Politecnico di Torino
Master's Degree in Aerospace Engineering

Master's Degree Thesis

A *Micro Glider* for stratospheric flight: design, manufacturing and testing

Thales Alenia Space Tutors
Ing. Alberto Congedi
Ing. Luca Simonini

Supervisors
Prof. Angelo Lerro
Dr. Luca De Pasquale

Candidate
Francesco Ghinamo

Academic Year 2024/2025

Abstract

The thesis project presented hereby aims at the development and testing of a scaled gliding vehicle capable of soaring from the upper layers of the atmosphere down to ground. This work finds its origins within a Thales Alenia Space internal venture, called *SpArks*, accelerated by the Space Business Catalyst (SBC), the industrial accelerator launched by the company's Innovation Cluster. Its goal is to create a totally new way of getting broad audience to know science, technology and expertise coming from the Space industry: a digital edutainment platform profiting from real Space assets with dedicated instrumentation, giving birth to the Playable Space Asset (PSAs) concept [10]. After this venture's first activities using stratospheric balloons as flying platforms, the next area of research concentrates on involving a more advanced flying machine: a remote-controlled glider, which will take the name of *Space Dart*. The objectives of this project are mainly focused on creating a ground-controlled aircraft capable of following a desired flight path and returning to the ground while streaming telemetry data and video live feed.
In order to pursue the aforementioned objectives, a full design process took place. In the first place, the main requirements for this product have been analyzed resulting in a detailed list of aerodynamic, structural and controllability performances as well as in an evaluation of the on-board systems structure. This lead to a first phase of avionics design carried out relying on off-the-shelf components. After this, the core study of this work is concentrated on aerodynamics and flight dynamics: to this end, an iterative procedure has been implemented to obtain the geometric details of the glider. Fluid dynamics evaluation software as OpenVSP and Xfoil have been used in this phase. Once in possession of these characteristics, a detailed 3D modeling of the aircraft followed. SolidWorks has been the main tool used for this purpose and to run CFD and structural FEM analysis as well. Once obtained a final design and after having sorted out the best manufacturing technique, the model has been 3D printed and eventually integrated with the electronics mentioned before.
The main outcome of this project is a fully-operative prototype of the *Space Dart* the venture is interested in. In addition, validation and testing of the platform have been conducted, proving the success and evaluating the accuracy of the before mentioned activities. Follow-ups to this work include, but are not limited to, outdoor flight testing in a real life operating scenario and further optimization of the vehicle itself regarding its aerodynamic properties, structural materials and on-board devices.

Contents

List of Figures

List of Tables

Chapter 1

Introduction

1.1 The SpArks project

SpArks is an internal open innovation venture developed within the framework of the industrial accelerator *Space Business Catalyst* of Thales Alenia Space; the SBC is an initiative led by company's Innovation Cluster to support the emergence of new markets and players in the space sector. This industry accelerator aims to shape and develop the space ecosystem of the future in collaboration with the best startups. *SpArks* aims to establish a platform that disseminates knowledge, technology, and expertise derived from space industry to a broader audience, and to make Space accessible to everyone. To this end, *SpArks* is designed to develop scientific and techno-digital products inspired by the domains of digital entertainment, casual education, and Web3 technologies, integrating them with dedicated instrumentation embedded on Space platforms and payloads: here it is where the concept of Playable Space Asset (PSA)[10] was born. The first targeted platform is a stratospheric balloon but, in the future, the goal is to deploy "actual" Space assets, thereby enabling ground-based users to interact with out-of-this-world flying objects. As a next step towards this goal, the development of a remote controllable flying machine comes into place. This solution aims to create a first dedicated platform to demonstrate how the aforementioned interaction can be implemented through the use of an object capable of flying through the upper layers of the atmosphere considered representative of a Space-like environment.

1.2 Objectives

The main goal carried out through this thesis project is the development of glider designed to be launched from a stratospheric balloon. The so called *Space Dart* gives the possibility to have a remote controlled lander capable of casting an augmented reality live feed of the flight to the ground while interacting with a gaming platform. This activity involves the development of a Minimum Viable Product (MVP). An MVP is a prototype of a certain device that includes functional versions of key elements that are planned for inclusion in the final one, and that is shared with a small audience whose feedback is used to inform and direct further product development [16]. For this purpose, the design activity has been focused on defining aerodynamics and flying qualities suitable for stratospheric flight. However, materials, manufacturing techniques and on-board devices didn't have to satisfy the final product requirements since the operating scenario of this MVP is limited to showcasing the project to which it belongs. For this reason, the material employed has been carbon fiber reinforced PLA (PLA-CF) and the prototype has been built using 3D printing. Regarding the on-board devices, model aircraft components have been used. Within this framework, a first analysis of the required on-board equipment has been carried out: in the first place regarding the venture's needs as a whole and then specializing it for the purpose of the MVP development. After this stage, the core activity of this research took place: a first-attempt aerodynamic shape have been conceived and linear aerodynamics analysis have been run to evaluate its aeromechanical properties. This lead to the implementation of an iterative procedure whose purpose has been the optimization of the aerodynamic surfaces and mass distribution in order to obtain the desired flying and handling qualities. Downstream of this process, a phase of detailed design and 3D modeling followed in order to enable the manufacturing stage through 3D printing. The final step of this work regarded the integration and testing of the developed platform: a crucial milestone to verify the success and attainability

of the whole project.
The aerodynamic study of the aircraft and the static and dynamic properties of its flight mechanics. This leads to the evaluation of loads and stresses on the structure and so to the sizing of the main structural components. Another important area of interest is the study and implementation of the onboard avionic system making it possible for the glider to be controlled and interact with the ground personnel. After this design phase, the natural follow up of the project is its manufacturing using 3D print and system integration. The final step is aimed to verify and test the model performance.

Chapter 2

Requirements analysis

2.1 Regulatory requirements

After having defined the framework in which this thesis work takes place, it is now time to focus on the details regarding the requirements imposed. To start with, an analysis of the constraints imposed by the current regulation of the European Commission is presented. The reference piece of law considered is the *REGULATION (EC) No 216/2008 OF THE EUROPEAN PARLIAMENT AND OF THE COUNCIL* regarding the operations with balloons. This is of interest to define the regulatory scenario this project is subjected to, since the *Space Dart* is meant to be launched from such balloons. In this context it results interesting to be aware of this definitions:

> (1) 'balloon' means a manned lighter-than-air aircraft which is not power-driven and sustains flight through the use of either a lighter-than-air gas or an airborne heater, including gas balloons, hot-air balloons, mixed balloons and, although power-driven, hot-air airships;
> (8) 'competition flight' means any air operation with a balloon performed for the purposes of participating in air races or contests, including practising for such an operation and flying to and from air races or contests;
> (9) 'flying display' means any air operation with a balloon performed for the purposes of providing an exhibition or entertainment at an advertised event open to the public, including practising for such an operation and flying to and from the advertised event [29];

As evidenced from *Article 3* of the aforementioned regulation, to undertake such *competition flights* or *flying display*, operators engaged in commercial operations shall demonstrate their capability and means of discharging the responsibilities associated with their privileges. These capabilities and means shall be recognized through the issuance of a certificate. The privileges granted to the operator and the scope of the operations shall be specified in the certificate [33]. In this regard, *Annex IV* of *Regulation (EC) No 216/2008* states that:

> An aircraft must be operated in accordance with its airworthiness documentation and all related operating procedures and limitations as expressed in its approved flight manual or equivalent documentation, as the case may be. The flight manual or equivalent documentation must be available to the crew and kept up to date for each aircraft [30].

From an operational standpoint, the same documents states that:

> A flight must not be commenced or continued unless the aircraft's scheduled performance, considering all factors which significantly affect its performance level, allows all phases of flight to be executed within the applicable distances/areas and obstacle clearances at the planned operating mass [31].

To satisfy these high level requirements on the operation of balloons the *Regulation (EC) No 216/2008* specifies that:

> An aircraft must be equipped with all navigation, communication and other equipment necessary for the intended flight, taking account of air traffic regulations and rules of the air applicable during any phase of the flight [32].

Coming to more concrete aspects, let's now consider the actual balloon intended as a carrier for this glider. The considered vehicle model is *Weather Balloon 3000* by *Stratoflights GmbH & Co. KG*, represented in Figure 2.1.

Figure 2.1: Weather Balloon 3000

This device is a stratospheric lighter-than-air aircraft designed to carry up to the higher layers of the atmosphere an instrumented payload aimed at gathering meteorological data. In this project's matter, this balloon will be considered as the selected vector for the *Space Dart* and technical requirements will arise from this. Its main features are summarized in Table 2.1 [25].

Model	Weather Balloon 3000
Weight	3000 g
Max. Payload	3000 g
Average burst altitude	40000 m
Ascent rate	4 - 5 m/s

Table 2.1: Carrier balloon features

Considering now the specific case study of this project, from the above mentioned statement it is possible to define a first list of technical requirements:

- the glider must be equipped with a GNSS receiver in order to establish its geographical position during each moment of its flight;
- when flying in controlled airspaces a transponder may be required for identification;
- the ground radio remote control must be capable of ensuring proper communication with the aircraft with acceptable latencies and no interruptions;
- it is advisable for the on-board control system to be equipped with a fail-safe feature meant to take control of the aircraft and land it safely in the case of ground remote control failure.

In addition to these qualitative specifications, it is possible to define also some geometry and mass constraints. They are shown in Table 2.2.

Max wingspan	0.80 m
Max weight	1 kg

Table 2.2: Regulatory requirements

The maximum wingspan requirement is set to ensure ease of handling while preparing the system for its launch; the weight limitation, instead, has been chosen to a third of the maximum payload capacity in order to leave room for balloon devices (i.e. its own on-board avionics, communication system and parachute) and a safety margin.
This eventually defines the properties this prototype must satisfy in order to be compliant with the current regulation.

2.2 Environmental requirements

In order to pursue the goal of designing such an aircraft, it is of fundamental relevance having a clear understanding of the natural environment in which it will operate. The following section explores the most relevant details of the atmospheric layers interested by this glider's flight: stratosphere and troposphere. Prior to deepen the technical details that interest the actual development of the aircraft, a brief description of the atmosphere structure is presented.
The atmosphere is comprised of layers based on temperature. These layers are the troposphere, stratosphere, mesosphere and thermosphere. A further region at about 500 km above the Earth's surface is called the exosphere [11]. The picture in Figure 2.2 [17] shows the air temperature profile with respect to the altitude, identifying the corresponding layers.

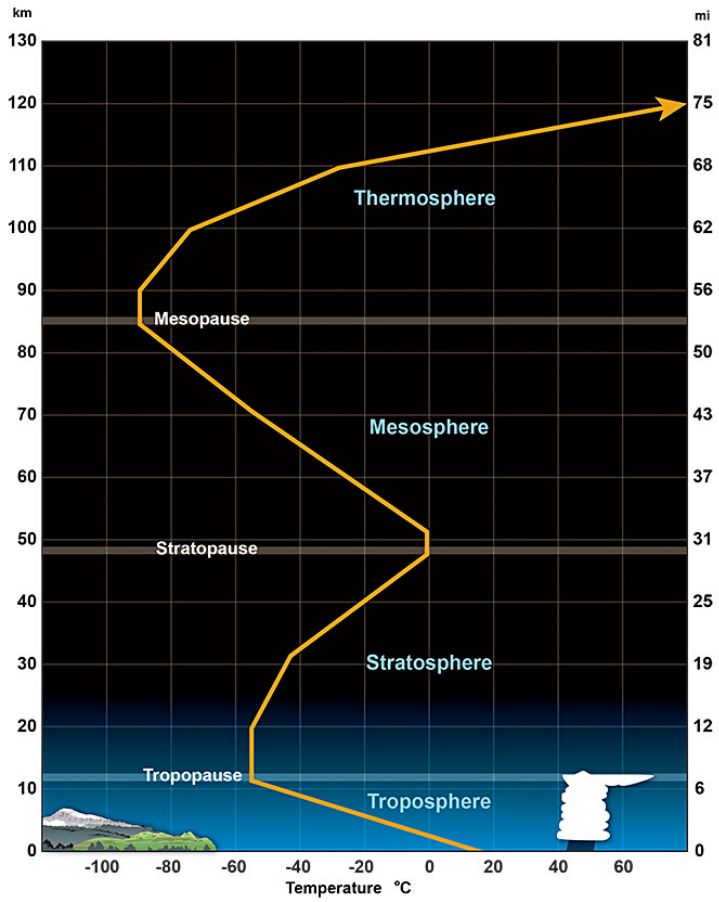

Figure 2.2: Artistic representation of atmosphere layers and temperature profile

Concentrating now on the two areas interested by this research, a brief insight is presented hereafter.

The troposphere This is the lowest part of the atmosphere - the part we live in. It contains most of our weather - clouds, rain, snow. In this part of the atmosphere the temperature gets colder as the distance above the earth increases, by about 6.5°C per kilometer. The actual change of temperature with height varies from day to day, depending on the weather.
The troposphere contains about 75% of all of the air in the atmosphere, and almost all of the water vapor (which forms clouds and rain). The decrease in temperature with height is a result of the decreasing pressure. If a parcel of air moves upwards it expands (because of the lower pressure). When air expands it cools. So air higher up is cooler than air lower down.
The lowest part of the troposphere is called the boundary layer. This is where the air motion is determined by the properties of the Earth's surface. Turbulence is generated as the wind blows over the Earth's surface, and by thermals rising from the land as it is heated by the sun. This turbulence redistributes heat and moisture within the boundary layer, as well as pollutants and other constituents of the atmosphere.
The top of the troposphere is called the tropopause. This is lowest at the poles, where it is about 7 - 10 km above the Earth's surface. It is highest (about 17 - 18 km) near the equator [13].

The stratosphere The stratosphere extends from 6-20 km above the Earth's surface to around 50 km. This layer holds 19 percent of the atmosphere's gases but very little water vapor. In this region, the temperature increases with height. Heat is produced in the process of the formation of ozone, and this heat is responsible for temperature increases, from an average -51°C at tropopause to a maximum of about -15°C at the top of the stratosphere. This increase in temperature with height means warmer air is located above cooler air. This prevents convection as there is no upward vertical movement of the gases. As such, the location of the bottom of this layer is readily seen by the anvil-shaped tops of cumulonimbus clouds [12].
The transition layer at the top of the stratosphere is called the stratopause.

2.2.1 The International Standard Atmosphere model

After this qualitative overview on the atmospheric environment, it is now possible to dive into more technical detail of the aspects that will eventually influence the glider design. In this regard it results handy to introduce the International Standard Atmosphere (ISA) model. This analytic representation of atmosphere physical properties has been introduced at the Paris Convention held in 1919. It's main goal is to define standard quantitative physical properties values relevant to the study of the implications they have on engineering applications. In particular, to the end of this work, this model will be useful to evaluate aircraft performance with respect to the altitude, represented with the symbol z, and to take into account its effects during the design phase. To begin with, let's define what is actually considered "air" in this regard: air is a mixture of different gases with the molecular weights and mass ratios presented in Table 2.3. Combining these properties it is possible to obtain air molecular weight M, considered as a whole.

Constituent	Molecular weight [kg/mol]	Mass ratio [%]
N_2	28.019	75.5
O_2	32.000	23.1
Ar	39.944	1.28
Air	**29.05**	**100**

Table 2.3: ISA chemical air composition

In addition to this, within this framework, air is considered as a perfect gas, thus the ideal gas law holds:

$$\frac{p}{\rho} = \frac{R}{M}T \tag{2.1}$$

where[1]:

- T: temperature;
- p: pressure;

[1] unless otherwise specified, all quantities in this document are expressed according to the International System (IS)

- ρ: density;
- R: universal gas constant, equal to 847.8 $\frac{kg\ m}{K\ mol}$.

Once these aspects have been established, detailed features of atmospheric layers can be presented.

Troposphere

The main outcome of this model is a law of variation of a certain state variable (e.g. p, pressure) with respect to the altitude z. Let's begin considering the troposphere: the lower layer that spans from sea level up to an altitude of 11000 m. To this end, the following aspects are considered:

- Stevino law holds: $dp = -\rho g dz$;
- ideal gas, equation 2.1 holds;
- constant temperature gradient: $\frac{dT}{dz} = -h = 0.0065\ \frac{K}{m}$;
- sea level ($z = 0\ m$) state defined as: $p_0 = 101325\ Pa$, $T_0 = 288\ K$, $\rho^* = 1.225\ \frac{kg}{m^3}$.

As an immediate outcome of these statements, the temperature law can be obtained:

$$T = T_0 + hz \tag{2.2}$$

Integrating the Stevino law considering the dependency with altitude of the temperature (Equation 2.2) of the above defined ideal gas (Equation 2.1), it is possible to demonstrate the following relation between pressure p and altitude z:

$$\left(\frac{p}{p_0}\right)^{\frac{1}{m}} = 1 - \frac{hz}{T_0} \tag{2.3}$$

where m is defined as $m = \frac{M}{h\ R} = 5.2561$.
Combining equation 2.3 with 2.1 it is of immediate deduction the following expression, which relates density ρ and altitude z:

$$\left(\frac{\rho}{\rho_0}\right) = \left(\frac{T_0 - hz}{T_0}\right)^{m-1} \tag{2.4}$$

Stratosphere

Similarly to what has been done to study the troposphere, the same aspects are analyzed regarding the stratosphere. To this purpose, every quantity referred to the base of this layer - the tropopause - is referred to with an asterisk $(\cdot)^*$. The following features are taken into account:

- tropopause altitude is $z = 11000\ m$
- Stevino law holds;
- ideal gas;
- temperature is constant throughout this layer, this Boyle-Mariotte law holds: $\frac{p}{\rho} = \frac{p^*}{\rho^*}$;
- tropopause ($z = 11000\ m$) state defined as: $p^* = 22632\ Pa$, $T^* = 216.5\ K$, $\rho^* = 0.3637\ \frac{kg}{m^3}$.

Combining these relations, it is possible to obtain the following equations describing the variation of pressure p and of density ρ with respect to the altitude z:

$$\frac{\rho}{\rho^*} = \frac{p}{p^*} = e^{\frac{z-z^*}{\frac{R}{M}T^*}} \tag{2.5}$$

Downstream of these considerations, it is possible to plot the characteristics of the above mentioned quantities with respect to the altitude. Pictures 2.3, 2.4 and 2.5 are referred respectively to temperature, pressure and density.

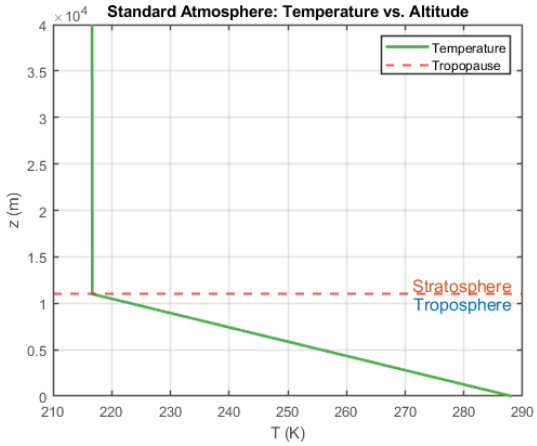

Figure 2.3: Temperature vs. Altitude (ISA)

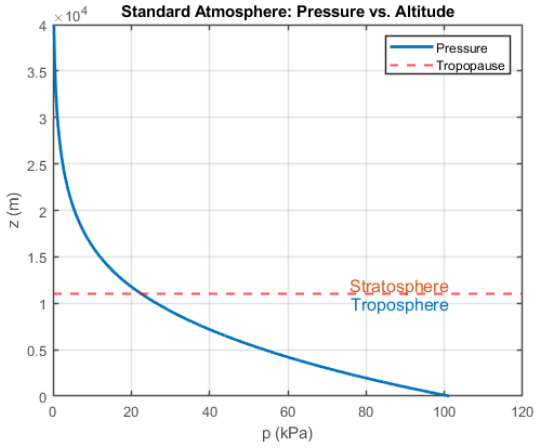

Figure 2.4: Pressure vs. Altitude (ISA)

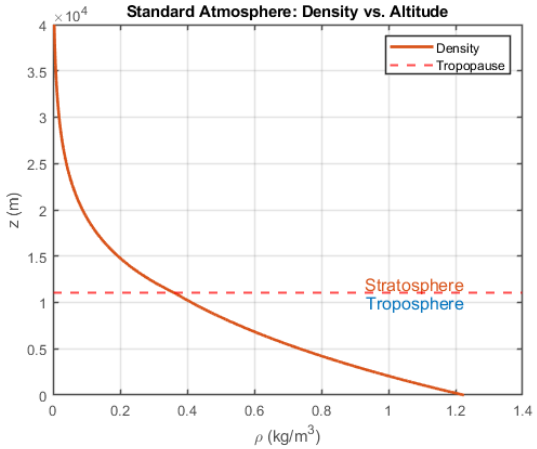

Figure 2.5: Density vs. Altitude (ISA)

As it is possible to notice, each of the three quantities decreases with increasing altitude. This leads to the following implications:

- temperature drops linearly in troposphere, reaching the minimum value of 216.5 K at tropopause and maintaining it through the stratosphere. Hence, this is the most critical value for this quantity

to be considered. This is useful to select structural materials and on-board electronics able to withstand these environmental conditions;

- pressure decreases almost to a 20% of its value at sea level while crossing tropopause: this has to be taken into account if employing operating fluids (such as those used for hydraulic actuation) and to provide a sufficient out-gassing flow of the internal bays of the glider to avoid explosion during ascent;
- the density drop has direct consequences on the dynamic pressure can be generated at a given speed. This is of interest because every aerodynamic action (force or torque) is directly proportional to this quantity. A lower dynamic pressure means lower lift and lower authority over the control of the aircraft: in order to recover suitable performance in low-density conditions, airspeed has to be increased. This aspect requires further analysis regarding the the effect of air compressibility, whose occurrence can be stated considering Mach number. This topic will be discussed in the following subsection.

2.2.2 Compressibility effects and Mach number

As aforementioned, the need for flight controllability has to be study taking into account its implications regarding flight speed and, in particular, its ratio with the speed of sound: the Mach number. The Mach number is hence defined as in Equation 2.6:

$$M = \frac{v}{a} \tag{2.6}$$

where:

- v: is the flow speed;
- a: is the speed of sound.

As shown in Equation 2.7, a is a state variable and depends on the state of the fluid it is referred to.

$$a = \sqrt{\gamma \frac{R}{M} T} = \sqrt{\gamma \frac{p}{\rho}} \tag{2.7}$$

From these simple equations it is possible to deduce that speed of sound decreases with increasing altitude. This aspect is clearly shown in Figure 2.6.

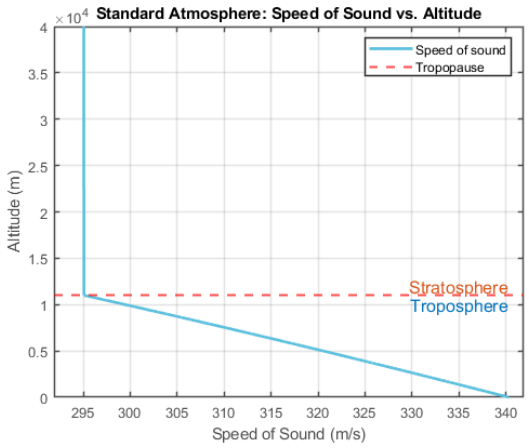

Figure 2.6: Speed of sound vs. Altitude (ISA)

When coming to consider velocities that can be compared to that of sound, a physical effect comes into place: compressibility, and Mach number can be interpreted as a descriptor of the magnitude of this phenomenon. For general applications, it is generally considered a threshold of M < 0.3 for incompressible flow. In presence of higher Mach numbers, flow compressibility must be taken into account. The velocity range of interest for this project corresponds to that of the lower-subsonic, incompressible speed regime,

characterized by M < 0.3. This constraint implies that air density can be considered as a constant fixed by the environmental conditions (i.e. the altitude). This hypothesis of low Mach number flow, and thus incompressible regime, allows to exclude any phenomena related to compressibility - such as shock waves or expansion fans - and is consistent with the application of potential flow-based aerodynamic simulations. More about the application of such methods will be explained in the following chapters. Downstream of these considerations, it is now possible to evaluate at each altitude the maximum flight speed threshold in order not to overcome the M < 0.3 constraint. This is shown in Figure 2.7. Unless otherwise specified, every *speed* referred to Flight Speed is intended as True Air Speed (TAS).

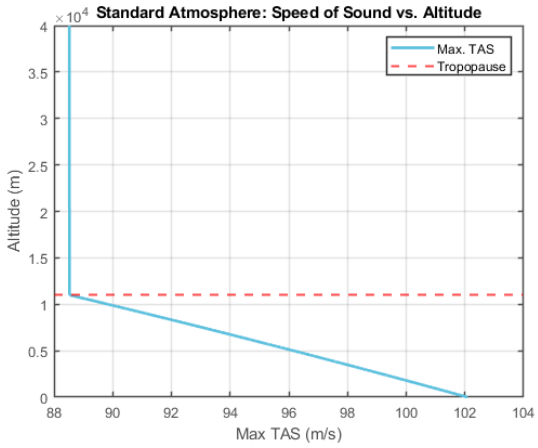

Figure 2.7: Max TAS vs. Altitude (ISA)

The latter considerations pose a constraint on the maximum allowed airspeed to maintain suitable performance with decreasing air density while remaining in compressible regime.
The requirements coming from considerations on flight environment are summarized in Table 2.4.

Min temperature	216.5 K
Max. Mach number	0.3

Table 2.4: Environmental requirements

2.3 Mission requirements

Coming to consider more detailed aspects of this project, a detailed analysis of the characteristics imposed by the use case of this glider is carried out. In this context, a specific analysis of the relationship between the *Space Dart* and the *SpArks* initiative edutainment contents is explored.
In the first place, the main objective of this product is that of providing a live feed of the flight to the ground personnel (i.e. the player). To this end, an on-board camera has to be present. This device must be capable of generating an high quality video stream suitable to be used in an augmented reality environment. This imposes the requirement for a high resolution-wide angle camera. In addition to this, in order to ensure a fluid video experience, a sufficiently high frame rate is also recommended.
Secondly, in order to implement remote control functionalities, radio link between the ground and flight segments has to be established. This communication channel must be characterized by long range coverage, high reliability, high packet rate and low latency. All of the latter are necessary to implement a successful pilot-in-the-loop control philosophy. Control commands, in fact, have to take effect instantaneously once applied by the pilot, and they have to be accurate and reliable even when flying at a great distance from the ground (e.g. stratospheric launch conditions). In addition to this, telemetry data has to be transmitted within this channel. This adds the requirement for a sufficiently precise synchronization among aircraft state, control commands upstream and telemetry downstream.
As a direct consequence of the previous aspects, an intermediate layer to interface the gaming platform with the flight segment has to present. This element is crucial to make the glider suitable product to play with. The task of flying such an aircraft in a controlled descent across the aforementioned atmosphere

layers cannot constitute a gaming activity by itself: required skills would mismatch from the goal of the *SpArks* initiative. For this reason, the duties of this logical element are those of allowing flight control throughout traditional gaming devices, user-friendly representation of aircraft state during flight and flight envelope protection. To pursue these objectives, this interface layers must implement user commands acquisition and flight control logic, while being able to establish an effective communication between them.
Another mission requirement is relative to the use effectiveness of this product: in order for it to be compliant with its employment within the edutainment environment, the glider must be able to ensure a sufficient long flight time. This constraint comes from directly from the features of the gaming environment and mostly depends on the initial launch altitude. To the end of this preliminary design, it has been set to 20000 m.
Another on-board equipment requirement comes from the strategy that will be adopted for flight termination. Since the implementation of a landing procedure on proper landing gears would require a sophisticated control law - and this would be beyond the scope of this project, a parachute is seen as the most viable solution. This device, in fact, allows to perform a safe and controlled descent without the necessity of a control system. The parachute is meant to be deployed when crossing a certain altitude threshold, slowing down the aircraft and changing from the phase of gliding flight to that of controlled fall. To this end, it necessary to specify that this device must me capable of ensuring a sufficiently low terminal velocity not to compromise structural integrity upon ground impact. At the same time, despite not being equipped with an active trajectory control, the parachute has to ensure the most regular fall trajectory so that the landing location can be easily predicted.
Finally, in order to determine the aircraft location with a sufficient level of precision, a GNSS equipment is needed. This device is useful both during the gliding phase of flight - to know instantaneously flight path and ground speed - and after landing - in order to know the exact location of the vehicle and make retrieval operations easier. Ultimately, this subsystem is fundamental for the integration with the gaming platform, allowing the glider to be properly used as the object of the gaming scene.

2.4 Required on-board devices

At this stage, an analysis of the required materials is carried out, considering as a reference the aforementioned list of requirements.
In the following paragraphs, a list of the required devices is presented. Along with it, a brief description of each element functionality and relevance is reported.

Flight Control Computer This represents the actual core of the on-board system and implements all control functionalities and resource management. It takes care of implementing the flight control logic and manages the radio communications used to interact with pilot's commands. In addition, this unit is responsible for handling the on-board camera and transmitting the real-time video signal to the ground. Each of every other on-board device is connected to this central unit. As it will be discussed later, this device can either be considered as a single physical unit in which all the aforementioned functionalities are concentrated, or as a logical entity with its assigned tasks distributed across multiple dedicated devices. This component will be referred to as the *FCC*.

Flight Control Firmware Along with the hardware equipment mentioned above, the actual control logic has to be considered as a crucial element by itself. This piece of software implements the control law aimed to fly the aircraft in a smooth and controlled way, following pilot's commands, integrating signals from the installed sensors, producing outputs for the actuators and managing radio communication. If necessary, this firmware has to provide Stability Augmentation System (SAS) features and may include autopilot functionalities to take control of the glider in case of ground communication loss. As already mentioned, the latter acts as a fail-safe mechanism to implement Return To Home (RTH) capability to land the vehicle autonomously and safely in a predetermined spot. This feature my be triggered automatically upon pilot's control failure - this eventuality could occur if the aircraft exceeds the maximum radio range.

ExpressLRS Module The use of this component is motivated by the need to establish a remote link between the ground control station and the aircraft. The *ExpressLRS* consists of an open-source communication system useful to implement remote controlled systems. To this end, ground and on-board transceivers modules are employed. It is characterized by the maximum achievable range at a given

frequency with the lowest possible latency. These features are crucial to ensure a suitable communication channel for flight control. This element, referred to as the *ExpressLRS transceiver*. Telemetry data transmission relies on this element.

Radio Communication Module In order to implement long-range radio communication, this module is required. This element is meant be employed to transmit auxiliary flight data, such as real-time video streaming with telemetry overlay: *OSD (On Screen Display)*. This component is referred to as the *Analog video transmitter*.

GNSS Module This device is meant to identify at the geographical location of the vehicle, allowing the aircraft's position and speed to be determined in real time. This device will simply be referred to as *GNSS*.

Transponder This device is required in order to enable aircraft identification when flying within controlled airspaces. The presence of a *Transponder* is mandated by regulatory requirements.

Inertial Platform This set of sensors is required to determine the aircraft attitude and angular velocities. This unit, globally referred to as the *IMU (Inertial Measurement Unit)*, is composed of a linear accelerometer (*Acc*) and a gyroscope (*Gyro*).

Air Data System The need for this module comes from the necessities of a complete determination of the aircraft's flight dynamics, such as altitude and airspeed. Consequently, this unit consists of a barometer (*Baro*) - for altitude measurement - and a Pitot tube (*Airspeed*) for airspeed determination.

Servo Actuators These devices are mainly required to actuate the primary flight controls (*Flight controls*), but also to perform various other mechanical operations that may be necessary. They are referred to as *Servos*.

Camera To the end of providing a video feedback of the flight activity, an on-board camera connected to an acquisition system is needed. After the scene has been captured by the camera, the *FCC* takes care of video compression and transmission, relying on the *Analog video transmitter*. This component is referred to as the *Camera*.

Parachute The conclusion of each flight is meant to be performed through the use of a parachute, ensuring a non-gliding controlled descent. This device must be completely housed within the structure so that it can be deployed upon a specific command. This element is referred to as *Parachute deployment*.

Batteries This component takes care of the power required by the entire system. In order to choose a suitable power supply system, a proper balance between maximum available capacity and weight is requiresd. The power system will be referred to as the *Battery*.

Ground Equipment The final logical element completing the general framework of required materials is the ground equipment. This refers to the devices necessary for aircraft flight control, monitoring, and video reception. For flight control, a radio controller (*Radio controller*) and an *ExpressLRS transceiver* module are required to communicate with the on-board counterpart. For video signal reception, a radio receiver (*Video receiver*) and a monitor (*Video output display*) are necessary.

2.5 Trade-off Analysis

In light of the previous analyses, a study is conducted to determine the optimal configuration that achieves the best compromise among the stated requirements, including environmental constraints, providing supporting reasoning. As will be discussed below, the system architecture can be implemented in multiple ways, each with its strengths and limitations. Two main configurations are analyzed: the first concentrates all functions within a single physical unit, while the second divides the flight control and video acquisition/transmission features between two separate devices.

2.5.1 Centralized functionality solution

The centralized architecture employs a single central unit to manage both flight control and video acquisition/transmission. Figure 2.8 shows this solution.

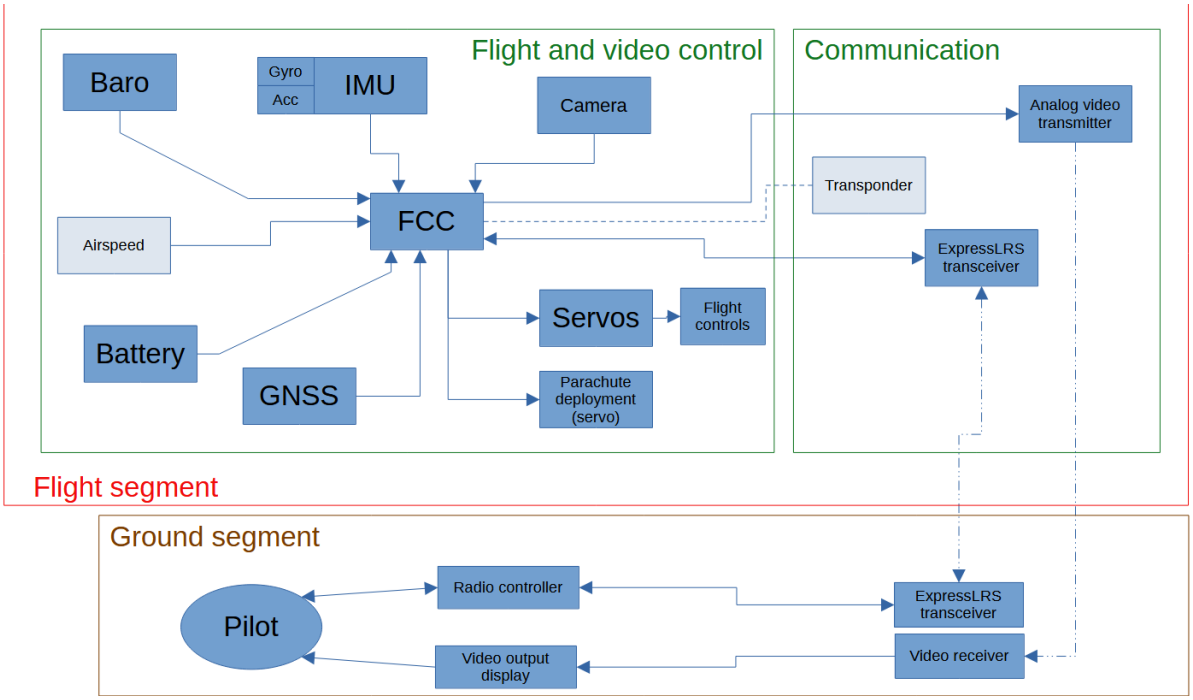

Figure 2.8: Centralized functionality architecture

As observed, this architecture involves a single on-board computer to which all signals and information converge. It integrates this data and generates commands for the servo actuators, while also managing telemetry and video signals. This scheme requires a control board capable of interfacing with all devices and, consequently, suitable firmware to perform these tasks. The control device thus has to deal with both flight control information and video data. Given the differences between control and video signals, as well as the bi-directionality of the former versus the downstream-only nature of the latter, the presence of two separate antennas is still necessary. Despite these challenges, this architecture shows its advantages in terms of weight: only one board is required and this minimizes the overall system weight and size. Additionally, telemetry and video can be managed in an integrated manner, enabling telemetry overlay on the video signal. The centralized nature also ensures that the video information is synchronized with the aircraft's real-time behavior, making an important feedback source for flight operation out of it.

2.5.2 Distributed functionality solution

The second type of solution analyzed distributes on-board functionalities between flight control management and video signal transmission. This architecture is shown in Figure 2.9.

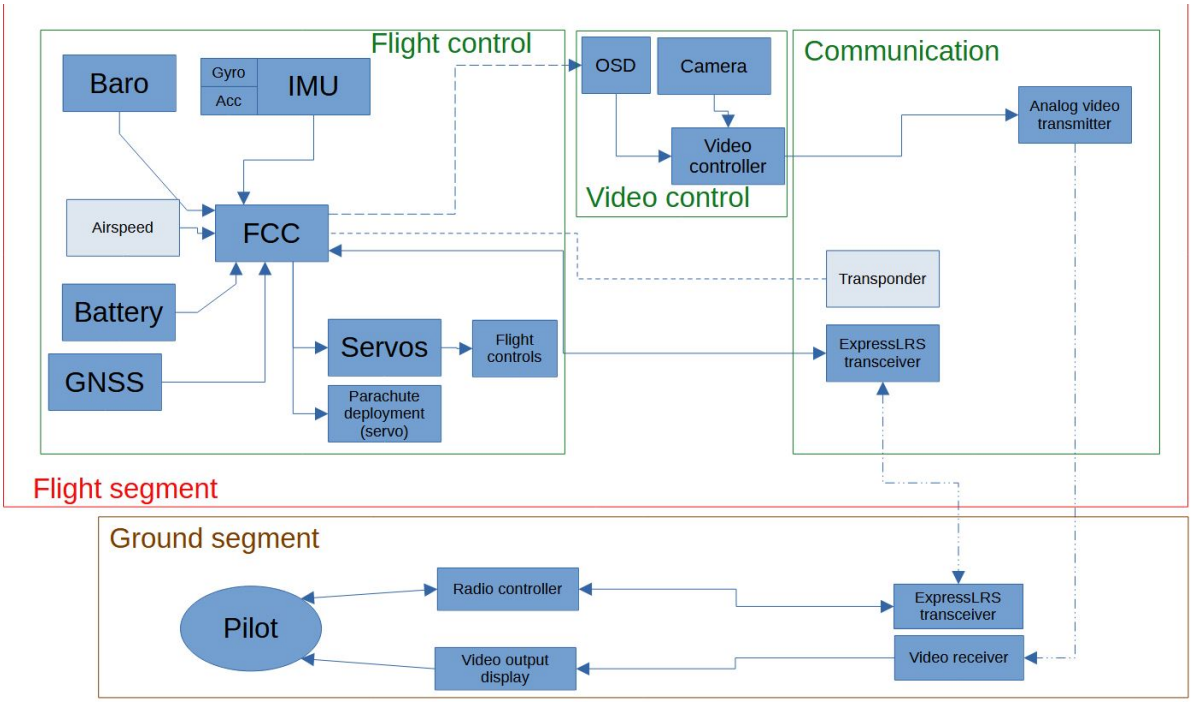

Figure 2.9: Distributed functionality architecture

Such a system simplifies implementation. As shown, it requires two control units: one dedicated to flight control and another for video management. This creates two independent systems, each assigned to a specific task. The first unit manages flight parameters, control, and telemetry, receiving only related radio signals. The second unit acquires the video signal from the camera and transmits it to the ground via its dedicated radio antenna. While this architecture may appear easier to implement, it has drawbacks. The use of two central units significantly increases the system's weight and size. Furthermore, segregating flight control and video information makes the use of video not a viable option as a piloting aid (due to potential asynchronous management of video streaming with respect to flight conditions) and complicates telemetry overlay.

2.5.3 Architecture selection

Based on the considerations presented, the chosen on-board configuration aims to minimize total weight and simplify the integration of functionalities. Therefore, the centralized solution was selected. As described above, this architecture employs a single central unit, this implies using a board that integrates many necessary elements (such as the inertial platform, OSD module, barometer, etc.), thereby reducing the total number of individual devices. Moreover, a centralized solution facilitates the management of on-board power: the battery interfaces with the single control board, which regulates and distributes energy to all installed elements. Another significant advantage is the synchronization of functionalities. By concentrating all tasks within a single unit, both radio communications (for flight control and video transmission) can be managed so that the video information is consistent with flight control data, minimizing latency. Finally, having both types of information within the same device simplifies the transmission of telemetry overlaid on video.

2.5.4 Materials required for the demonstrator

As an outcome of the previous considerations, it is eventually possible to define a complete list of the needed on-board equipment. From this point on, the listed materials and features are specific for the creation of the aforementioned MVP. As such, these devices have been chosen in order to meet the operational requirements essential to effectively represent the glider role within the venture's project. In this matter, the following constraints have been discarded:

- low temperature compatibility: the MVP is meant to be launched in a lower-troposphere environment:

this implies that temperatures are significantly higher than those in stratosphere. As a consequence of that, on-board devices - especially electronics - is not required to be certified for extreme operating conditions. In addition, this enables 3D printing to be adopted as manufacturing technique and material such as PLA to be used;

- high Mach number flight regime: another implication of flying in a high air density environment is that of lower airspeed necessary to obtain suitable aerodynamical loads. In addition to this - and as a consequence of higher air temperature in troposphere than in stratosphere - speed of sound is expected to be high enough to maintain significantly low Mach numbers. The direct consequence of this is that of allowing aerodynamical study within the incompressible regime. Nevertheless, the aerodynamical study has been conducted for stratosphere flight conditions;
- Long-range radio link: low altitude flight allows the requirement for long-range radio link to lapse. This is because the MVP, as it is conceived, would never fly in sufficiently high altitude necessary to cover enough distance to require specific long-range radio link capabilities. Although the employed technologies, such as ExpressLRS, may still satisfy long-range requirements, signal power can be reduced: this makes the use of smaller power supply devices (i.e. batteries) possible, hence making the prototype lighter;
- mission duration: acting as a demonstrator for the final product, the MVP doesn't have to satisfy strict flight time constraints. Once again, this allows smaller batteries to be employed.

Downstream of the above mentioned aspects, a detailed study and selection of the on-board needed materials has been conducted. In this matter, company's suppliers catalogs have been consulted and, after evaluating the mutual compatibility of the devices found, a definitive list has been defined. Hereafter, a brief paragraph reports the most relevant features for each element.

Flight Control Computer *Matek F411 WTE*: this is the selected board that will be used as the core of the avionics system. This device is mainly intended for model aircraft applications and comes with a tailored flight control firmware (more about this in the following paragraph). The board is lightweight and compact - fundamental features for airborne use - and is equipped with several interfaces to which is possible to connect peripherals such as sensors, actuators and transceiver devices. In addition, it also features built-in IMU, barometer, analog video capturing, On Screen Display (OSD) functionalities and power management capabilities. Technical specifications are highlighted in Table 2.5 [8].

FCC Specifications	
IMU	ICM42688P (built-in)
Barometer	SPL06-001 (built-in)
OSD	AT7456E (built-in)
UART interfaces	2
Full softserial interfaces	2
PWM outputs	6
ADC interfaces	4
Power	
Rating	6-30V DC
Required battery	2-6S LiPo
FCC Firmware	
Software	INAV 4.1 or newer (see next paragraph)
Physical	
Dimensions	31 x 26 x 16.5 mm
Wight	10 g

Table 2.5: FCC specifications

Picture in Figure 2.10 shows the above described board.

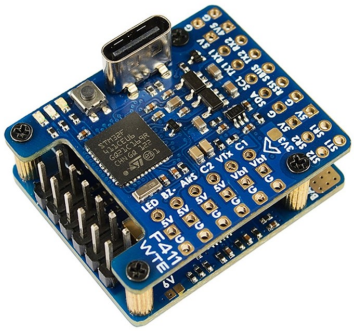

Figure 2.10: Matek F411 WTE

Flight Control Firmware *INAV 6.0.0*: this is the selected firmware employed for this project. INAV is an open-source project that provides a navigation-enable flight control firmware. This software can be configured to operate both with fixed-wing and moving-wing aircraft. Since operating in the former scenario, it is possible to set within this firmware configuration environment the type of vehicle, number and type of control surfaces, control law gains and a proper SAS system. In addition, it is capable of managing radio communication, telemetry and video acquisition and streaming. At last, the firmware can be configured to implement the fail-safe RTH logic. As it will be discussed afterwards, this version has been chosen as the last release compatible with the NMEA GNSS protocol: this strongly depends on the GNSS receiver and the latter is the only protocol supported by the chosen device.

ExpressLRS module *Matek ELRS-R24-D*: this is an ExpressLRS-compliant tranceiver device to be installed on-board of the aircraft. It is fully compatible with the FCC board and the installed firmware. It is composed of a main shield from which two antennas branch off. Connection with motherboard is ensured by the UART interface, and radio link relies on the Crossfire (CRSF) protocol. This device enables radio communication for remote control purposes and for telemetry transmission. Table 2.6 [15] highlights the most relevant technical features.

ExpressLRS Specifications	
Board interface	UART
Signal frequency	2,4 GHz (2400-2480 MHz)
Telemetry power	22,5dBm - 23dBm
RX Gain	12.5 dB
RF protocol	CRSF
Antenna	IPEX MHF 1
Power	
Operating voltage	4-9 V CC @ 5 V pad
Physical	
Dimensions	21 x 15 x 5 mm
Wight	3 g

Table 2.6: ExpressLRS specifications

Figure 2.11 represents as this device appears.

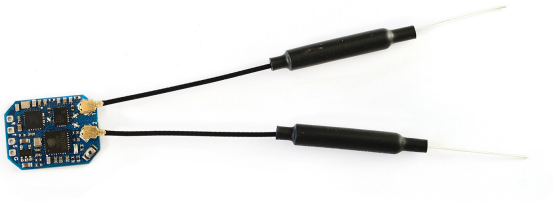

Figure 2.11: ExpressLRS transceiver

Radio communication module *TBS Unify Pro 5G8 V3*: this module is an analog video transmission (VTX) shield. It is capable of collecting a video digital signal, amplifying it relying on power supply, and casting a live stream via radio link. Air to ground connectivity is established thanks to a monopole HF omnidirectional antenna. This means that signal power is radiated in every space direction. In order to establish a sufficiently stable radio link, a more directional antenna has to be employed. Table 2.7 [28] reports technical details of this equipment.

VTX Specifications	
Board interface	Power supply & Video signal
Signal frequency	5.8 GHz
Signal power	up to 800 mW
Antenna connector	RP-SMA Female
Power	
Operating voltage	4.5-5.5 V CC @ 5 V pad
Physical	
Dimensions	21 x 15 x 5 mm
Wight	5 g

Table 2.7: VTX specifications

Figure 2.12 is a visual representation of this object.

Figure 2.12: VTX module

GNSS module *Seeed Studio 113020003*: this device provides GNSS satellite communication. It is composed of a circuit board on which signal receivers are installed and of an antenna connected to it.

This module complies with the NMEA standard and can be directly connected to the main board via UART interface. Features are shown in Table 2.9 [23].

GNSS Specifications	
Board interface	UART
Sensitivity	up to -160 dBm
Compatible constellations	GPS, Galileo, Glonass
Supported protocols	NMEA, U-BLOX
Power	
Operating voltage	2.75-3.6 V CC @ 5 V pad
Physical	
Dimensions	13 x 20 x 40 mm
Wight	10 g

Table 2.8: GNSS specifications

Image in Figure 2.14 is representative of this device.

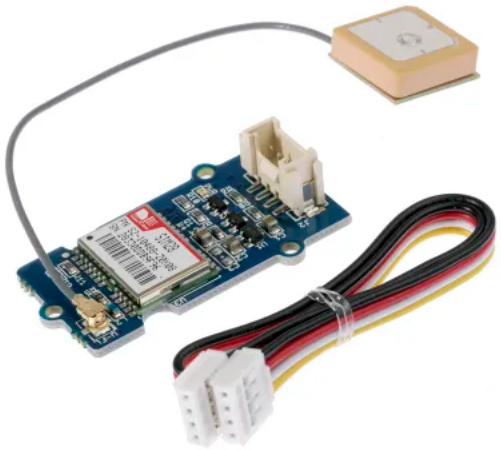

Figure 2.13: GNSS module

Inertial platform *FCC built-in*: as mentioned in the FCC paragraph, the inertial platform (also called IMU), in is included in the FCC board. This device features a six axis sensor, capable of measuring linear and angular accelerations along three independent space axis.

Air Data System *Matek ASPD-4525*: this device is a sensor capable of measuring airspeed relying on a Pitot tube probe. To this end, the sensor is equipped with two inlets to which total pressure and static pressure tubes are connected. This sensor embeds an ADC converter to translate the pressure differential analog one to a digital one. For this reason, this shield communicates with the board via the ADC interface. Table [14] lists technical details for this element.

Airspeed sensor Specifications	
Board interface	ADC
Sensitivity	up to -160 dBm
Compatible constellations	GPS, Galileo, Glonass
Supported protocols	NMEA, U-BLOX
Power	
Operating voltage	2.75-3.6 V CC @ 5 V pad
Physical	
Dimensions	13 x 20 x 40 mm
Wight	10 g

Table 2.9: Airspeed sensor specifications

Figure represents the described module.

Figure 2.14: Airspeed module

Regarding the barometer sensor, it results from the FCC specifications to be included in the board. For this reason no other specific sensor has been selected.

Servo actuators *Kitronik micro Servo*: this little device is a basic, low-power servo actuator with a maximum moving range of 180 degrees. Its external structure features screw holes useful to fix the actuator to the airframe. In addition, the moving shaft is fitted with a pinion: this will be used to ensure mechanical link between the servo and the actuated element. Table 2.10 [9] showcases this element most relevant features.

Servo actuators Specifications	
Board interface	Power & PWM signal
Max. range	180°
Max. torque	0.12 Nm
Power	
Operating voltage	5 V CC @ 5 V pad
Physical	
Dimensions	11.8 x 22.7 x 26.7 mm
Wight	10 g

Table 2.10: Servo actuators specifications

Picture in Figure 2.15 is a representation of this element.

Figure 2.15: Servo actuator

Camera *CADDX ANT - 1200TVL 16:9 FPV NANO Camera*: this device is fundamental to capture the scene the glider is flying through. Its lightweight and compact feature make it ideal to be employed for the designed goal. It is compliant with the NTSC and PAL video standards and its fairly high resolution and aspect ratio should be capable of giving a nice video experience. More technical aspects are reported in Table 2.11 [5].

Camera Specifications	
Board interface	Power & analog signal
Horizontal resolution	1200 TVL
Video standard	NTSC or PAL
Video aspect ratio	16:9 or 4:3
Sensor	1/3" CMOS
Focal length	1.8 mm
Power	
Operating voltage	3.7 - 18 V DC
Physical	
Dimensions	14 x 14 x 14 mm
Wight	2 g

Table 2.11: Camera specifications

In Figure 2.16 this element is showcased.

Figure 2.16: Camera

Parachute This element has been considered as object of design and as such, its development will be discussed in the following chapters.

Batteries *Tattu LiPo Battery*: in order to identify the most suitable power source for this application, two LiPo batteries have been selected: a 3 cells and a 4 cells ones. The former has been chosen for a matter of reducing total on-board weight, while the latter for the aim of granting a longer mission timespan. Table 2.12 [26] report the 3 cells battery main technical features, which is showed in Figure 2.17.

3 cells Battery Specifications	
Technology	LiPo
Number of cells	3
Output voltage	11.1 V
Capacity	750 mAh
Charging capacity	95 C
Connector	XT-30 female
Physical	
Dimensions	21 x 31 x 60 mm
Wight	62 g

Table 2.12: 3 cells Battery Specifications

Figure 2.17: 3 cells Battery

Likewise, Table 2.13 [27] and Figure 2.18 are relative to the 4 cells battery.

4 cells Battery Specifications	
Technology	LiPo
Number of cells	4
Output voltage	14.8 V
Capacity	1300 mAh
Charging capacity	130 C
Connector	XT-60 female
Physical	
Dimensions	25 x 76 x 38 mm
Wight	143 g

Table 2.13: 4 cells Battery Specifications

Figure 2.18: 4 cells Battery

2.5.5 Ground Equipment

After having completely defined the on-board required devices, a list of the equipment necessary to operate the aircraft from the ground is presented hereafter.

Radio Remote Control *RadioMaster Pocket*: this element is the radio transceiver meant to be hold in pilot's hands to control the glider and to receive real-time telemetry data. This remote control, in fact, is equipped with sticks and buttons that can be programmed to perform specific actions over the aircraft. In particular, sticks will be used for controlling mobile surfaces while buttons are ideal to trigger different flight modes or parachute deployment. This device come with a preinstalled EdgeTX firmware that enables ExpressLRS communication and is capable of running the so-called LUA script, required to handle and display telemetry data. This element also features a LCD display on which the latter can be showed. Table 2.14 [21] reports the main features of this element, which is showed in Figure 2.19.

RadioMaster Pocket Specifications	
Operating frequency	2.4 - 2.48 GHz
Operating system	EdgeTX
Display	128 x 64 Monochrome LCD
Supported protocols	ELRS & CC2500
Control channels	16
Power	
Batteries	2 x 18650 batteries
Physical	
Dimensions	156.6 x 73.1 x 154.8 mm
Wight	288 g

Table 2.14: RadioMaster Pocket Specifications

Figure 2.19: RadioMaster Pocket

Ground video antenna *YAGI OSCAR18*: this antenna has been chosen for its directional properties. As mentioned before, the on-board video antenna emits its signal with spherical symmetry, thus radiating power along every space direction. This means that only a small fraction of the total emitted signal is actually directed to the ground receiver. In order to establish a stable link, it is necessary to use a ground device with a sufficiently collimated radio beam and point it directly toward the emitting antenna: this allows to open a communication channel despite a low power signal. Table 2.15 [19] reports this device main features.

Yagi Antenna Specifications	
Spectrum coverage	400 - 6 GHz
Connector	N-TYPE Female
Antenna cable	RG58
Physical	
Dimensions	290 x 208 x 50 mm
Wight	0.9 kg

Table 2.15: Yagi Antenna Specifications

This element is shown in Figure 2.20.

Figure 2.20: Yagi antenna

Video receiver *RC832S*: this element is aimed to receive the analog video signal captured by the antenna and amplify it so that a following converter (Video to USB converter [7]) can turn it into digital stream. The antenna is connected to the latter via a coaxial cable [6]. Table 2.16 [22] shows video receiver and annex devices specs.

Video receiver Specifications	
Sensibility	<-95 dBm
Channels	48
Antenna connector	RP-SMA Male
Video standard	NTSC or PAL
Power	
Operating voltage	7 - 12 V DC
Physical	
Dimensions	80 x 54 x 15 mm
Wight	80 g
Video converter	
Video input	Composite, RCA audio, S-video
Video output	USB
Max. resolution	720 x 480, 720 x 576
Coaxial cable	
Antenna-side connector	N-TYPE Male
Receiver-side connector	RP-SMA Female

Table 2.16: Video receiver Specifications

Figures 2.21, 2.22 and 2.23 show respectively the aforementioned devices.

Figure 2.21: Video receiver

Figure 2.22: Video converter

Figure 2.23: Coaxial cable

2.5.6 Final avionics configuration

As an outcome of the above mentioned considerations, it is now possible to define the final and complete avionics configuration chosen for this project. The schematic shown in Figure 2.24 showcases the the architecture of the on-board system, putting in evidence the mutual connections among the various devices, specifying the interfaces or protocols and stating the information exchanged over each of those: the arrows

indicate the direction of data flow, identifying the inputs for each element. Solid lines identifies wired connection, while dashed ones refer to radio link.

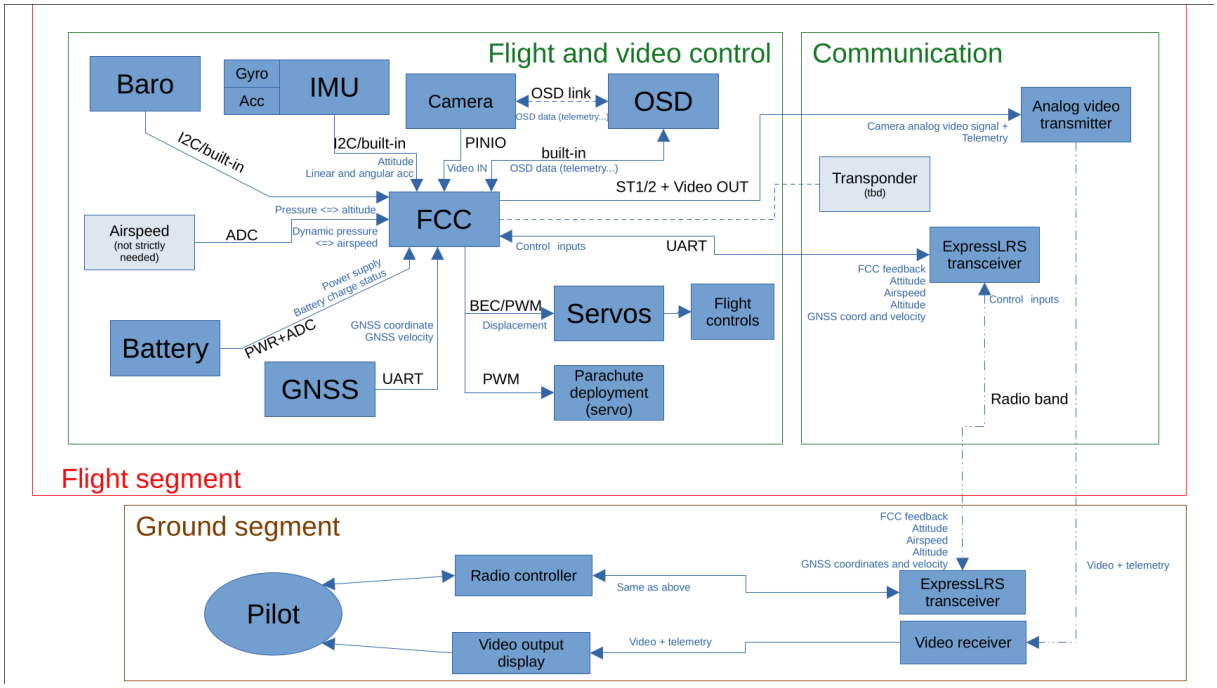

Figure 2.24: Final avionics configuration

As it is possible to see, the scheme is divided into two main sections: *Flight segment* and *Ground segment*. As the names suggest, the former identifies all the equipment that needs to be installed on the aircraft and, as such, subjected to weight and size limitations. The latter, instead, is related to those devices that will constitute the ground equipment and take care of establishing radio communication, sending control inputs and receiving telemetry and video signals. Within the *Flight segment* section, it is possible to notice two further subsections, named *Flight and video control* and *Communication*. These two groups respectively refer to the set of devices necessary for the actual operating of the avionic system and to establish a radio link with the ground equipment.

Chapter 3

Aerodynamic design

3.1 The Vortex Lattice Method

To the aim of carrying out the complete design of this model aircraft, an aerodynamic study has to be performed. Considering the low speed regime this glider will be subjected to, it is possible to employ a potential flow-based model. This method makes it possible to study the aerodynamic properties of a body considering a simplified version of the Navier-Stokes equations. This is possible within the applicability domain of certain hypothesis:

- the flow must suit the steady-state approximation. This implies that the solution to this model will not be time-dependent: this reduces the overall complexity of the mathematical problem - removing every time-dependent element from the equations, but, on the other hand, makes not possible to study transient conditions;
- considering flows characterized by low Mach numbers, an important aspect comes into play: incompressibility. As stated in the previous chapters, the maximum possible Mach number for this application has to be lower than or equal to 0.3. This means that flow density can be considered constant and equal to the free stream conditions. In terms of equations, this reduces the mass conservation law to the following:
$$\nabla \cdot \mathbf{V} = 0 \tag{3.1}$$
where $\mathbf{V}$ is the velocity vector;
- In the case of flows characterized by high Reynolds numbers, the effects of viscosity and thermal conductivity are confined to thin regions localized along the body surfaces and in the wake, and thus negligible in most of the domain. In this case, the fluid can be considered as inviscid [4]. This means that the viscous stresses caused by velocity gradients can be discarded and, as a consequence of this, the diffusive terms can be removed from the Navier-Stokes equations. This has the effect of eliminating the stress tensor term from the momentum equation and decoupling this equation and the energy conservation (i.e. thermal equation) one;
- an additional condition imposed on the velocity vector is that of irrotationality. This amounts to saying that the vorticity ω is null in every point of the considered domain:
$$\omega = \nabla \times \mathbf{V} = 0 \tag{3.2}$$

These hypothesis allow for the definition of a scalar quantity: velocity potential ϕ. Its relationship with the velocity vector is described by the following equation:

$$\nabla\phi = \mathbf{V} \tag{3.3}$$

Thanks to these assumptions, it is eventually possible to re-write the Navier-Stokes vectorial equation into a single, scalar relation for the velocity potential: the so called *Laplace equation*:

$$\nabla^2\phi = 0 \tag{3.4}$$

As reported in Renzo Arina's *Fundamentals of Aerodynamics* [4], this law turns the problem of solving a complete fluid motion field - in which scalar and vectorial equations have to be solved simultaneously and the thermal equation is coupled with the momentum one - into single-variable, linear, scalar problem where the unknown is the velocity potential (also called potential function). Once the solution for this quantity is determined, it is immediate to calculate the velocity vectorial field using equation 3.3. From this, it is then possible to determine the pressure field using Bernoulli equation that, under the aforementioned hypothesis can be written in the following form:

$$p + \frac{1}{2}\rho V^2 = const = p_0 \tag{3.5}$$

where, p is the static pressure, $q = \frac{1}{2}\rho V^2$ is the dynamic pressure and p_0 is the total pressure which, in this scenario, is constant in every point of the considered domain. In presence of these hypothesis, it is common practice to refer to this kind of flow as *potential flow*.
In this framework, when approaching the study of a general fluid motion field, it becomes useful to define a set of elementary fluid fields that, if properly combined, can be used to describe more general flows. In this regards, it results that in some cases it's possible to define the velocity distribution and obtain the corresponding expression for the potential function based on its definitions. Furthermore, by applying the principle of superposition of effects, combinations of these simple fields provide the potential expression for more complex cases [4]. In particular, it is possible to demonstrate that the flow field surrounding a lifting surface can be represented through the combination of a series of vortex lines immersed in a uniform current field. Each of those are meant to represent the local disturbance to the flow field caused by the presence of the surface and are characterized by a specific magnitude. In order to correctly represent the effect of wake vortexes, as well as extremities vortexes, these lines are composed of a portion perpendicular to the free stream direction - representing the surface itself effect on the flow - and of two offshoots parallel to the flow - modeling the wake effects. This structure is often referred to as *horseshoe vortexes*. The schematic in Figure 3.1 represents a segment of a wing on which a *horseshoe vortex* is placed on a portion of its surface.

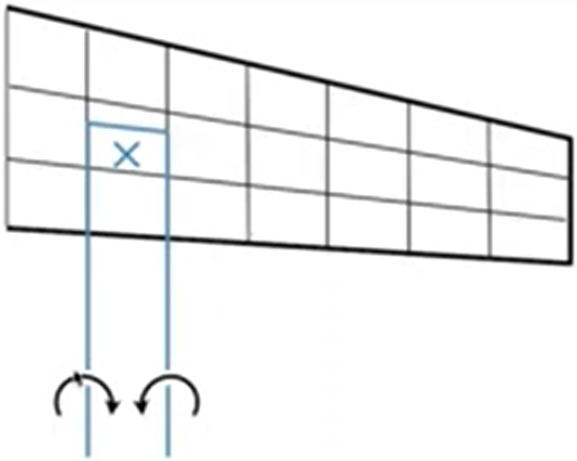

Figure 3.1: Vortex lines schematic

As the image suggests, if this structure is replicated to the point of completely covering the interested surface, a thick grid of vortex lines would result and this could be employed to properly study the aerodynamic properties of the enclosed body. This model takes the name of *Vortex Lattice Method (VLM)* and, for the objectives of this project will be adopted as the main fluid dynamic simulation and evaluation tool.

3.1.1 The OpenVSP environment

To the end of applying the aforementioned model to calculate relevant quantities for the design process, an analysis tool released by NASA has been used: OpenVSP. OpenVSP is a parametric aircraft geometry tool. It allows the user to create a 3D model of an aircraft defined by common engineering parameters [1], define free stream flow conditions and, eventually, calculate its properties giving aerodynamic coefficients

and derivatives as an output. Within this environment it is also possible to define mass properties of the vehicle structural components and of on-board equipment: this allows a realistic study of static and dynamic qualities. This software offers a graphic user interface that makes it easy to create the 3D model of the aircraft and the output is given through a user-friendly plain-text file format.

3.2 Fundamentals of flight mechanics

Within this section and the following some of the crucial aspect of flight mechanics will be covered. In the first place, the aircraft will be studied considering a body-fixed reference frame in which:

- X_B axis lies in the symmetry plane of the aircraft and is oriented positively towards the nose;
- Y_B axis lies in the symmetry plane and is oriented positively downward;
- Z_B axis completes the right-handed triad (oriented positively to the pilot's right).

As a consequence of this, the aerodynamics moments and angular velocities are defined as follows:

- along the roll (X_B) axis: the aerodynamic moment is l and the roll velocity p. Their are considered positive if oriented towards a right-hand bank;
- along the pitch (Y_B) axis: the moment is called m and the pitch rate q. They are oriented positively towards the nose-up attitude;
- along the yaw (Z_B) axis: the corresponding moment is n and the yaw velocity r. Their value is considered positive towards a nose-right direction.

On the other hand, lift L and drag D forces are, by their definition, perpendicular and parallel to the free stream wind direction: to take into account their effect, they will be decomposed along these axis. Picture in Figure 3.2 [3] represents the adopted reference frame. It is also possible to notice the definition of the angle of attack (α) and the side-slip angle (β) with respect to the free stream velocity (V_∞). u_B, v_B and w_B show a decomposition of the latter along the frame axis. Since, otherwise specified, the only

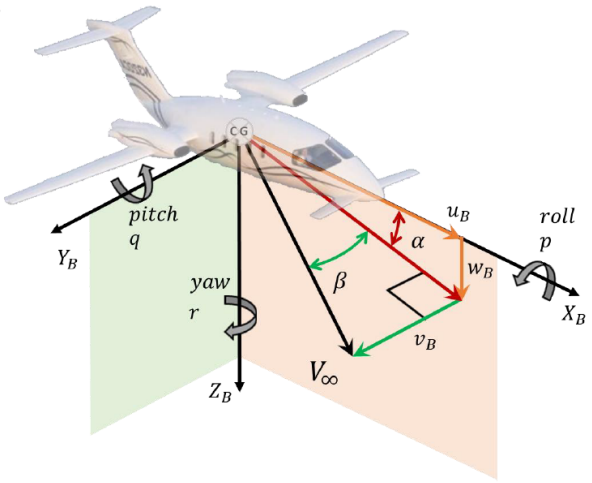

Figure 3.2: Body-axis reference frame

reference frame adopted in this study is the body-fixed one, subscript symbols will not be reported in the continuation of this discussion.
Within the framework of aerodynamic studies, it si common practice to operate with non-dimensional quantities. This means that pressures, forces, moments are scaled with the characteristics quantities as reported in Table 3.1.

Quantity	Reference quantity	Corresponding coefficient
Pressure p	Dynamic pressure $q = \frac{1}{2}\rho V_{eq}^2$	$C_p = \frac{p}{q}$
Force F	Reference force $F_{ref} = \frac{1}{2}\rho V_{eq}^2 S_{ref}$	$C_F = \frac{F}{F_{ref}}$
Moment M	Reference moment $M_{ref} = \frac{1}{2}\rho V_{eq}^2 S_{ref} c$	$C_M = \frac{M}{M_{ref}}$

Table 3.1: Dimensionless quantities

When considering derivatives, other reference quantities are used to obtain their non-dimensional expressions. These quantities are reported in Table 3.2.

Quantity	Reference quantity
Time t	Reference time for longitudinal plane $t^* = \frac{c}{2V_\infty}$
Time t	Reference time for lateral-directional plane $t^* = \frac{b}{2V_\infty}$

Table 3.2: Derivative reference quantities

Within the above reported lists, some relevant quantities are mentioned:

- the following relation holds: $V = V_\infty = V_{eq}$. Velocity is defined as that of the steady-state equilibrium condition;
- S_{ref} is the reference wing surface;
- c is the mean aerodynamic chord, or MAC;
- b is the wingspan.

To sum up the aforementioned concepts a brief example is reported hereafter: let's consider lift as an aerodynamic, dimensional force: L. Downstream of this it is possible to define the following non-dimensional quantities:

- lift coefficient: $C_L = \frac{L}{\frac{1}{2}\rho V^2 S}$;
- lift derivative w.r.t. angle of attack: $L_\alpha = \frac{\partial L}{\partial \alpha}$;
- lift coefficient derivative, aerodynamic derivative: $C_{L\alpha} = \frac{\partial C_{L\alpha}}{\partial \alpha}$.

3.2.1 Static stability and equilibrium

Coming to consider more specific topics, the following section describes the physical model adopted to study the main mechanical properties of the aircraft being designed. As a start point, a free-body diagram is used to study the steady-state equilibrium condition. The corresponding scheme is shown in Figure 3.3.

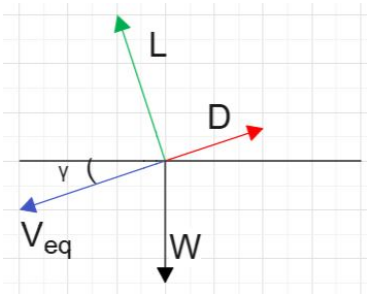

Figure 3.3: Longitudinal free-body diagram

Where γ is the angle between the velocity vector and the horizon, taking the name of *flight-path angle*. Considering that the zero-lift and zero-pitching moment lines may not be coincident with the X body axis - with respect to which the angle of attach (AoA) is considered, the lift coefficient and the pitching moment coefficient are expressed as:

- $C_L = C_{L0} + C_{L\alpha}\alpha$
- $C_m = C_{m0} + C_{m\alpha}\alpha$

where C_{L0} and C_{M0} are respectively the lift and moment coefficient evaluated at a zero AoA condition. The pitching moment is calculated considering the aircraft center of gravity (C.G.) as the pole. The steady-state condition for a this aircraft performing a gliding symmetric $\beta = 0$ flight is described by the following set of equations, in which the first two equations constitute an equilibrium of forces while the last one expresses a moment equilibrium along the pitch axis.

$$\begin{cases} W\cos\gamma = \frac{1}{2}\rho V^2 S C_L \\ \frac{1}{2}\rho V^2 S C_D + W\sin\gamma = 0 \\ \frac{1}{2}\rho V^2 S c\, C_m = 0 \end{cases} \tag{3.6}$$

Where:

- $W = mg$ is the weight corresponding to total aircraft mass m;
- C_L, C_D and C_m dependency on α is obtained as a result of numerical analysis;
- the unknowns to this problem are the set of variable describing the aircraft flight state: γ, α and V.

Furthermore, from the last equation of set 3.6, it is possible to derive the condition for the static longitudinal stability. Considering a small perturbation of α value, it results that the aircraft would respond in the sense of minimizing the disturbance only if the $C_{M\alpha}$ value is lower than zero. In addition, to ensure an upright, positive attitude ($\alpha > 0$) flight condition at the equilibrium state, it is also necessary that $C_{M0} > 0$. The following summarizes the just mentioned conditions:

$$\begin{cases} C_{m0} > 0 \\ C_{m\alpha} < 0 \end{cases} \tag{3.7}$$

When considering a delta-wing configuration, it is possible to demonstrate what follows:

- C_{m0} corresponds to the pitching moment coefficient relative to the C.G. of the wing-body assembly;
- $C_{m\alpha}$ can be expressed with the following relation:

$$C_{m\alpha} = C_{L\alpha}\frac{x_G - x_N}{c} \tag{3.8}$$

  where x_G and x_N are respectively the distances of the aircraft C.G. and neutral point from the nose.

Downstream of this, it is of immediate deduction from equation 3.8 that the geometric condition to ensure longitudinal static stability is:

$$x_G < x_N \tag{3.9}$$

Equation 3.9 poses a constraint over the maximum aft position of the C.G. It is of common use to define the static stability margin as:

$$K_n = \frac{x_N - x_G}{c} \tag{3.10}$$

this parameter is an index for the longitudinal static stability of a certain platform and, thanks to its non-dimensional definition, it is useful compare different aircraft configurations from this standpoint. This property is obviously ensured by $K_n > 0$.
Regarding the upright flight condition (the first line of set 3.7), various solutions are available, as its reported on Piero Gili's [20] *Fundamentals of Flight Mechanics* notes:

- using a reversed-cambered airfoil, or
- adopting a twisted and swept wing.

These are the conditions that will be used to assess the static stability properties of the glider. Similarly to this, static stability can be studied along the lateral-directional axis as well. Considering the adopted reference frame, with the respective aerodynamic actions and angles, it is possible to state that static stability relative to these planes is ensured if:

- $C_{l\beta} < 0$: dihedral effect, that determines lateral static stability;
- $C_{n\beta} > 0$: vertical stabilizer effect, that determines directional static stability.

As it will be discussed afterwards, the aerodynamic and geometric features of the studied model - such as aerodynamic coefficients and derivatives, neutral point position, C.G. position and polar curves - will be evaluated using the OpenVSP environment and will be subjected to an optimization process to the aim of obtaining a suitable aircraft configuration in compliance with the assigned requirements.

3.3 Flight dynamics and the State-Space model

Along with the study of the vehicle steady state and static characteristics, it is of fundamental importance evaluating the dynamic properties as well. To this end, a dynamic model of the aircraft is presented hereafter. In the first place, it is necessary to define the reference frames used in this analysis. The first one is the North, East, Down (NED) reference frame: this coordinate system defines the basic inertial reference frame with respect to which the dynamics of the aircraft is studied. It is fixed to the Earth surface and its axis point respectively towards the north pole, east and the center of the planet. Figure 3.4 [3] represent the NED reference frame relatively to a Earth-centered system.

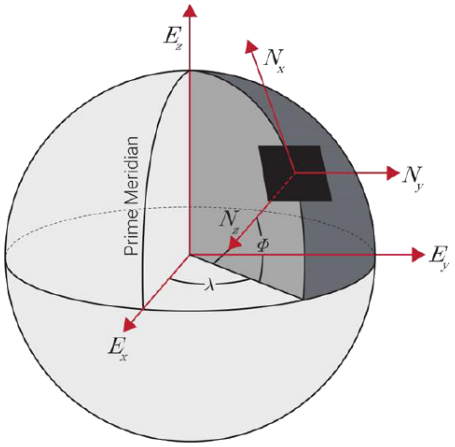

Figure 3.4: NED reference frame

The second frame is the above mentioned body-fixed one. The relation between these two coordinate systems is described by *Euler angles*. These quantities constitute an ordered set of angles that, stating subsequent rigid rotations around axis of succeeding terns, allows a uniquely determined transposition relation between the two frames. These angles are defined as follows:

- *heading angle*: ψ;
- *elevation angle*: θ;
- *bank angle*: ϕ.

Following this order of rotation, it is possible to demonstrate the following correlation between the time derivative of Euler angles and the angular velocities around body axis. These equations, written in matrix form, take the name of *Gimbal equations*:

$$\begin{Bmatrix} \dot{\phi} \\ \dot{\theta} \\ \dot{\psi} \end{Bmatrix} = G^{-1} \begin{Bmatrix} p \\ q \\ r \end{Bmatrix} = \begin{bmatrix} 1 & \frac{\sin\phi\,\sin\theta}{\cos\theta} & \frac{\cos\phi\,\sin\theta}{\cos\theta} \\ 0 & \cos\phi & -\sin\phi \\ 0 & \frac{\sin\phi}{\cos\theta} & \frac{\cos\phi}{\cos\theta} \end{bmatrix} \begin{Bmatrix} p \\ q \\ r \end{Bmatrix} \tag{3.11}$$

Downstream of this, the equilibrium equations for the aircraft, written in the body-fixed reference frame, can be expressed as:

$$\begin{cases} F_x = m\big(\dot{u} + qw - rv\big) \\ F_y = m\big(\dot{v} + ru - pw\big) \\ F_z = m\big(\dot{w} + pv - qu\big) \\ L = J_x\dot{p} - r\dot{J}_{xz} + qr(J_z - J_y) - J_{xz}pq \\ M = q\dot{J}_y + pr(J_x - J_z) - J_{xz}(p^2 - r^2) \\ N = -p\dot{J}_{xz} + r\dot{J}_z + pq(J_y - J_x) + J_{xz}qr \end{cases} \tag{3.12}$$

where:

- $F_{x,y,z}$ is the decomposition of forces along the body axis;
- L, M, N are the moments around the same axis;
- $J_{x,y,z,xy,xz,yz}$ are the moment of inertia relative to the considered reference frame.

These two sets of equations allows for a detailed study of the aircraft dynamics: when substituting to the forces and moments their expressions with respect to the kinematic unknowns (u, v, w, p, q, r), a closed set of equations would result. Once obtained these quantities, it is possible to evaluate navigation parameters throughout mathematical integration of the latter. Furthermore, to determine the actual attitude of the aircraft equations 3.11 can be used to this end.

3.3.1 Small Perturbation Theory

Coming to consider more specific aspects of this model, it would result particularly interesting to undertake an analysis of the intrinsic dynamics properties of the described body. To this end, modal analysis is found to be useful. The first step to perform to conduct such a study is that of linearize the equations of motion in order to obtain a system of linear differential equations. In this matter the *Small Perturbation Theory* is introduced.
This approach can be applied under the following conditions:

- the initial condition is a steady-state equilibrium one;
- variable deviations from their equilibrium values must be small enough so that the derivatives of the latter can be approximated with a constant value (i.e. constant aerodynamic derivatives);
- let X be an arbitrary quantity and X_0 its initial value. Its generic value should be represented as:

  $$X = X_0 + \Delta X$$

  where ΔX is the deviation from the initial value;
- the dynamic model has to be re-written to take into account only the deviation part of the total variable value.

In this context, then, the above mentioned perturbation is intended around an equilibrium condition. The solution of the linearized system describes the evolution over time of such deviations, that can be superimposed to the initial condition to obtain the total value solution. This approach is highly useful because it provides reliable results both for the study of stability and for the analysis of the aircraft response (to pilot inputs or external disturbances). The limitation of the small-disturbance theory is that of in presence of significant deviations with respect to the reference condition, the solution loses reliability. Even significant disturbances (e.g., a gust) may not necessarily lead to substantial variations of the variables involved (e.g., angular velocities). The great advantage is the linearization of the set of nonlinear differential equations and of the aerodynamic forces and moments [3].

If applying this method to equation 3.12 and eliminating every second order element, the result is:

$$\begin{cases} \Delta F_x = m(\dot{u} + qw_{eq}) \\ \Delta F_y = m(\dot{v} + ru_{eq} - pw_{eq}) \\ \Delta F_z = m(\dot{w} - qu_{eq}) \\ L = J_x\dot{p} - \dot{r}J_{xz} \\ M = \dot{q}J_y \\ N = -\dot{p}J_{xz} + \dot{r}J_z \end{cases} \tag{3.13}$$

As an additional simplification, the following conditions are assumed [1]:

- $u_{eq} = u_0 \simeq V_\infty$;
- $v_{eq} = 0$, hence giving $\beta = 0$;
- $w_{eq} \simeq 0$;
- p_{eq}, q_{eq}, $r_{eq} = 0$

Furthermore, considering $\theta_{eq} = \phi_{eq} = \psi_{eq} = 0$, and applying the just described approximations, it is possible to state that:

$$\begin{cases} p = \dot{\phi} \\ q = \dot{\theta} \\ r = \dot{\psi} \end{cases} \tag{3.14}$$

Observing the set of equations 3.13, it si possible to notice that the first, third and fifth expressions only involve quantities relative to the longitudinal plane, while the remaining ones contain mixed terms of both lateral and directional plane. This means that within the hypothesis of small perturbation the phenomena regarding the longitudinal plane can be studied separately from those of the lateral-directional one. This puts in evidence a physical independence of the former over the latter that, conversely, cannot be further decoupled.

3.3.2 Longitudinal plane

Considering the dynamics that develops over the longitudinal plane, it results particularly advantageous referring the equations to a stability reference frame. In order to obtain a easily-scalable representation of the aircraft dynamics, equation 3.13 is combined with 3.14 and the resulting system is scaled with the aforementioned reference quantities. In addition, identifying the vector defined as $x = [\Delta V \ \Delta\alpha \ q \ \theta]^T$ as the set of state variables for this system, it is possible to express the resulting equations in matrix form as:

$$\begin{Bmatrix} \frac{d\hat{V}}{dt} \\ \frac{d\alpha}{dt} \\ \frac{d\hat{q}}{dt} \\ \frac{d\hat{\theta}}{dt} \end{Bmatrix} = A_{long} \begin{Bmatrix} \Delta\hat{V} \\ \Delta\hat{\alpha} \\ \hat{q} \\ \hat{\theta} \end{Bmatrix} \tag{3.15}$$

where:

$$A_{long} = \begin{bmatrix} -\frac{C_{DV}}{2\mu} & \frac{C_{L_{eq}} - C_{D_\alpha}}{2\mu} & 0 & 0 \\ -\frac{C_{L_V} + 2C_{w_{eq}}}{2\mu + C_{L_\alpha}} & \frac{C_{L_\alpha} + C_{D_{eq}}}{2\mu + C_{L_\alpha}} & -\frac{2\mu - C_{L_{\dot{q}}}}{2\mu + C_{L_\alpha}} & 0 \\ \frac{1}{\hat{I}_{YY}}\left[C_{M_V}(C_{L_V} + 2C_{w_{eq}}) - \frac{C_{M_\alpha}(C_{L_V} + 2C_{w_{eq}})}{2\mu + C_{L_\alpha}}\right] & \frac{1}{\hat{I}_{YY}}\left[C_{M_\alpha}(C_{L_\alpha} + C_{D_{eq}}) - \frac{C_{M_\alpha}(C_{L_\alpha} + C_{D_{eq}})}{2\mu + C_{L_\alpha}}\right] & \frac{1}{\hat{I}_{YY}}\left[C_{M_q}(2\mu - C_{L_q}) - \frac{C_{M_\alpha}(2\mu - C_{L_q})}{2\mu + C_{L_\alpha}}\right] & 0 \\ 0 & 0 & 1 & 0 \end{bmatrix} \tag{3.16}$$

[1] the u_{eq} and w_{eq} relations become exact equalities if a *stability reference frame* is adopted: this system is fixed to the aircraft as the body one, but it is rotated around the Y axis so that the X axis is parallel to wind direction

This representation takes the name of *State-Space model* and matrix A_{long} - the state matrix - can be used to perform modal analysis on the dynamics properties of the aircraft along the longitudinal plane. To this end it is necessary to evaluate eigenvalues and eigenvectors of the state matrix. The former define the *modes* characteristics, meaning its damping or amplification coefficients and oscillatory features. The latter, instead, provide a description of the extent to which each variable is affected by each mode. Considering conventional aircraft properties, it is possible to state that the dynamic response to a small perturbation is composed - and is the superposition - of the following modes:

- *short period mode*: this is an oscillatory mode, represented by a complex conjugate pair with negative real part. Generally it's a high-frequency and heavily damped mode. Observing the associated eigenvector, the following features apply to this mode:
  - $\theta \simeq \Delta\alpha \Rightarrow \gamma \simeq 0$;
  - θ, $\Delta\alpha$ and $\Delta\hat{V}$ can be considered in phase;
  - θ and $\Delta\alpha$ can be considered as the most relevant variables to this mode;
  - $\Delta\hat{V}$ effect is negligible [3];
- *phugoid mode*: this is a low frequency moderately damped oscillatory mode. The following features can be observed:
  - $\Delta\alpha$ effect is negligible;
  - $\theta \simeq \gamma$;
  - θ and $\Delta\hat{V}$ can be considered as teh most relevant variables to this mode;
  - $\Delta\hat{V}$ is in opposition with $\Delta\alpha$ and in quadrature with θ [3];

Further details on this modes and respective diagrams will be showed in the following sections.

3.3.3 Lateral-directional plane

Similarly to what has been done for the longitudinal plane, the lateral-directional one can be studied using the state-space method. In this case, the state variables are those defining the vector $x = [\beta\ \hat{p}\ \hat{r}\ \phi\ \psi]^T$. Thus, the linearized equations can be written in matrix form as:

$$\begin{Bmatrix} \frac{d\beta}{d\hat{t}} \\ \frac{d\hat{p}}{d\hat{t}} \\ \frac{d\hat{r}}{d\hat{t}} \\ \frac{d\phi}{d\hat{t}} \\ \frac{d\psi}{d\hat{t}} \end{Bmatrix} = A_{lat-dir} \begin{Bmatrix} \beta \\ \hat{p} \\ \hat{r} \\ \phi \\ \psi \end{Bmatrix} \tag{3.17}$$

where:

$$A_{lat-dir} = \begin{bmatrix} \frac{C_{Y_\beta}}{2\mu} & \frac{C_{Y_p}}{2\mu} & \frac{C_{Y_r}-2\mu}{2\mu} & \frac{C_{w_{eq}}}{2\mu} & 0 \\ \frac{C_{l_\beta}}{\hat{I}'_X} + \hat{j}'_{zx}C_{n_\beta} & \frac{C_{l_p}}{\hat{I}'_X} + \hat{j}'_{zx}C_{n_p} & \frac{C_{l_r}}{\hat{I}'_X} + \hat{j}'_{zx}C_{n_r} & 0 & 0 \\ \frac{C_{n_\beta}}{\hat{I}'_Z} + \hat{j}'_{zx}C_{l_\beta} & \frac{C_{n_p}}{\hat{I}'_Z} + \hat{j}'_{zx}C_{l_p} & \frac{C_{n_r}}{\hat{I}'_Z} + \hat{j}'_{zx}C_{l_r} & 0 & 0 \\ 0 & 1 & 0 & 0 & 0 \\ 0 & 0 & 1 & 0 & 0 \end{bmatrix} \tag{3.18}$$

Performing the same modal analysis over the $A_{lat-dir}$ matrix as done for the longitudinal plane, it is possible to infer the presence of the following dynamic characteristics:

- *heading mode*: the corresponding eigenvalue is null and it only affects the ψ variable. This mode doesn't feature any oscillations;

- *roll mode*: the only relevant variable is ϕ and, as it will be discussed later, the study of this mode is of relevance to analyze the aircraft response upon roll command. It usually is a damped, non-oscillatory mode;
- *spiral mode*: this damped - or slightly amplified - mode mainly affects ϕ and ψ variables, while having a significant lower effect on β. The evolution of this mode, if not counteracted by the pilot, leads the aircraft in a spiral trajectory with increasing bank angle;
- *dutch-roll mode*: this mode involves perturbations on each state variable of this plane. It's oscillatory feature requires it to be damped, in order to ensure suitable aircraft controllability characteristics.

Further details on this modes and respective diagrams will be showed in the following sections.

3.4 Fuselage effects

Since the solving algorithm implemented in the OpenVSP software exploits the vortex lattice method, the representation of a bluff body (such as the fuselage) by means of median planes perpendicular to each other may not be accurate. Therefore, numerical analysis have been carried out considering only the aerodynamic surfaces (wing and vertical tail). This made it possible to obtain an evaluation of the aerodynamic polar curve and aerodynamic derivatives considering the aircraft as a *flying wing* configuration. The effect of the fuselage to the longitudinal plane has been considered downstream of this using the theories of Munk and Multhopp for fuselages. The fuselage is considered not to have camber and can be assumed symmetric with respect to the horizontal and vertical mid-planes. This allows the body axes of the fuselage and the wing to be coincident. In particular, the following models have been considered:

- regarding the pitching moment coefficient at zero incidence (C_{m0}), the Multhopp's theory has been used:

$$C_{m0f} = \frac{k_2 - k_1}{36.5Sc} \sum_{x=0}^{x=l_f} w_f^2(\alpha_{0w} + i_f)\,\Delta x$$

  The parameters in this formula have been obtained obtained from the model designed in OpenVSP and by exploiting the assumptions on the fuselage mentioned above. The reference quantities are the dynamic pressure at the equilibrium velocity of the aircraft without controls at sea level (defined as the *trim* condition), the wing surface area and the mean aerodynamic chord.

- for the derivative of the pitching moment coefficient ($C_{M\alpha}$), Munk's theory was used:

$$C_{M\alpha} = \frac{2 \cdot k_m \cdot Vol}{S \cdot \bar{c}}$$

  This law was chosen since Multhopp's theory considers the effect of wing downwash on the fuselage, which in this case is not relevant because the wing extends along its entire length [3].

- regarding the contribution of the fuselage to aerodynamic resistance, the effect was neglected due to the fact that the force generated by a streamlined body is much smaller than the drag of the aircraft or the lift force generated by the wing [2].
- the effect of the fuselage on the lateral-directional plane was neglected as well, as an indication.

The coefficients thus obtained were used to correct those derived from the analysis of the isolated wing in order to take into account the contribution of the fuselage.

3.5 The startup point

Once this theoretical background has been completely defined, it is possible to move to the actual design process of the aircraft. As already mentioned, this glider takes the shape of *delta wing* aircraft. This means that the main element composing it will be a wing, a vertical stabilized and, of course, a fuselage aimed to create the main avionic bay of the vehicle. The start point for the evaluation and optimization of the aeromechanical properties has been very common object, something that everybody can interact with on a daily basis: a paper plane. Paper planes are very interesting objects from this standpoint: a lot of the features required by this project are actually present in this rudimentary model aircraft. Some of those are the following:

Figure 3.5: Paper plane

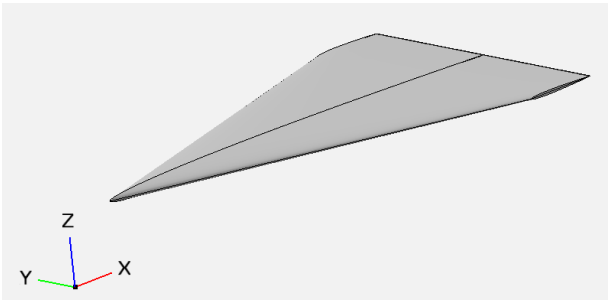

Figure 3.6: Paper plane OpenVSP model - perspective view

- it features a delta wing, that is the kind of lifting device needed by this project;
- since constituted by a sheet of paper, the wing can be assimilated to a thin flat plate. For this reason, it has been seen as a good start point on which compute iterations to the end of defining the most suitable airfoil;
- from an empirical perspective, paper planes are fairly stable platforms, this means that studying their aerodynamic and mass properties and replicating them on the studied model can be a good start point to build an aircraft configuration with good aeromechanical features.

Coming to more detailed aspects, the kind of paper aircraft considered is the most "classical" one, shown in Figure 3.5. The first step has been that of creating a digital model of this aircraft within the OpenVSP environment. Figure 3.6 shows a perspective view of the model. Dimensions for this model have been taken from the actual paper object and are reported in Figure 3.7. Values are expressed in centimeters. Eventually, to represent an ideal thin plate, a symmetric airfoil has ben set: NACA 0005. This shape is thin enough to be assimilated to the sheet the real paper plane is composed of. The parameters shown in Table 3.3 have been set to run the first numerical analysis.

Mass	5 g
Reference chord (MAC)	20.22 cm
Reference surface	292.4 cm^2
Altitude	0 m (sea level)

Table 3.3: Paper plane features

In this matter, a study of the polar curves has been carried out. Results are presented in Figure 3.8e

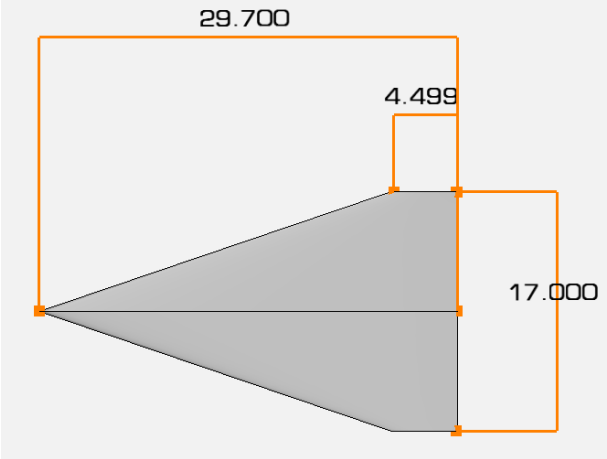

Figure 3.7: Paper plane OpenVSP model - dimensions

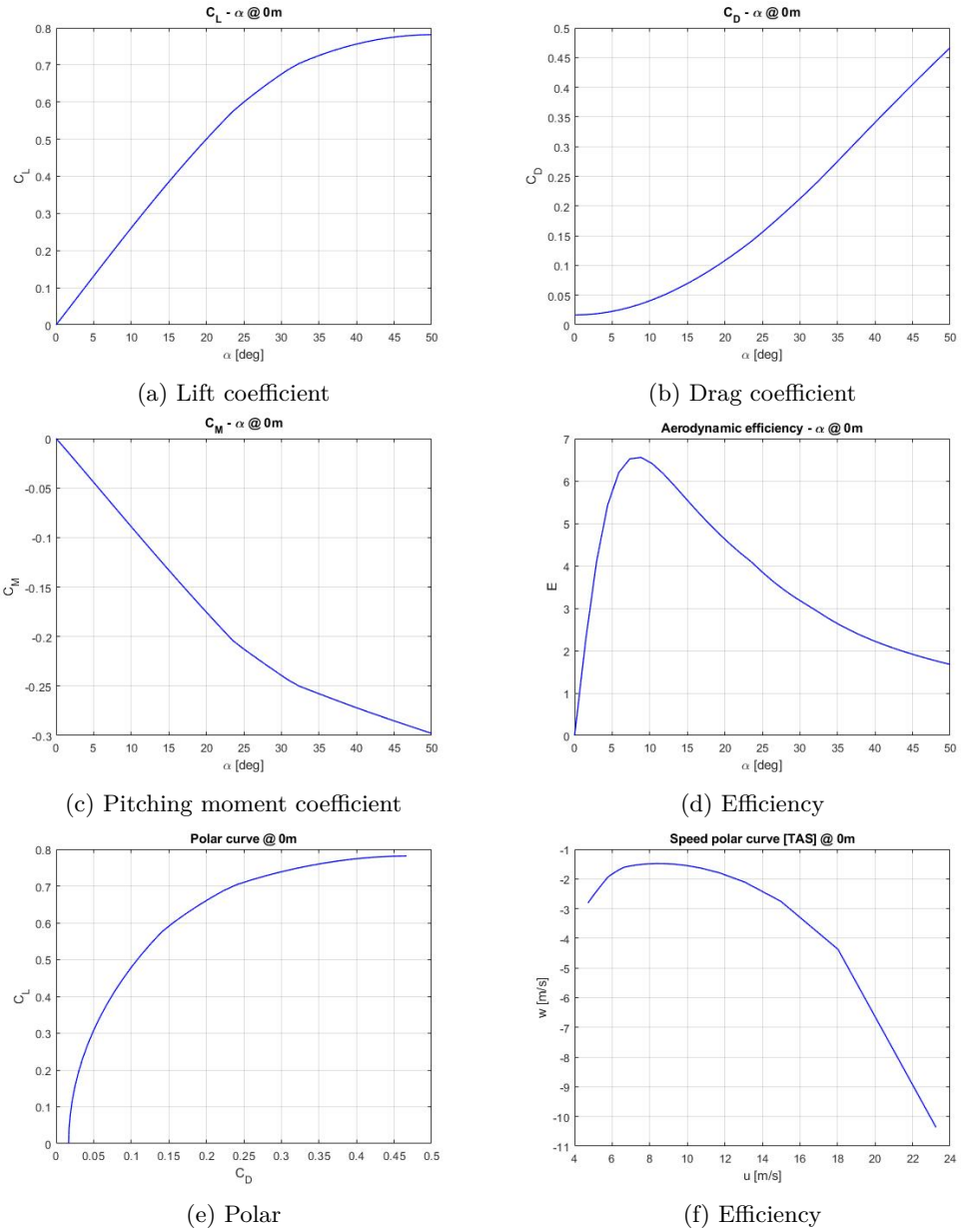

(a) Lift coefficient

(b) Drag coefficient

(c) Pitching moment coefficient

(d) Efficiency

(e) Polar

(f) Efficiency

Figure 3.8: Paper plane polar curves

These charts provide a baseline upon which the following studies will be carried out. As it is possible to notice, in these curves the stall phenomenon is not accurately represented: this is because the VLM doesn't consider the viscous effects that induce boundary layer instability, transition and separation. However, this does not compromise the validity of the results because the delta wing configuration shows good performances also at high AoA flight conditions (up to 30° - 40°).
As it is possible to see, the reported curves are analogous to those of any conventional aircraft. Particular attention, though, must be payed for the pitching moment one (Figure 3.8c). As it is possible to notice, this curve shows that the C_{m0} parameter for this aircraft configuration is null; thus, the equilibrium incidence would result to 0 *deg*. This is a direct consequence of the symmetric characteristic of the considered airfoil. In order to obtain a positive value for this quantity, a cambered airfoil will be adopted. For the same purpose, also the presence of a wing twist will be introduced.

3.6 Preliminary shape

Downstream of the aforementioned evaluations, the following features have been introduced:

- wing twist: -10° twist at wing tip;
- cambered airfoil: NACA 1205. This feature, together with the previous one, has been considered to ensure a positive value to the C_{m0} parameter;
- fuselage: a solid body has been introduced: it is composed of a succession of elliptical sections and its shape has been qualitatively determined to the purpose of defining a suitable avionic bay;
- vertical stabilizer: this aerodynamic surface has been added to confer stability over the lateral-directional plane and to reach the configuration the glider will eventually have;
- ballast: an arbitrary ballast entity has ben added in proximity to the aircraft nose to adjust C.G. position and ensure longitudinal static stability.

Dimensions, in cm, of the just described configuration is reported in Figure 3.9a and 3.9b. Figure 3.10 shows a perspective view of this model.

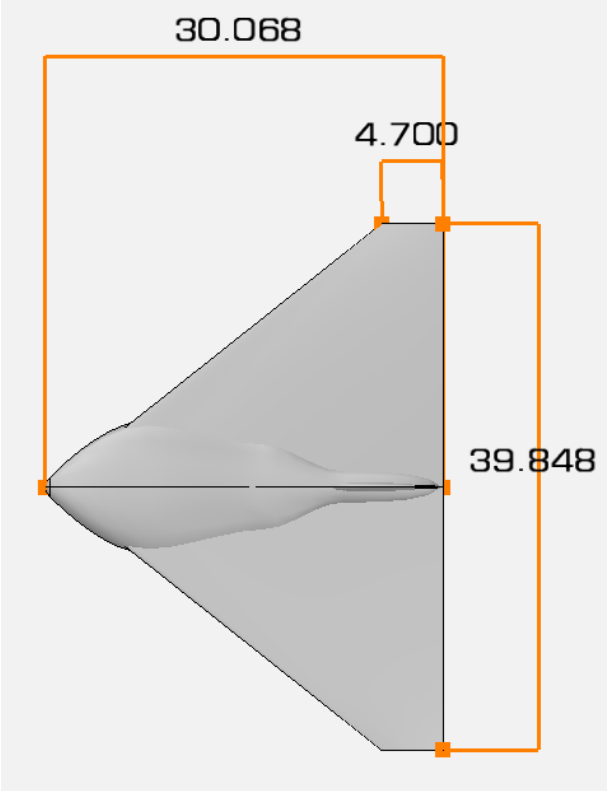

(a) Preliminary shape - top

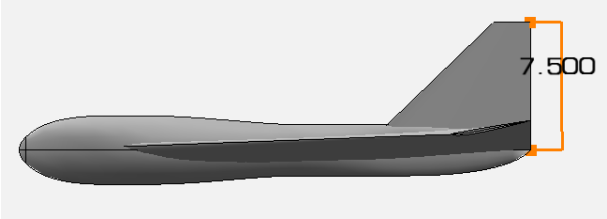

(b) Preliminary shape - left

Figure 3.9: Preliminary shape views

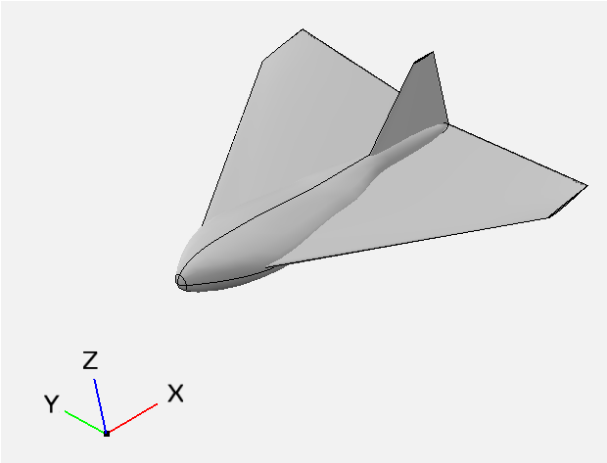

Figure 3.10: Preliminary shape - perspective

Further details of this configuration are reported in Table 3.4.

C.G. position	$x_G = 6.3$ cm
Neutral point position	$x_N = 16.04$ cm
Reference chord (MAC)	20.22 cm
Reference surface	688 cm^2
Altitude	0 m (sea level)
Mass	5 g

Table 3.4: Preliminary shape features

Downstream of these declarations, the analysis has been executed, providing the results shown in Table 3.5. The reported data define the equilibrium condition along the longitudinal plane. This set of quantities, and the respective values, describe the reference baseline on which flight characteristics will be evaluated. This equilibrium condition will be also referred to as *trim condition*.

Flight path angle	$\gamma = -17.9°$
AoA	$\alpha = 4.1°$
Speed	$V_{eq} = 4.28\ m/s$

Table 3.5: Preliminary shape - equilibrium conditions

As it is possible to notice, the equilibrium AoA is positive: this means that the effect of the inverted cambered airfoil and wing twist successfully managed to create the desired equilibrium condition. In this regard, the polar curves are presented in Figure 3.11e.

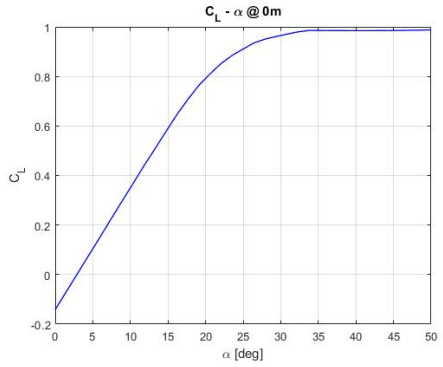

(a) Lift coefficient

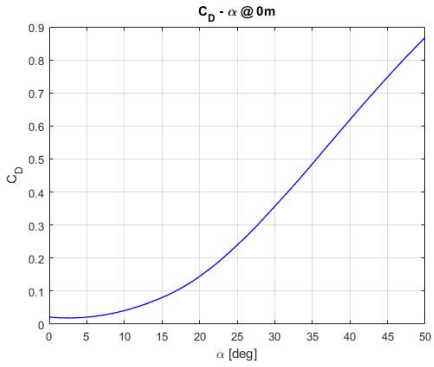

(b) Drag coefficient

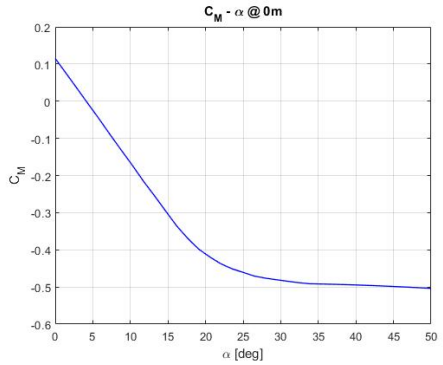

(c) Pitching moment coefficient

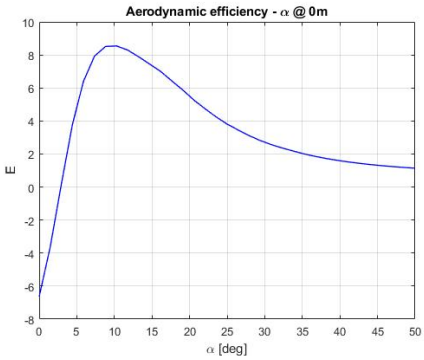

(d) Efficiency

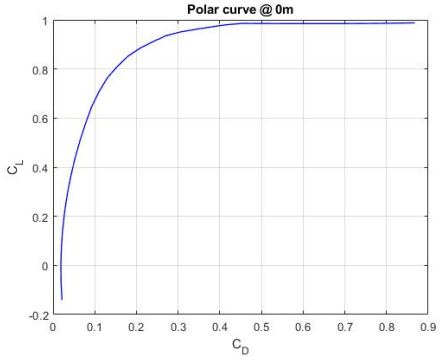

(e) Polar

Figure 3.11: Preliminary configuration polar curves

In agreement to what mentioned before, the $C_m - \alpha$ curve intersects the x-axis on a positive α value: this corresponds to the equilibrium AoA. In addition, the same plot shown a negative value of the $C_{m\alpha}$ derivative. This means that this configuration satisfies the requirement for static stability. This is in accordance with the fact that the overall center of gravity is closer to the nose than the neutral point is. As a further study, a dynamic stability modal analysis has been carried out. Considering the state matrices as in 3.16 and 3.18 and performing an eigenvalues analysis over them the following results have been obtained:

- **Longitudinal plane**: along this axis the eigenvalues of the corresponding matrix are:
  - $(-2.0817 \pm 2.2826i)$: this is a conjugate complex number and, as such, identifies an oscillatory mode. Since the real part is lower than zero, the dynamic evolution described by this parameter is damped. This eigenvalue is associated to the short period mode;
  - $(-0.0061471 \pm 0.25358i)$: similarly to the previous one, this parameter describes an oscillatory damped mode, characterized by lower frequency and damping coefficient than the latter. This represents the phugoid mode;

Thanks to the just reported statements, it is possible to assess that this first-attempt preliminary shape of the delta wing configuration presents good features of static and dynamic stability along the longitudinal plane.

- **Lateral-directional plane**: by analogy to what described in the previous point, the eigenvalues relative to this system are:
  - (0.00): as already mentioned the null eigenvalue doesn't identify an actual dynamic relevant mode: this is associated to the heading response;
  - (-5.469148): this real, negative value indicates a mode that doesn't involve any oscillation but that, after a perturbation has occurred, tends to bring the aircraft to the original equilibrium condition asymptotically. This eigenvalue is representative of the roll mode;
  - (-0.028246): similarly to the latter, this value indicates an asymptotic response. A smaller value, though, indicates less damped response, resulting in a longer transient from the perturbed condition to that of equilibrium. This represents the spiral mode;
  - $(-0.16367 \pm 0.84318\text{i})$: at last this damped, oscillatory mode is that of dutch-roll. Since its sever implication over controllability features, it is neccesary for this mode to be damped.

To the end of visualizing the aforementioned features and determine the dynamic properties of the associated modes at a glance, the tool of *root loci* is particularly useful. These are plots that represent the complex plane on which the eigenvalues are graphically marked. For this model, the root loci plots relative to the longitudinal an lateral-directional plane are reported in Figure 3.12.

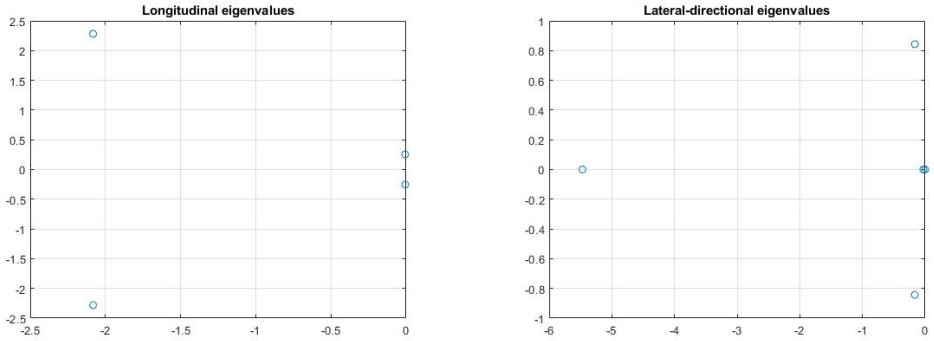

(a) Longitudinal plane (b) Lateral-directional plane

Figure 3.12: Preliminary configuration root loci

Qualitatively, this is the result this project aims to.

3.7 Scaling to the real model size

After having completed these preliminary studies, and having obtained the overall features this vehicle should have, it is possible to move from the first conceptual evaluations, to more specific design features for the final product. To this end, an initial geometric scaling of the model has been performed. In this context, limitations expressed by the requirements imposed to this project have been considered. Nevertheless, fuselage sizing has been conducted considering the volume of avionics devices it has to contain.

Wing	
Wingspan	$b = 0.5\ m$
Root chord	$c_{root} = 0.297\ m$
Tip chord	$c_{tip} = 0.047\ m$
LE sweep	$\Lambda_{LE} = 45°$
TE sweep	$\Lambda_{TE} = 0°$
Dihedral	$\Gamma = 6.5°$
Twist	$\Theta = -10°$
Airfoil	NACA 1205
Vertical stabilizer	
Height	$z_V = 0.12\ m$
Root chord	$c_{Vroot} = 0.15\ m$
Tip chord	$c_{tVip} = 0.035\ m$
LE sweep	$\Lambda_{V-LE} = 43.78°$
TE sweep	$\Lambda_{V-TE} = 0°$
Airfoil	NACA 0007
Fuselage	
Length	$0.30\ m$
Max width	$0.065\ m$
Max height	$0.055\ m$

Table 3.6: Scaled model geometry features

All the data reported have to be intended as first attempt ones. This means that they are the result of a mere scaling of the initial preliminary shape aimed to fit the dimensions needed for this project purposes. More specifically, the following aspects have been taken into consideration:

- all the on-board avionics have been modeled within the OpenVSP environment. Thus, a real-scale model entity has been created for each component to define with precision the required system bay size. This has been the main driving factor for fuselage sizing;
- wing twist, sweep angle and dihedral angle have been introduced considering their effects on aeromechanical qualities of the aircraft, as reported on Angelo Lerro's [3] *Meccanica del Volo* lecture notes;
- wing span has been set to a sufficiently high value to ensure a suitable wing surface and aspect ratio. The main reason for this is that of creating a sufficiently high lifting area to decrease wing loading, hence reducing overall flight speed. In addition, a high aspect ratio configuration provides the aircraft with good gliding properties in terms of aerodyanamic efficiency;
- vertical stabilizer size has been determined to give a suitable damping effect over the lateral-directional dutch-roll mode.

As already mentioned, mass properties have been considered within this model. To this end, specific entities and properties have been set within the analysis environment. The main elements that define the aircraft total mass are the structure and the avionics system. These two macro aspects will be covered hereafter.

Structural weight In order to estimate the weight due to structural elements, the material properties have been taken into account. Since the designed material for this project is PLA, its density has been considered equal to $1240 kg/m^3$ [24]. Considering that the structure is mainly composed of thin elements, such as aerodynamic or fuselage skins, this value has been used to determine the relative surface density, parametrized with the local thickness. Table 3.7 represents the mass properties considered for each structural main component.

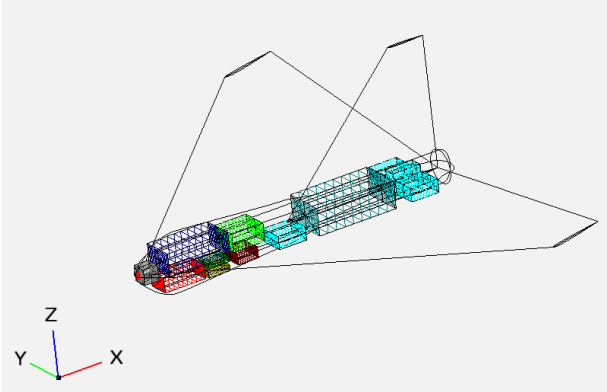

Figure 3.13: Avionic on-board mass

Element	**Thickness [mm]** [2]	**Surface density [kg/m^2]**
Fin	1.0	1240
Fuselage	1.5	1860
Wing	1.5	1860

Table 3.7: Structural mass properties

These are the structural mass properties values that will be considered for the whole design process.

Avionics weight To the end of correctly considering the weight, inertial properties and occupied space of the elements housed within the internal system bay, an ad-hoc model has been created for each component. For this reason, every device has been approximated with a parallelepiped which dimensions are those of the envelope volume occupied by the respective element. Furthermore, proper mass properties have been assigned to each of those: the assigned density is so that if homogeneously spread over the interested volume, the resulting mass would be equal to that of the actual device. For this process data from data-sheets have been used. Table 3.8 is a synopsis of the just mentioned evaluations.

Element	**Mass [kg]**	**Width [m]**	**Length [m]**	**Height [m]**	**Density [kg/m^3]**
GNSS	0.010	0.013	0.020	0.040	961.538
Servo	0.10	0.0118	0.0227	0.0267	1398.237
Battery3S	0.062	0.031	0.060	0.021	1587.302
Battery4S	0.143	0.025	0.076	0.038	1980.609
FCC	0.010	0.026	0.031	0.0165	751.936
Airspeed	0.0035	0.020	0.020	0.010	875.00
ELRS	0.003	0.015	0.021	0.005	1904.762
Camera	0.002	0.014	0.014	0.014	728.863
VTX	0.005	0.015	0.021	0.005	3174.603

Table 3.8: Avionics mass properties

Downstream of these aspects, the complete model of the aircraft has been defined, putting every avionics representative element within the structure containing them. Figure 3.13 represents a first attempt allocation of these devices. The driver aspects with respect to which the distribution of mass is optimized are the following:

- maintain the aircraft symmetry, both from a geometric standpoint and from a mass distribution one;
- ensure a positive static margin and, as a consequence, static longitudinal stability.

As it is possible to deduce, avionics devices are key elements to control the C.G. position of the aircraft: their relative positions constitute multiple degrees of freedom and allow for a precise study of the optimal configuration. Nevertheless, it may result that to obtain certain characteristics there may be no suitable

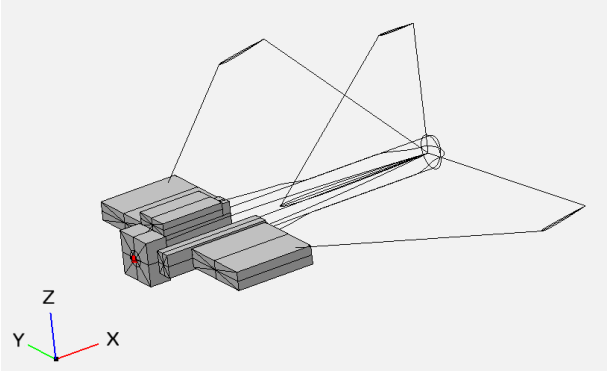

Figure 3.14: Ballast mass

on-board arrangement (e.g. a particular configuration may interfere with aircraft structure or aerodynamic features); for this reason, the presence of ballasts has been evaluated. In this regard, ballasts are considered as portions of the structure in which a solid material infill is present. This simple strategy makes it possible to fine tune the C.G. position without interfering with aircraft overall shape or requiring substantial modifications.
During the study of this first scaled model, some iterations have been conducted to determine the most suitable C.G. position. This lead to the presence of ballasts as in Figure 3.14.
The analysis of so defined model lead to the definition of features exposed in Table 3.9.

C.G. position	$x_G = 0.127$ m
Neutral point position	$x_N = 0.179$ m
Reference chord (MAC)	0.202 m
Reference surface	0.086 m^2
Altitude	0 m (sea level)
Mass	0.905 kg

Table 3.9: Scaled model features

Running analysis for the equilibrium condition, results shown in Table 3.10 are obtained.

Flight path angle	$\gamma = -5.68°$
AoA	$\alpha = 7.43°$
Speed	$V_{eq} = 24.32\ m/s$

Table 3.10: Scaled model - equilibrium conditions

As it is possible to notice, a significant decrease of the flight path angle has been obtained. Despite this, a significant increase in flight speed and AoA can be observed: one of the objectives of the following studies will be that of reducing the values of these two parameters. This is of relevance to give the aircraft a sufficiently wide range around the equilibrium condition.
At last the root loci for this configuration is shown in Figure 3.15.

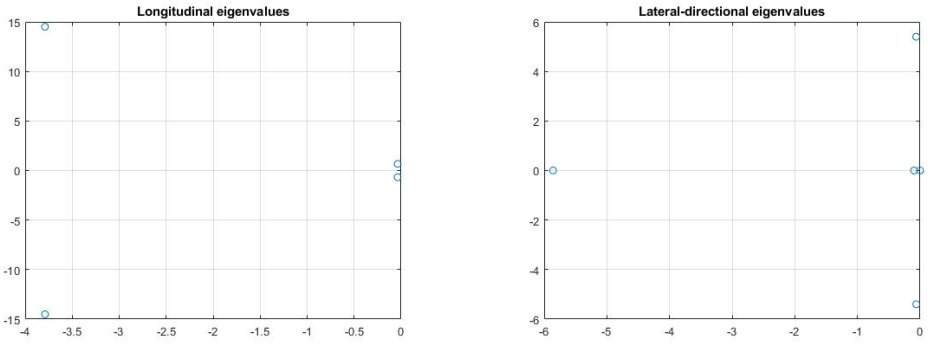

(a) Longitudinal plane (b) Lateral-directional plane

Figure 3.15: Scaled configuration root loci

As these charts report, this configuration satisfies the requirements for stability both from a static and dynamic standpoint. This configuration will be considered as the basis upon which a parametric analysis will be carried out to obtain the best compromise solution that will be the main outcome of this project.

3.8 Parametric analysis

Once defined a completely-featured aircraft model, as done in the previous section, it is now time to study in more precise details the effect of each design parameter on the aircraft performance. To this end, a parametric analysis has been carried out. Each of the following paragraphs report the main results for each studied parameter. For each of those, a modal analysis has been performed and four reference conditions have been considered: both at a null value of the AoA and at the trim condition one; and both at sea level altitude (z = 0 m) and at nominal flight altitude (z = 20000 m). The root loci diagrams reported hereafter allow to determine the intrinsic dynamic stability features. Data reported in Tables 3.6, 3.9 and 3.10 are considered as the reference configuration around which the following analysis has been conducted.

3.8.1 C.G. position

The first analyzed parameter has been the C.G. position with respect to the aircraft nose. The parametric analysis reported the following results:

Longitudinal plane Along this first set of axis, the corresponding root locus is reported in Figure 3.16.

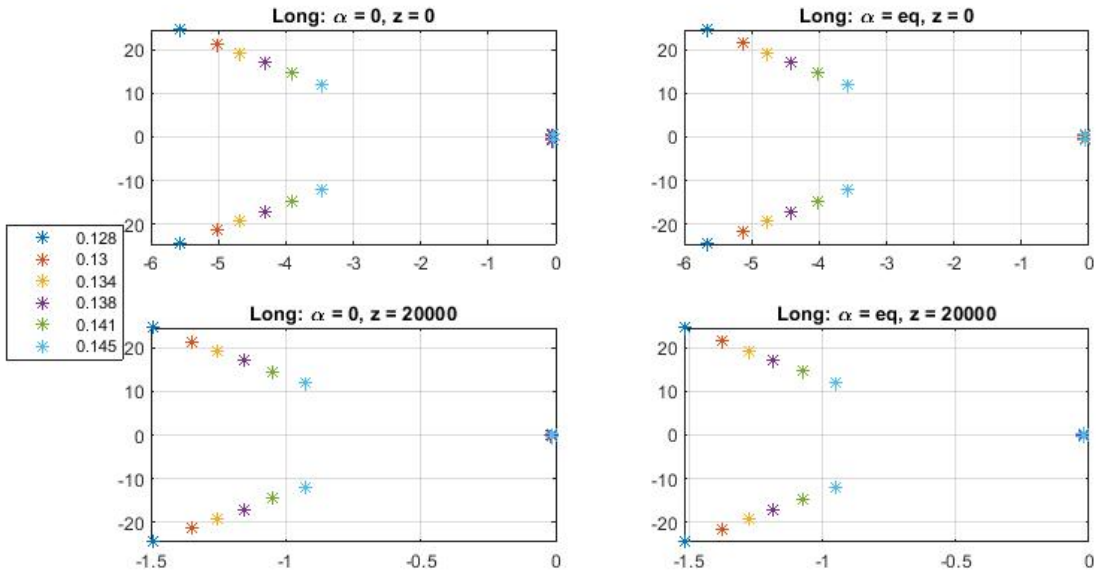

Figure 3.16: C.G. parametric analysis - longitudinal

As it is possible to notice, when moving the C.G towards the aircraft tail, the short period mode tends to lose it damping property while reducing its natural frequency. Similarly goes for the phugoid mode. This means that pushing the C.G. in an aft direction tends to reduce longitudinal stability.

Lateral-directional plane The root locus relative to the lateral-directional plane is presented in Figure 3.17.

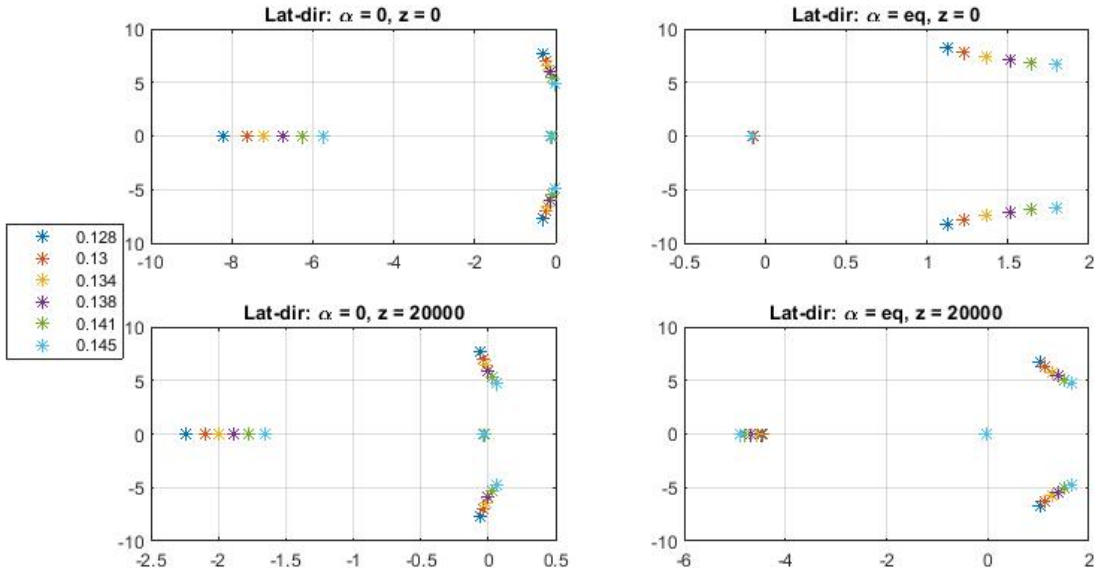

Figure 3.17: C.G. parametric analysis - lateral-directional

As these charts show, also on this plane the C.G. has a destabilizing effect on spiral and dutch-roll modes if moved towards the stern. In particular, beyond a certain threshold, the latter becomes unstable. In addition, effect are more evident in a high altitude environment: this is because lower air density leads to lower damping effects.

3.8.2 Dihedral angle

The study of this parameter is of particular interest for the effect is has over the lateral-directional plane, with particular regard to the dutch-roll mode. The results of analysis about this parameter are reported hereafter

Longitudinal plane Along this first set of axis, the corresponding root locus is reported in Figure 3.18.

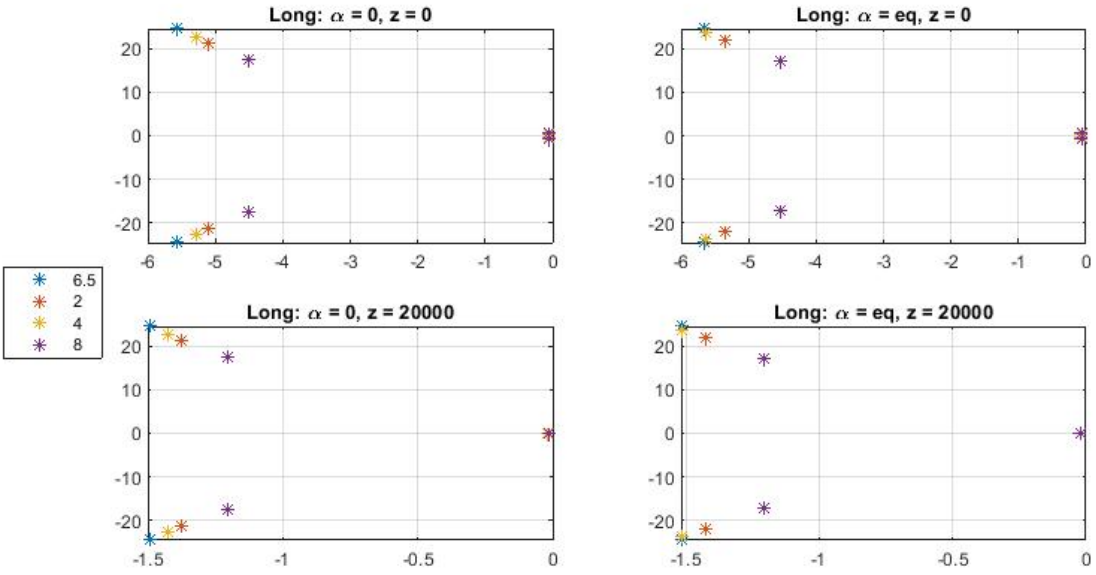

Figure 3.18: Dihedral angle parametric analysis - longitudinal

As it is possible to notice, with increasing values of the dihedral angle, the effect on the short period mode is the same as observed for the C.G. parameter. Nevertheless, the effect on the phugoid dynamic is negligible.

Lateral-directional plane The root locus relative to the lateral-directional plane is presented in Figure 3.19.

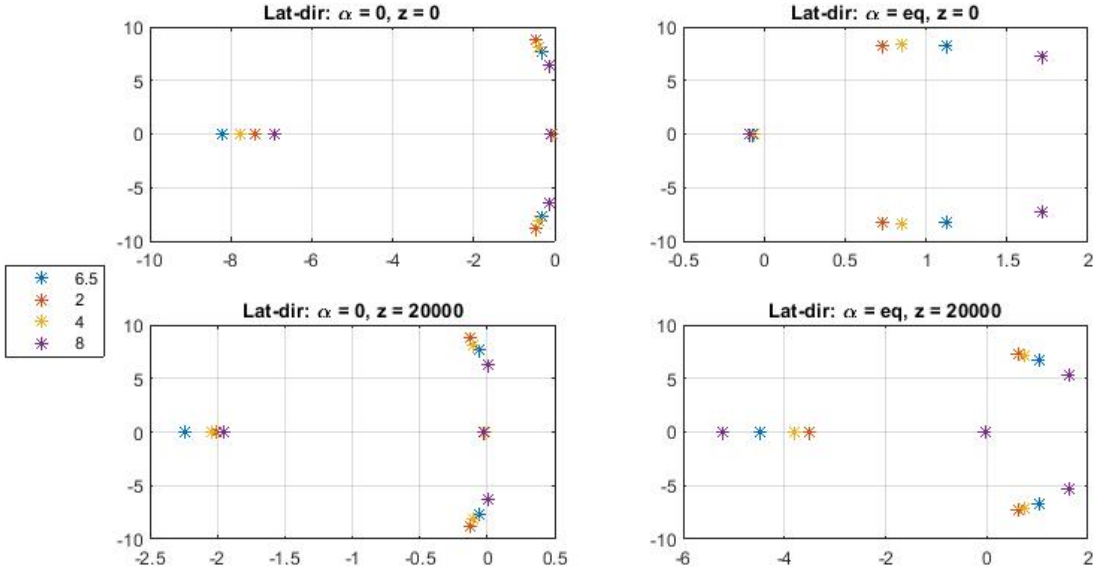

Figure 3.19: Dihedral angle parametric analysis - lateral-directional

As it can be seen, the main effect is on the dutch-roll mode and greater values for this parameter mean a less stable response. For this reason, also negative values for the dihedral angle may be considered. Conversely, it has a stabilizing effect on the spiral mode.

3.8.3 Sweep angle

As this analysis will show, increasing values of this parameter lead to a positive effect on dynamic stability. In particular:

Longitudinal plane Along this first set of axis, the corresponding root locus is reported in Figure 3.20.

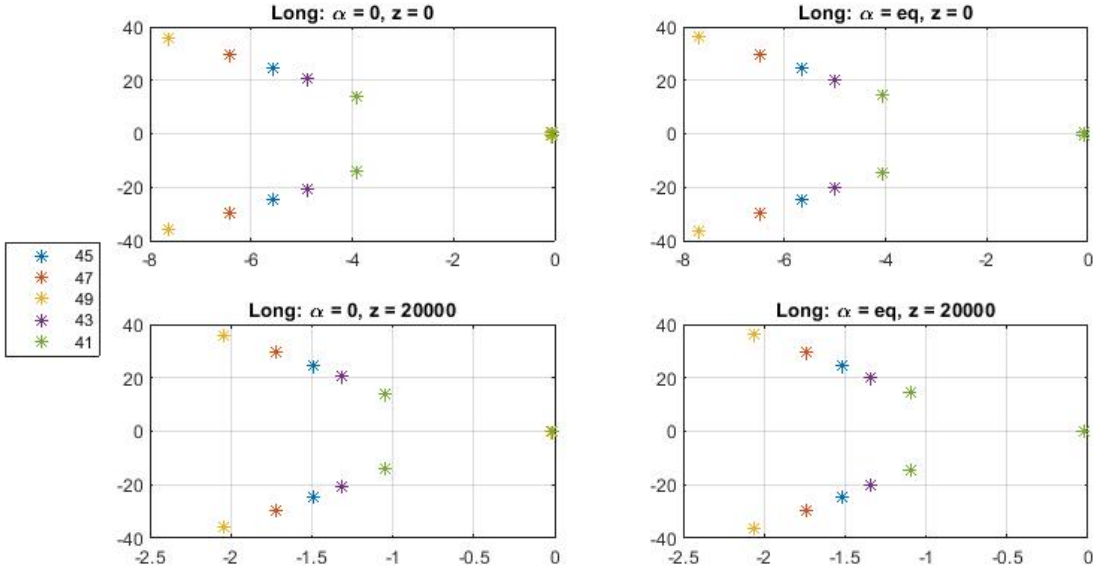

Figure 3.20: Sweep angle parametric analysis - longitudinal

As it is possible to notice, an evident stabilizing effect acts over the short period mode. This is because

increasing the sweep angle shifts the wing neutral point astern: this increases the static margin, hence improving longitudinal stability.

Lateral-directional plane The root locus relative to the lateral-directional plane is presented in Figure 3.21.

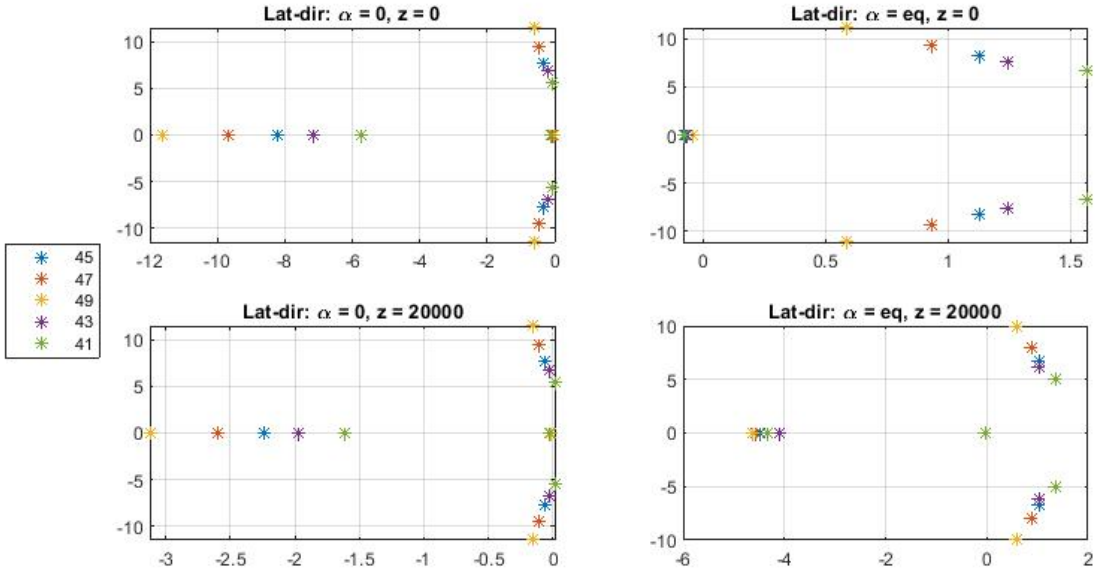

Figure 3.21: Sweep angle parametric analysis - lateral-directional

The main effect is on the roll mode, stabilizing it. Also a slight damping effect increase can be seen on the dutch-roll mode, despite a higher natuarl frequency.

3.8.4 Outcomes

The just mentioned parametric analysis has been useful to identify the effect that the variation of each parameter has on each dynamic property of the aircraft. Downstream of this study, an iterative study and optimization of the configuration has been conducted. At each step the static and dynamic properties of the model have been evaluated in order to fine tune the aforementioned parameters. This process eventually lead to the final configuration that will be described in the following section.

3.9 The final configuration

The major outcome of this preliminary aerodynamic design is that of obtaining an optimized aerodynamic configuration that satisfies the requirements for static and dynamic stability both along the longitudinal plane and the lateral-directional one. This will constitute the basis upon which the control surfaces will be designed and, at last, the experimental model will be manufactured. Table 3.11 shows the geometric features of this configuration

Wing	
Wingspan	$b = 0.688\ m$
Root chord	$c_{root} = 0.297\ m$
Tip chord	$c_{tip} = 0.021\ m$
LE sweep	$\Lambda_{LE} = 45.44°$
TE sweep	$\Lambda_{TE} = 12°$
Dihedral	$\Gamma = -9°$
Twist	$\Theta = -10°$
Airfoil	NACA 2207
Vertical stabilizer	
Height	$z_V = 0.07\ m$
Root chord	$c_{Vroot} = 0.17\ m$
Tip chord	$c_{tVip} = 0.06\ m$
LE sweep	$\Lambda_{V-LE} = 57.53°$
TE sweep	$\Lambda_{V-TE} = 0°$
Airfoil	NACA 0007
Fuselage	
Length	$0.30\ m$
Max width	$0.075\ m$
Max height	$0.05\ m$

Table 3.11: Final model geometry features

Picture in Figure 3.22 shows a perspective view of this configuration.

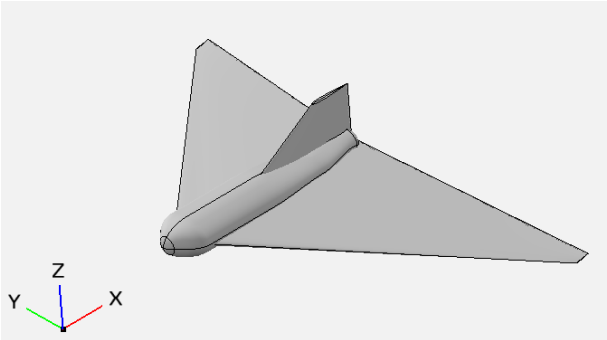

Figure 3.22: Final configuration - perspective view

Furthermore, the already mentioned mass properties have been set to this model. In particular, Picture 3.23 shows the on-board devices positioning, while Table 3.12 specifies the center of gravity position of each element with respect to the nose-fixed reference frame.

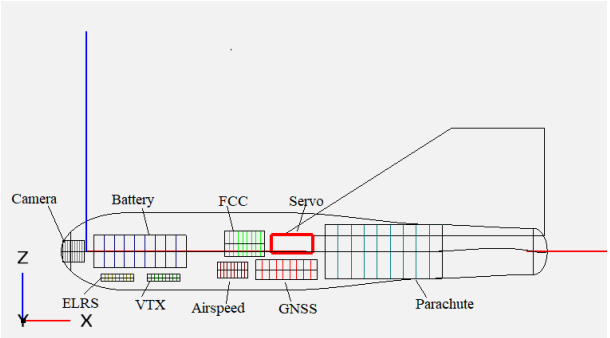

Figure 3.23: Final configuration - avionics disposition

Element	x [m]	y [m]	z [m]
GNSS	0.110	0.000	-0.012
Battery3S	0.005	0.000	0.000
Battery4S	0.005	0.000	0.000
FCC	0.09	0.000	0.005
Airspeed	0.085	0.000	-0.012
ELRS	0.010	0.000	-0.017
VTX	0.040	0.000	-0.017
Camera	-0.015	0.000	0.000
Parachute	0.155	0.000	0.000
Servo1	0.245	0.020	0.000
Servo2	0.245	-0.020	0.000
Servo3	0.245	0.000	0.000
Servo4	0.120	0.000	0.005

Table 3.12: Avionics mass properties

In addition to this, some ballast entities have been also introduced to correct the vehicle total mass distribution. Table 3.13 showcases the inserted ballasts specifications. In particular, for each of those, the dimensions (along x, y, z), the assigned density, and the C.G. position w.r.t. the nose-fixed frame are specified.

Element	**Size [m]**	**Density [kg/m^3]**	x [m]	y [m]	z [m]
Ballast1	(0.110x0.015x0.021)	1024	0.000	0.028	0.000
Ballast2	(0.110x0.015x0.021)	1024	0.000	-0.028	0.000
Ballast3	(0.075x0.070x0.017)	1240	0.025	0.070	0.000
Ballast4	(0.075x0.070x0.017)	1024	0.025	-0.070	0.000
Ballast5	(0.020x0.040x0.040)	1024	-0.010	0.000	0.000
Ballast6	(0.110x0.050x0.010)	1024	0.010	0.000	0.020
Ballast7	(0.110x0.050x0.010)	1024	0.010	0.000	-0.020

Table 3.13: Ballasts properties

Similarly to what done before, the main feature for this model have been evaluated and are presented in Table 3.14.

C.G. position	$x_G = 0.141$ m
Neutral point position	$x_N = 0.191$ m
Reference chord (MAC)	0.198 m
Reference surface	0.109 m^2
Altitude	0 m (sea level)
Mass	1.032 kg

Table 3.14: Final model features

The associated trim conditions, are presented in Table 3.15. This flight attitude and speed are calculated at sea level conditions. Table 3.16 reports the same values evaluated at altitude $z = 20000m$. As it is possible to notice, the flight path angle and the AoA don't change: only the flight speed increases to compensate the lower air density in stratosphere than in troposphere. This means that the Mach number in this condition is also higher than in troposphere flight. In this case, it slightly overshoots (M = 0.36) the imposed requirement: further analysis in the following chapters will be aimed to reduce this parameter value.

Flight path angle	$\gamma = -4.92°$
AoA	$\alpha = 5.78°$
Speed	$V_{eq} = 28.57\ m/s$

Table 3.15: Final configuration - equilibrium conditions (z = 0 m)

Flight path angle	$\gamma = -4.92°$
AoA	$\alpha = 5.78°$
Speed	$V_{eq} = 106.57\ m/s$

Table 3.16: Final configuration - equilibrium conditions (z = 20000 m)

Further aircraft performance data is reported in Table 3.17. The reported values are intended as steady-state equilibrium values.

Max. efficiency	$E_{max} = 14.27$
Max. efficiency AoA	$\alpha_{E_{max}} = 9°$
Min. flight path angle	$\gamma_{min} = 4°$
Min. descent speed speed @ 0 m	$w_{min} = 1.23\ m/s$
Min. descent speed speed @ 20000 m	$w_{min} = 4.65\ m/s$
Min. w AoA	$\alpha_{E_{max}} = 15°$

Table 3.17: Final configuration - performances

Figure 3.24 reports the polar curves.

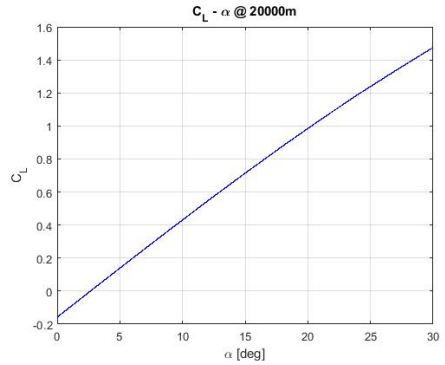

(a) Lift coefficient

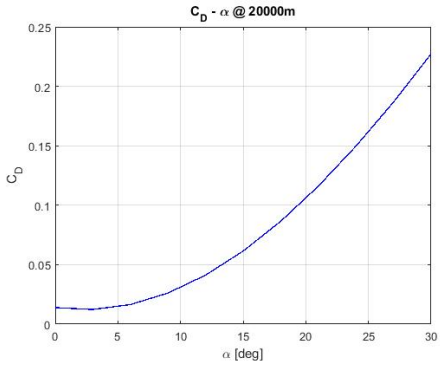

(b) Drag coefficient

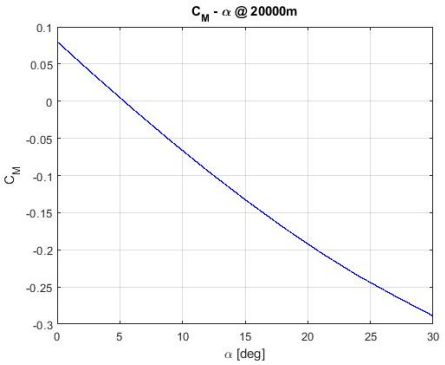

(c) Pitching moment coefficient

(d) Efficiency

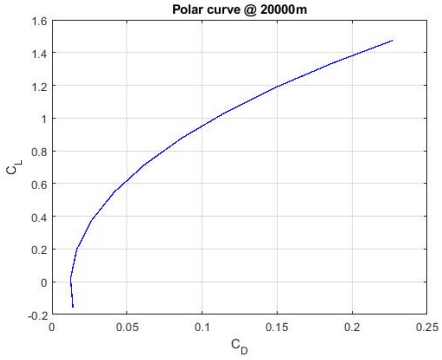

(e) Polar

Figure 3.24: Final configuration polar curves

At last, the dynamic modal analysis has been performed. As it is possible to see in Figure 4.10, every perturbation response mode is intrinsically stable. This means that this design process successfully managed to create a sufficiently stable platform that, after being subjected to a small perturbation, naturally returns to the original equilibrium state. More into details, the dynamics oscillatory modes are characterized by the following quantities:

- **short period**: period $T = 0.223\ s$, half-time $t/2 = 0.1\ s$, angular frequency $\omega = 28.93\ rad/s$, damping ratio $\zeta = 0.237$;
- **phugoid**: period $T = 13.46\ s$, half-time $t/2 = 12.76\ s$, angular frequency $\omega = 0.47\ rad/s$, damping ratio $\zeta = 0.115$;
- **dutch-roll**: period $T = 1.098\ s$, half-time $t/2 = 0.76\ s$, angular frequency $\omega = 5.79\ rad/s$, damping ratio $\zeta = 0.157$.

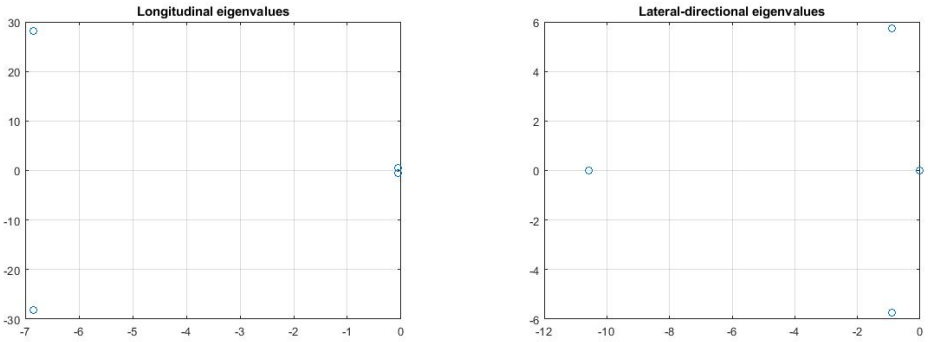

(a) Longitudinal plane (b) Lateral-directional plane

Figure 3.25: Final configuration root loci

Chapter 4

Control surfaces design

4.1 Control surfaces modeling

After having obtained an overall aircraft design from an aerodynamic standpoint, the following step is that of defining the number and type of control surfaces. As a preliminary assumption, the number of moving surface has been set to three: a rudder and a pair of elevons. This choice constitutes a conventional configuration for a delta wing aircraft. In this discussion, elevons may be also, improperly, referred to as ailerons or elevators to describe respectively their functionalities as control over the lateral-directional or longitudinal plane. In this context, the deflection angle of each surface, is referred to with the following variables. The respective sign is coherent with the body-fixed reference frame:

- δ_r: rudder deflection;
- δ_a: elevons deflection, when acting over lateral-directional plane;
- δ_e: elevons deflection, when acting over longitudinal plane.

Obviously, it is possible to express the control aerodynamic derivatives in analogy to what explained in the previous chapter. At this point it is possible model the control surfaces behavior adopting the same linearized model used for the overall aerodynamic evaluations. Similarly to what done before, the discussion will be carried out considering a separate study for the longitudinal and lateral-directional mechanics.

4.1.1 Longitudinal plane

The only control surfaces acting over the longitudinal plane are the elevons, when actuated in a symmetric way (δ_e). In this matter, their effect is that of changing the overall lift and pitching moment produced by the wing. For this reason, the most important aerodynamic derivatives associated to this control surface are:

- $C_{L\delta e}$;
- $C_{m\delta e}$.

In order to ensure conventional control inputs, the former should result greater than zero while the latter lower than zero. Thanks to the introduction of such control surfaces, it is now possible to evaluate the aircraft equilibrium condition with respect to the deflection of the elevons. To this end, it is possible to model the aircraft steady-state equilibrium condition with the following set of equations:

$$\begin{cases} C_{L,eq} = C_{L\alpha}\,\alpha_{eq} + C_{L\delta}\,\delta_{e,eq} \\ C_{m,eq} = 0 = C_{m0} + C_{m\alpha}\,\alpha_{eq} + C_{m\delta}\,\delta_{e,eq} \end{cases} \tag{4.1}$$

where $\Delta = C_{L\alpha}C_{m\delta} - C_{L\delta}C_{m\alpha}$ and is not afected by C.G. position. These equation are written at the equilibrium conditions, as such, all the mentioned variables have to be considered as the expected values

at the steady state regime. Solving Equations 4.1, it is possible to obtain the following expressions for the equilibrium AoA and elevon deflection angle:

$$\alpha_{eq} = C_{L,eq} \frac{C_{m\delta}}{\Delta} + C_{m0} \frac{C_{L\delta}}{\Delta} \tag{4.2}$$

$$\delta_{e,eq} = -C_{L\alpha} \frac{C_{m0}}{\Delta} - C_{L,eq} \frac{C_{m\alpha}}{\Delta} \tag{4.3}$$

From Equation 4.3 it is possible to derive the plot presented in Figure 4.1 [3]. The reported curves show the elevon deflection needed to equilibrate the aircraft at a certain lift coefficient. A negative slope indicates that with increasing lift coefficient, the demanded deflection becomes lower (i.e. upward elevon orientation): this corresponds with the conventional control mechanisms. Conversely, the opposite happens if considering curves with a positive slope. As it is possible to notice from the labels reported over the curves, the former condition coincides with that of longitudinal static stability; the latter, on the other hand, corresponds to an unstable configuration. The red-marked areas identify the elevons excursion limit. This poses a constraint on the maximum forward C.G. position. In fact, elevons size and C.G. position must be carefully evaluated in order to make it possible for the aircraft to be stabilized between the green lift coefficient thresholds with proper elevons excursion.

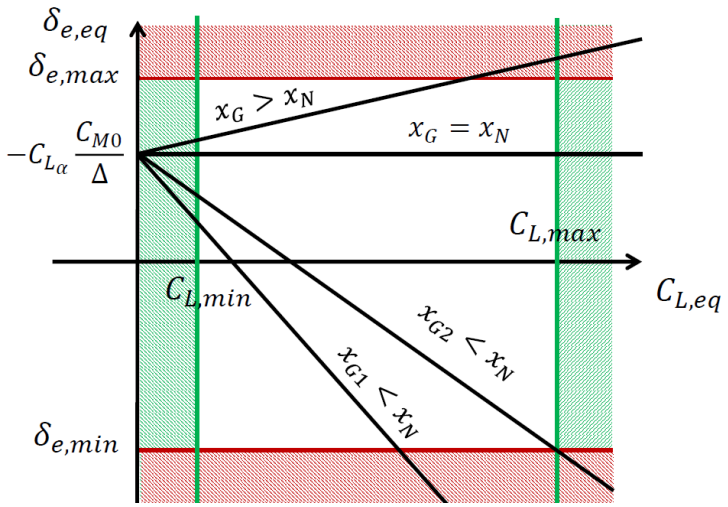

Figure 4.1: Longitudinal elevons deflection cases

Substituting Equation 4.2 into 4.3 and expressing $\delta_{e,eq}(\alpha_{eq})$, the following equation results:

$$\delta_{e,eq} = -\frac{C_{L\alpha}C_{m0}}{\Delta} - \frac{C_{m\alpha}}{C_{m\delta}}\alpha_{eq} + \frac{C_{m\alpha}C_{m0}C_{L\delta}}{C_{m\delta}\,\Delta} \tag{4.4}$$

This formula will be used to evaluate the needed elevon deflection to stabilized the aircraft at a certain AoA.
In addition, if substituting the lift coefficient definition in Equation 4.4, it is possible to obtain the following relation, that describes the demanded elevons angle with respect to the desired flight speed:

$$\delta_{e,eq} = -C_{L_\alpha}\frac{C_{m_0}}{\Delta} - \frac{C_{m_\alpha}}{\Delta}\frac{2W/S}{\rho V_{eq}^2} \tag{4.5}$$

Thanks to Equation 4.5 it is possible to verify the satisfaction of the speed-stability requirement, that can be expressed as:

$$\frac{\partial \delta_{e,eq}}{\partial V_{eq}} > 0$$

and is an implicit consequence of the static stability requirement.
In addition to this steady-state considerations, an insight on the dynamic modeling of the effects the control surfaces have on aircraft response is presented hereafter. Similarly to what done in the previous

chapter, the linearized approach of the state-space representation is adopted. Equation 3.15 can be extended as follows:

$$\{\dot{x}\} = A_{long}\{x\} + B_{long}\{\delta_e\} \tag{4.6}$$

where:

$$B_{long} = \begin{bmatrix} -\frac{C_{D\delta}}{2\mu} \\ -\frac{C_{L\delta}}{2\mu + C_{L_\alpha}} \\ \frac{C_{m\delta}}{\hat{J}_y} \\ 0 \end{bmatrix} \tag{4.7}$$

Thanks to this contribution, the dynamic model is complete and can accurately describe the time evolution of the aircraft motion in response of a command on the longitudinal plane.

4.1.2 Lateral-directional plane

Similarly to what discussed about the longitudinal plane, the same elements will be presented regarding the lateral-directional plane. In this case, the interested moving surfaces are both the rudder (δ_r) and the pair of elevons (δ_a). Also in this case it is possible to consider the following aerodynamic derivatives that express the corresponding effects:

- $C_{l\delta a}$: aileron effectiveness;
- $C_{n\delta r}$: rudder effectiveness;
- $C_{n\delta a}$: aileron adverse yaw;
- $C_{l\delta r}$: rudder induced roll.

One key difference between the type of controls acting on the longitudinal plane or the lateral-directional one worth mentioning is that the former acts as *attitude* commands while the latter as *rate* commands. As such, to the aim of correctly sizing the control surfaces, two evaluations will be conducted in steady-state regime: roll angular speed and sideslip angle counteraction.
To analyze the former scenario, it is sufficient to perform an equilibrium analysis of the roll moment (l) produced by the elevons deflection ($C_{l\delta a}\delta_a$) and the damping effect caused by angular regime roll speed ($C_{lp}\hat{p_{reg}}$). From this simple equilibrium condition, it is possible to state that the non-dimensional roll speed is correlated to the aileron displacement by the relation that follows:

$$\hat{p_{reg}} = -\frac{C_{l\delta a}}{C_{lp}}\delta_a \tag{4.8}$$

Conversely, in order to evaluate the rudder and ailerons deflections needed to counteract a certain sideslip angle β, an equilibrium condition is imposed over the yaw and roll axis. Steady-state conditions are considered and the following relation holds: $p = r = \dot{\beta} = 0\ rad/S$. It is then possible to write the following set of equations through which it si possible to obtain δ_a and δ_r in the face of an imposed β angle.

$$\begin{cases} C_{l_\beta}\beta + C_{l_{\delta_a}}\delta_a + C_{l_{\delta_r}}\delta_r = 0 \\ C_{n_\beta}\beta + C_{n_{\delta_a}}\delta_a + C_{n_{\delta_r}}\delta_r = 0 \end{cases} \tag{4.9}$$

At last, also on the lateral-directional plane it is possible to integrate the control surfaces effect in the state-space dynamics equation. The complete model, in fact can be represented as:

$$\{\dot{x}\} = A_{lat-dir}\{x\} + B_{lat-dir}\begin{Bmatrix} \delta_a \\ \delta_r \end{Bmatrix} \tag{4.10}$$

where:

$$B_{lat-dir} = \begin{bmatrix} \frac{C_{Y_{\delta_a}}}{2\mu} & \frac{C_{Y_{\delta_r}}}{2\mu} \\ \left(\frac{C_{l_{\delta_a}}}{\hat{J}'_x} + \hat{J}'_{xz}C_{n_{\delta_a}}\right) & \left(\frac{C_{l_{\delta_r}}}{\hat{J}'_x} + \hat{J}'_{xz}C_{n_{\delta_r}}\right) \\ \left(\frac{C_{n_{\delta_a}}}{\hat{J}'_z} + \hat{J}'_{xz}C_{l_{\delta_a}}\right) & \left(\frac{C_{n_{\delta_r}}}{\hat{J}'_z} + \hat{J}'_{xz}C_{l_{\delta_r}}\right) \\ 0 & 0 \\ 0 & 0 \end{bmatrix} \tag{4.11}$$

This completes the dynamic model definition and makes it possible to evaluate the dynamic evolution of the aircraft mechanics in response to a generic command.

4.2 Control surfaces preliminary design

Downstream of these considerations, a first attempt sizing of the movable surfaces is presented hereafter. In particular, some details regarding the elevators are provided in the following list:

- extension in the spanwise direction: from 20% to 90% of the half-span;
- extension in the chord direction: 30% of the local chord for each point of the movable surface.

A visual representation of this configuration is presented in Figure 4.2.

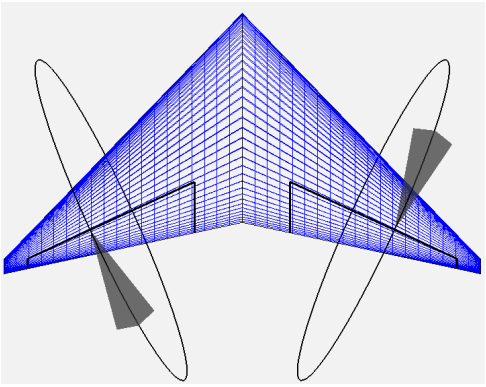

Figure 4.2: First attempt elevons configuration

Regarding the rudder, instead, the chosen dimensions are:

- Extension in the height direction: from 20% to 80% of the tail height;
- Extension in the chord direction: 0.037 m.

Figure 4.3 depicts this configuration.

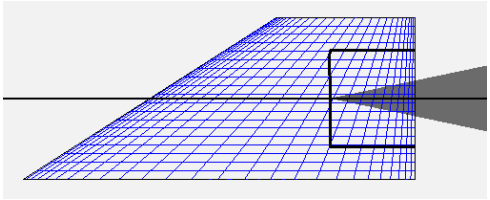

Figure 4.3: First attempt rudder configuration

On this basis, the OpenVSP analysis has been run and, as a first result, it is possible to notice the values for the control aerodynamic derivatives, as it can be seen in Table 4.1.

$C_{m\delta}$	-0.7617
$C_{l\delta a}$	-0.0048
$C_{n\delta a}$	0.000621

Table 4.1: First attempt control derivatives

Regarding the control authority over the pitch axis, plots in Figure 4.4 report the elevator deflection needed to stabilize the aircraft at a specific AoA or flight speed. Red horizontal lines indicate the maximum assumed elevon excursion in order to avoid stalling.

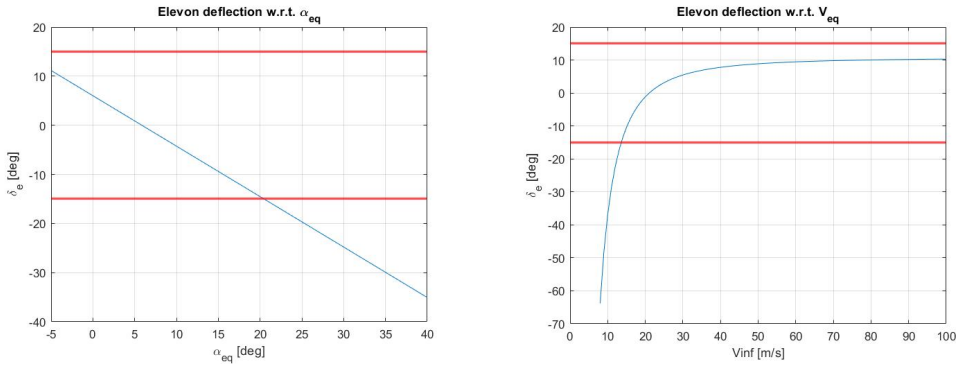

(a) Elevon deflection w.r.t. AoA (b) Elevon deflection w.r.t. trim speed

Figure 4.4: Elevon deflection - first attempt

Considering the control authority over the roll axis, instead, plot in Figure 4.5 is representative of the regime roll speed with respect to the imposed elevon deflection.

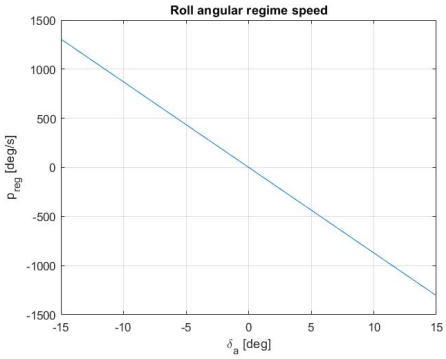

Figure 4.5: Elevon deflection w.r.t. roll rate

At last, Table 4.2 shows the needed elevons and rudder deflections required to counteract the specified β values.

β	δ_a	δ_r
10°	1.26°	28.23°
15°	1.89°	42.34°
20°	2.52°	56.46°

Table 4.2: Sideslip angle counteracion - first attempt

As it is possible to notice, this configuration gives good controllability properties on the longitudinal plane even if an extension of the α_{eq} range will be object of study. On the lateral directional one, despite having a very intense authority over the roll axis, the rudder is under-dimensioned: this is indicated by the very wide deflection required to counteract the sideslip angle.
Downstream of these considerations, to further improve the effect of the elevon over the longitudinal axis, $C_{m\alpha}$ derivative absolute value has to be reduced. Similarly rudder effectiveness must be improved.

4.3 Final complete design

After performing the aforementioned evaluations the following changes have been made:

- **aft shift of the center of gravity**: in order to decrease the aerodynamic derivative $C_{m\alpha}$ value, the distance between the center of gravity and the neutral point was reduced. To this end, the center of gravity was moved aft by reducing the amount of ballast placed in forward part of the

model. In this way, the beneficial effect of reducing the overall mass and, consequently, the trim velocity was also obtained;

- **forward shift of the aerodynamic center**: for the same purpose as the previous point, the position of the aerodynamic center was advanced by reducing the sweep angle of the trailing edge. This operation was carried out while keeping constant the wing root chord, the tip chord, and the wingspan; in this way, a corresponding reduction of the leading-edge sweep angle occurred;
- **variation of rudder relative chord extension**: in order to preserve the control authority of this movable surface while increasing the structural strength of the vertical tailplane, both the root chord and the tip chord of the vertical tail were increased. At first, an attempt was made to keep the shape of the vertical tail unchanged by acting only on the dimensions of the movable surface: the tip chord of the rudder was reduced and the root chord increased. However, this modification negatively affected the control authority of the movable surface, requiring larger deflections to balance the aircraft in the presence of crosswind. This effect was attributed to the variation of the hinge axis inclination of the rudder: this could have caused the force component generated by the rudder to be inclined at a nonzero angle with respect to the XY plane, leading to a reduction of the effective component capable of generating yawing moment (absolute reduction of the derivative $C_{n\beta}$). Therefore, it was decided to restore the size of the movable surface and to increase the chord extension of the vertical tailplane by acting on both root and tip chords. Thanks to this modification, the rudder authority was effectively increased and the tip chord-to-root chord ratio c_{tip}/c_{root} was reduced.

A synopsis of the glider final configuration is presented hereafter. Starting from the main geometrical features, Table 4.3 showcases the final version specifications.

Wing	
Wingspan	$b = 0.688\ m$
Root chord	$c_{root} = 0.297\ m$
Tip chord	$c_{tip} = 0.021\ m$
LE sweep	$\Lambda_{LE} = 44.4°$
TE sweep	$\Lambda_{TE} = 10°$
Dihedral	$\Gamma = -6°$
Twist	$\Theta = -6°$
Airfoil	NACA 1207
Vertical stabilizer	
Height	$z_V = 0.09\ m$
Root chord	$c_{Vroot} = 0.20\ m$
Tip chord	$c_{tVip} = 0.10\ m$
LE sweep	$\Lambda_{V-LE} = 48.0°$
TE sweep	$\Lambda_{V-TE} = 0°$
Airfoil	NACA 0007
Fuselage	
Length	$0.30\ m$
Max width	$0.075\ m$
Max height	$0.05\ m$

Table 4.3: Final model geometry features - controls

After this, Table 4.4 contains the main geometrical features regarding the control surfaces.

Rudder	
Height	from 10% to 100% of vertical stabilized height
Root chord	$c_{root} = 0.07\ m$
Tip chord	$c_{tip} = 0.07\ m$
Elevons	
Spanwise dimension	from 10% to 80% of half-wing aperture
Root chord	$c_{Vroot} = 0.08\ m$
Tip chord	$c_{tVip} = 0.04\ m$

Table 4.4: Control surfaces geometry features

Picture in Figure 4.6 are representative of the final aircraft configuration, as specified in Tables 4.3 and 4.4.

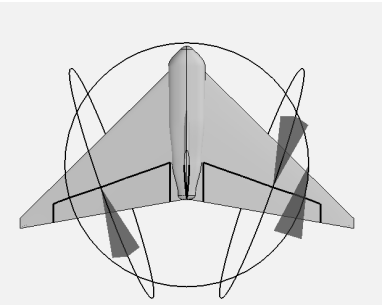

(a) Final model - top view

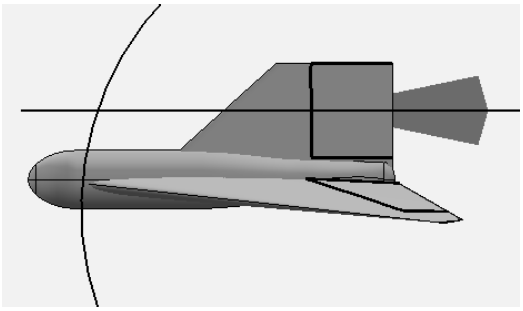

(b) Final model - left view

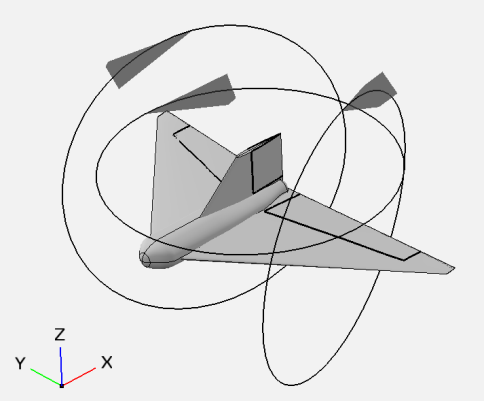

(c) Final model - perspective view

Figure 4.6: Final model views

Once completely defined the geometry features, it is time to specify the final configuration of the on-board equipment disposition. These data are reported in Table 4.5.

Element	x **[m]**	y **[m]**	z **[m]**
GNSS	0.110	0.000	-0.012
Battery3S	0.005	0.000	0.000
Battery4S	0.005	0.000	0.000
FCC	0.09	0.000	0.005
Airspeed	0.085	0.000	-0.012
ELRS	0.010	0.000	-0.017
VTX	0.040	0.000	-0.017
Camera	-0.015	0.000	0.000
Parachute	0.155	0.000	0.000
Servo1	0.245	0.020	0.000
Servo2	0.245	-0.020	0.000
Servo3	0.245	0.000	0.000
Servo4	0.120	0.000	0.005

Table 4.5: Final avionics mass properties

In order to complete the mass distribution description, Table 4.6 reports the ballasts geometrical and physical specifications.

Element	**Size [m]**	**Density [kg/m^3]**	x **[m]**	y **[m]**	z **[m]**
Ballast1	(0.110x0.015x0.021)	1024	0.000	0.028	0.000
Ballast2	(0.110x0.015x0.021)	1024	0.000	-0.028	0.000
Ballast3	(0.075x0.070x0.017)	620	0.025	0.070	0.000
Ballast4	(0.075x0.070x0.017)	620	0.025	-0.070	0.000
Ballast5	(0.020x0.040x0.040)	620	-0.010	0.000	0.000
Ballast6	(0.110x0.050x0.010)	620	0.010	0.000	0.020
Ballast7	(0.110x0.050x0.010)	620	0.010	0.000	-0.020

Table 4.6: Final ballasts properties

As it is possible to notice, some of the ballasts have been reduced in terms of assigned density: this allows the aircraft to be lighter and, thus, to reduce the overall flight airspeed. Considering the physical and mechanical characteristics just mentioned, it is possible deduce the salient features displayed in Table 4.7.

C.G. position	$x_G = 0.159$ m
Neutral point position	$x_N = 0.185$ m
Dimensional static margin	0.026 m
Static margin, referred to the (MAC)	$K_n = 0.126$
Reference chord (MAC)	0.198 m
Reference surface	0.109 m^2
Mass	0.849 kg

Table 4.7: Final model features

Downstream of these data, it is possible to evaluate the steady-state equilibrium conditions. As a reference, the case with null control surfaces deflection is considered. Results to this study are presented in 4.8. As it is possible to see, the flight speed has been calculated both for sea level and stratosphere altitude flight conditions. The latter corresponds to $M = 0.33$: this is slightly higher that the $M = 0.3$ threshold. Nevertheless, considering that the aircraft is equipped with suitable control surfaces, a lower equilibrium speed can be obtained. For this reason, this result is considered acceptable.

Flight path angle	$\gamma = -2.74°$
AoA	$\alpha = 4.57°$
Speed @ $z = 0\ m$	$V_{eq} = 26.04\ m/s$
Speed @ $z = 20000\ m$	$V_{eq} = 97.15\ m/s$

Table 4.8: Final configuration - equilibrium conditions - controls

Further aircraft performance data are reported in Table 4.9. The reported values are intended as steady-state equilibrium values.

Max. efficiency	$E_{max} = 16.17$
Max. efficiency AoA	$\alpha_{E_{max}} = 9°$
Min. flight path angle	$\gamma_{min} = 3.53°$
Min. descent speed speed @ 0 m	$w_{min} = 0.99\ m/s$
Min. descent speed speed @ 20000 m	$w_{min} = 3.664\ m/s$
Min. w AoA	$\alpha_{E_{max}} = 12°$

Table 4.9: Final configuration - performances

Thanks to the improvements made to the previous configurations, the maximum efficiency has increased and the minimum descend speed has decreased. These features are of particular interest for the mission this glider will be interested in. Higher efficiency and lower descent speed mean longer range and longer in-flight time: these are key characteristics to make the aircraft viable to be employed within an edutainment platform. Figure 4.7 reports the polar curves.

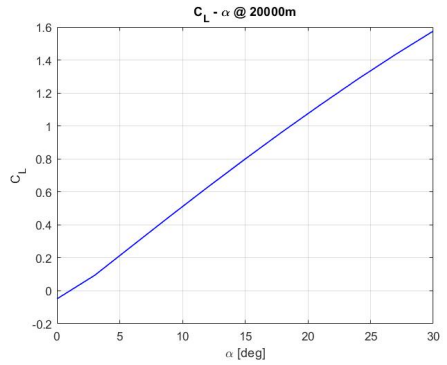

(a) Lift coefficient

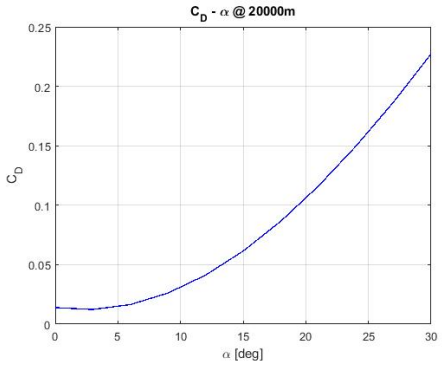

(b) Drag coefficient

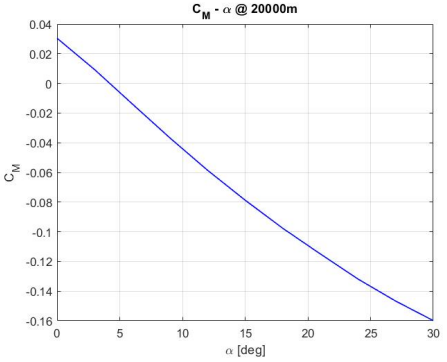

(c) Pitching moment coefficient

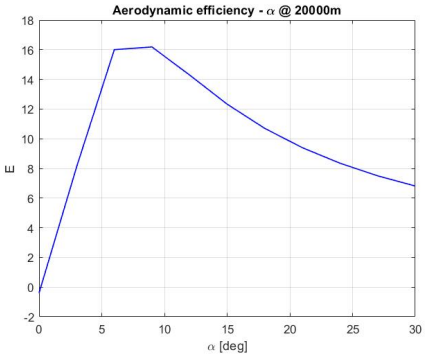

(d) Efficiency

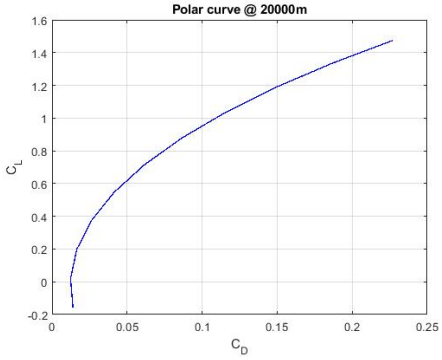

(e) Polar

Figure 4.7: Final configuration polar curves - controls

More specifically, the aerodynamic coefficients and derivatives shown in Table 4.10 have been evaluated.

Stability derivatives	
Longitudinal plane	
C_{m0}	0.0304
$C_{m\alpha}$	-0.3826
Lateral-directional plane	
$C_{l\beta}$	-0.0179
$C_{n\beta}$	0.0136
Control derivatives	
Longitudinal plane	
$C_{m\delta e}$	-0.6649
Lateral-directional plane	
$C_{l\delta a}$	-0.3052
$C_{l\delta r}$	-0.0011
$C_{n\delta a}$	0.0365
$C_{n\delta r}$	-0.0107

Table 4.10: Final aerodynamic derivatives

From these values it is possible to notice that the aircraft is statically stable along both longitudinal and lateral-directional plane. In addition, from the values of the control derivatives, it is possible to assess that the designed controls are coherent with the conventional configuration. In addition, the adverse yaw and induced roll effects are expected to be significantly small since the corresponding derivatives are smaller of more than an order of magnitude than the control ones.
Downstream of this, it possible to analyze the control surfaces effectiveness over the longitudinal plane using charts reported in Figure 4.8.

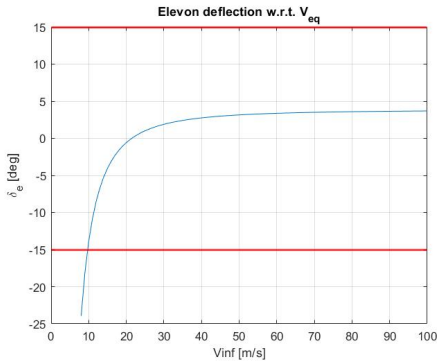

(a) Elevon deflection w.r.t. trim speed @ z = 0 m

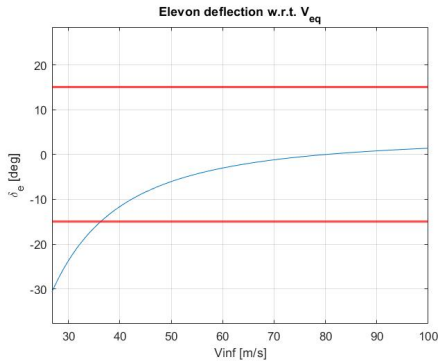

(b) Elevon deflection w.r.t. trim speed @ z = 20000 m

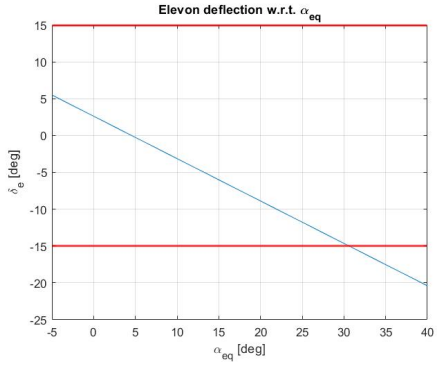

(c) Elevon deflection w.r.t. AoA

Figure 4.8: Elevon deflection - final configuration

Once again, it is possible to notice from these charts that the speed stability requirement is respected.

In addition, plot in figure 4.8b shows that airspeed as lower as roughly 35 m/s can be obtained within the nominal elevon excursion. This demonstrates that the $M < 0.3$ requirement is actually satisfied. In addition chart 4.8a shows that an minimum steady-state airspeed of 10 m/s can be obtained when flying at sea level altitude. Coming to the lateral-directional plane, Figure 4.9 shows the lateral control effectiveness of the elevons. Since the most critical condition for their sizing has been that of longitudinal attitude control, their still are over-sized with respect to the lateral aircraft inertia and damping.

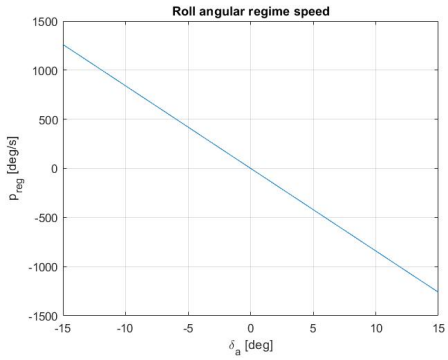

Figure 4.9: Roll speed at regime condition - final configuration

Nevertheless, the sizing fine-tuning design applied on the control surfaces relative to the lateral-directional plane led to suitable rudder excursion when counteracting a sideslip angle. This is shown in Table 4.11. The reported data show that the rudder control authority has actually been increased.

β	δ_a	δ_r
10°	0.54°	10.91°
15°	0.82°	16.37°
20°	1.09°	21.83°

Table 4.11: Sideslip angle counteraction - final configuration

At last, to conclude this overall view of the final aeromechanic model resulted as an outcome of this design project, the dynamic properties are presented. The following list shows the most relevant properties of the aircraft dynamic modes in response to a small perturbation:

- **short period**: period $T = 0.316\ s$, half-time $t/2 = 0.108\ s$, angular frequency $\omega = 20.87\ rad/s$, damping ratio $\zeta = 0.305$;
- **phugoid**: period $T = 12.36\ s$, half-time $t/2 = 11.92\ s$, angular frequency $\omega = 0.51\ rad/s$, damping ratio $\zeta = 0.1131$;
- **dutch-roll**: period $T = 1.578\ s$, half-time $t/2 = 1.175\ s$, angular frequency $\omega = 4.024\ rad/s$, damping ratio $\zeta = 0.145$.

As it is possible to notice, these last values are very similar to the ones relative to the configuration presented in the previous chapter. Nevertheless, the changes made slightly improved the short period dynamics features: this is a relevant result because it confers better controllability features to the aircraft. The same result is true also for the dutch-roll mode.
Eventually, as a synoptic view of the just mentioned aspects, the root loci are presented in Figure 4.10.

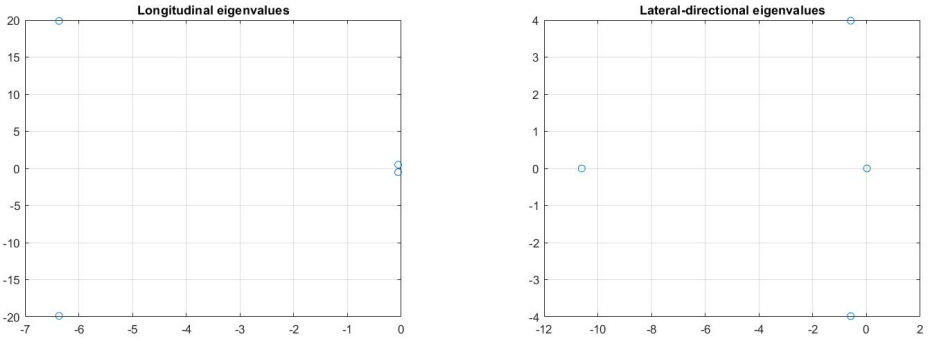

(a) Longitudinal plane (b) Lateral-directional plane

Figure 4.10: Final configuration root loci

Chapter 5

Prototype manufacturing

5.1 Structural modeling

The final outcome of the previous sections has been that of designing an aeromechanical model for a delta wing glider featured with suitable static and dynamic stability and controllability. At this stage a detailed 3D modeling process can be undertaken to the aim of making a set of elements that can be eventually employed to physically build the aircraft model. As a first step, a set of *primitive* elements has been created following the geometrical characteristics analyzed in the previous chapters: this refers to the modeling of the aircraft basic elements: the wing, the fuselage and the vertical stabilizer. These parts have been modeled as hollow objects, setting a wall thickness as specified in Table 3.7. After this, these components have been merged, respecting the mutual relative positioning and clearing the resulting object from intersecting parts. At this point, a complete 3D, hollow CAD model of the aircraft has been obtained. The following phases regarded the designing of the internal spaces aimed to accommodate the on-board electronics. After this, a detailed modeling of the control surfaces followed. At last, a study of the subdivision of the model for 3D printing has been conducted. The Following paragraphs report detailed information and descriptions of the structural modeling process. Every part of the hereby presented modeling phase has been conducted within the *SolidWorks* environment.

5.1.1 Primitives modeling

This preliminary design phase had the objective of creating the basic geometries needed to obtain a 3D model of the glider. First of all, a material library corresponding to the PLA used for manufacturing has been created. Table 5.1 [24] specifies the mechanical properties considered for this project. This defines the material called *PLA* that has been applied to every structural component of this project.

PLA	
Elastic modulus	3500 MPa
Poisson's ratio	0.36
Shear modulus	1287 MPa
Mass density	1240 kg/m^3
Tensile strength	59 MPa
Yield strength	70 MPa

Table 5.1: PLA mechanical properties

At this stage, the aircraft primitive components have been modeled according to sizes reported in Table 4.3.

The wing

This is the main entity of the aircraft. I has been obtained through a twisted extrusion of the NACA 1207 airfoil, show in Figure 5.1.

Figure 5.1: NACA 1207 airfoil

This operation has been performed assigning a wall thickness of 1.5 mm. The overall result is shown in Figure 5.2.

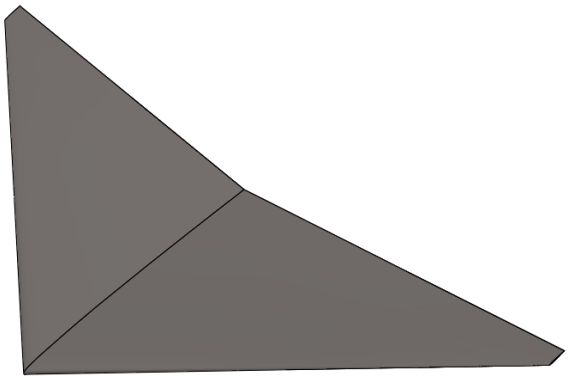

Figure 5.2: Wing primitive

Pictures in Figure 5.3 offer different views of the 3D model for this primitive. In particular, from Figure 5.3a is is possible to notice the presence of the negative dihedral angle; picture in Figure 5.3b shows the inner cavity and it is possible to see the entity of the set wall thickness. Eventually, Figure 5.3c shows the planform of the aerodynamic surface: from this view it is possible to notice the wing tapering together with leading edge and trailing edge sweep angles.

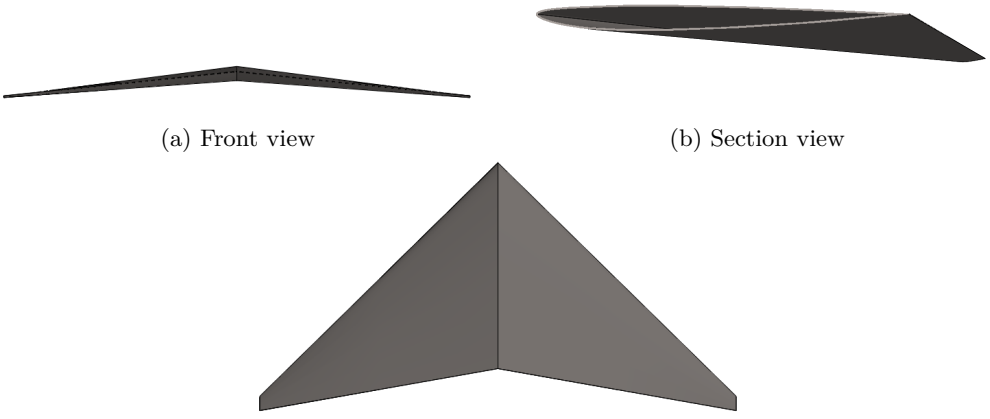

(a) Front view

(b) Section view

(c) Top view

Figure 5.3: Wing primitive views

In addition, it is worth to notice that the wingtips of this model aren't actually hollow but solid filled. This happens because the local total wing thickness is lower that the wall thickness.

The vertical stabilizer

The second basic element modeled has been the vertical stabilizer. Similarly to the wing, it has been obtained through an extrusion of the NACA 0007 airfoil and it is shown in Figure 5.4.

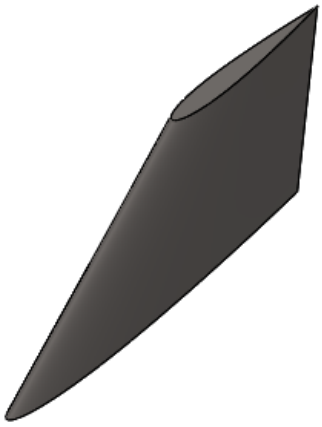

Figure 5.4: Fin primitive

Pictures in Figure 5.5 show different views of this aerodynamic surface. In particular, Figures 5.5a and 5.5b represent a top and a section view of the fin and from them it is possible to notice the actual shape of the adopted airfoil. Figure 5.5c, instead, shows a side view of this element, making visible the leading edge sweep angle.

(a) Top view

(b) Section view

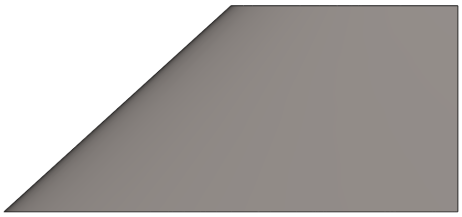

(c) Side view

Figure 5.5: Vertical stabilizer primitive views

The fuselage

The last primitive element modeled has been the fuselage. Due to its irregular shape, this entity has been directly exported from the OpenVSP environment and edited within SolidWorks to obtain a suitable hollow model. The result of these operations is shown in Figure 5.6.

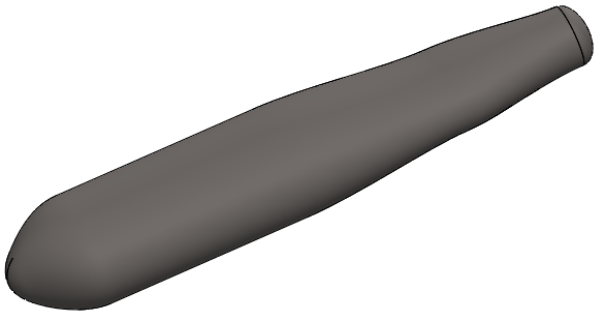

Figure 5.6: Fuselage primitive

Figures 5.7a and 5.7b show respectively a top and lateral section view of the fuselage, from which it is possible to notice the wall thickness associated to this component and the internal space to be used as the

main avionic bay for this aircraft.

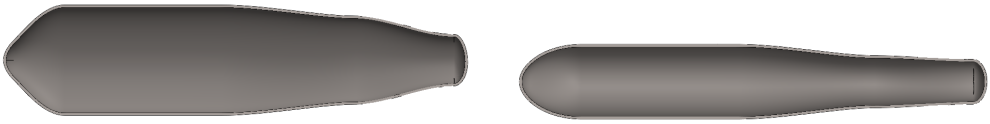

(a) Top view (b) Lateral view

Figure 5.7: Fuselage primitive views

The aircraft overall shell

Once obtained the three primitive elements just described, the following step has been that of merging them respecting their mutual relative positioning. Once cleaned the model from all the superfluous intersecting geometries, a hollow, reliable representation of the aircraft shell has been obtained.

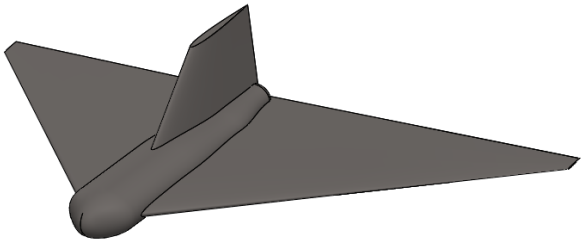

Figure 5.8: Overall shell

Pictures in Figure 5.11 show different views of this model.

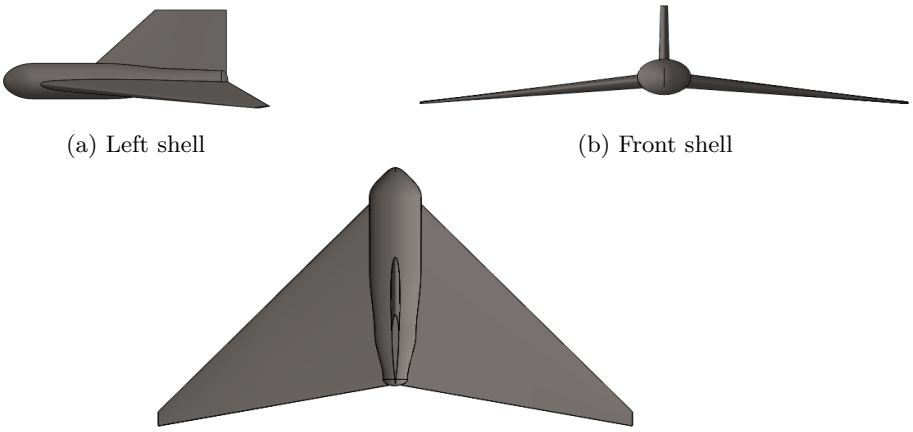

(a) Left shell (b) Front shell

(c) Top shell

Figure 5.9: Shell views

At last, Figure 5.10 reports a section view of the model, making visible the final result of this first stage of 3D modeling.

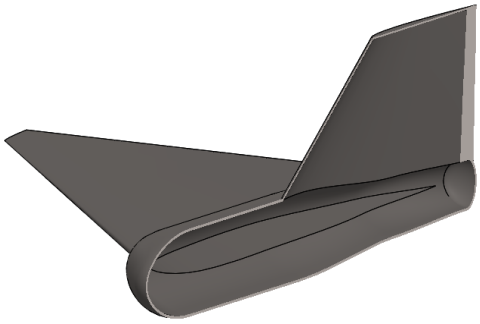

Figure 5.10: Shell section

5.1.2 Internal bay modeling

After having defined the overall shape of this aircraft model, the next phase regarded the design of the internal compartments aimed to house the various electronic components. These slots have been positioned within the aircraft structure according to the devices positioning expressed in Table 4.5.
As a first step, the aircraft waterline plane has been created, adding to the lower part of the fuselages a solid element, constituting *Ballast7* as specified in Table 4.6. On top of it the ELRX and VTX modules housings have been created, as shown in Figures 5.11a and 5.11b. For these elements, rectangular shaped inserts have been created and their size is determined to fit the respective devices with a tolerance of 1 mm.

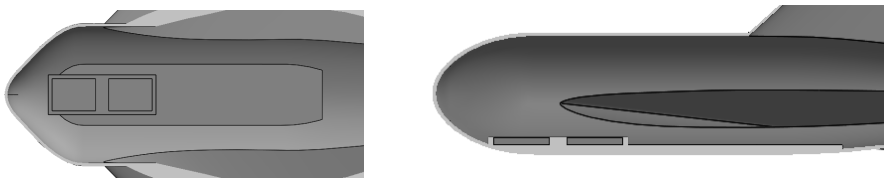

(a) Top view (b) Left view

Figure 5.11: ELRS and VTX housings

Similarly to this, housings for Airspeed and GNSS module have been created in the aft part of the waterline plane. Regarding the nose cone, instead, the most forward part of the fuselage has been filled with material - creating *Ballast5* - and the camera slot has been carved into it. Eventually, to the aim of sustaining the battery packs, symmetrical supports have been added above the ELRS and VTX housings. These features are represented in Figure 5.12.

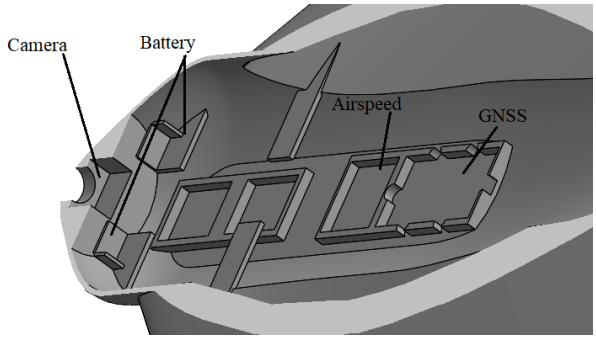

Figure 5.12: Avionic bay general view

At last, the support structure for the FCC is created on top of the Airspeed and GNSS housings. This is shown in Figure 5.13.

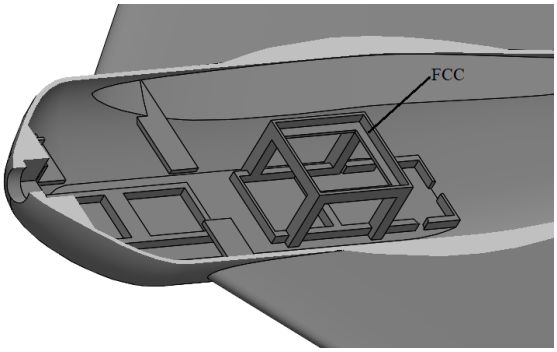

Figure 5.13: FCC holder

At this stage the housing for every on-board device has been correctly designed in order to fit all the internal components in the correct position determined in the previous design phases. This is fundamental to ensure the correct C.G. position.
In addition to this, the Pitot-tube holding structure and antennas openings have been created. Regarding the former, it has been chosen to insert it underneath the main fuselage body with the probe pointing forward. This structure has been positioned in the very forward part of the model so that the Pitot-tube total and static pressure holes would result out of the fuselage boundary layer. In addition, cavities to accommodate pressure lines have been carved within the aforementioned structure. Regarding the antennas openings, instead, these have been placed aside the ELRS and VTX bays. This is shown in Figure 5.14.

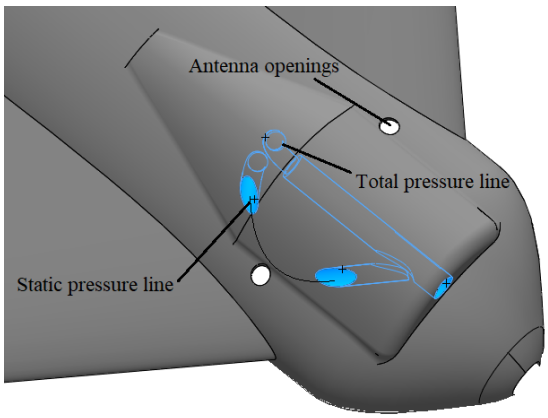

Figure 5.14: Pitot-tube and antennas placement

5.1.3 Control surfaces and parachute bay modeling

After having conceived the internal structure of this model, the next part of detail design has been concentrated on the control surfaces, ailerons and rudder. Following size information from Table 4.4, the volume portion corresponding to the moving surfaces has been cut out from the main structure. The removed parts have then be used to create the actual control surfaces. Figure 5.15 shows the main body from which the control surfaces areas have been removed.

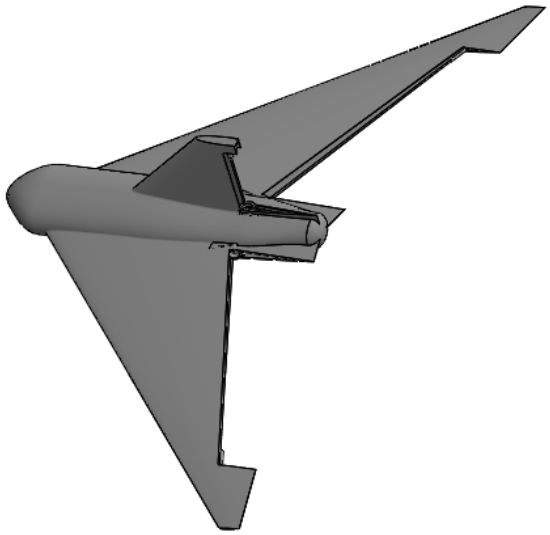

Figure 5.15: Control surfaces cut

In more detail, hinges and servo support structures have been created on the body. To this end, it has been chosen to design a female socket in each in-board part of every hinge, while a male pin in each out-board part. The main reason for this has been that of creating a simple servo-surface coupling mechanism in the first case while not weakening the wing structure in the second. In fact, as it will be shown afterwards, the elevon (or rudder) shaft that couples with the in-board hinge is directly connected to the servo actuator and this is possible only if the moving surface is equipped with a protruding end. Conversely, regarding the outboard side, a pin coming out of the wing fixed structure avoids the need for a hole in the main structure: this is of help to avoid local structural weakening. Figure 5.16 shows closeups of the in-board and out-board hinges as just described.

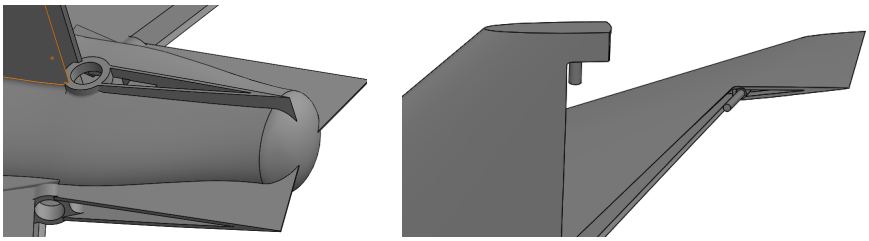

(a) In-board hinges (b) Out-board hinges

Figure 5.16: Hinges closeups

Downstream of this, the actual modeling of the control surfaces took place. After having shortened the surfaces span by 1 mm - in order to allow for a suitable geometric tolerance between the moving and fixed parts - a reinforcement in the moving surface leading edge has been introduced and hinges couplings created. Figure 5.17 shows the the left elevon, in which it is possible to notice the presence of the in-board male hinge (Figure 5.17a) with the servo coupling hole. In Figure 5.17b it is possible to see the out-board female hinge.

(a) In-board hinge (b) Out-board hinge

Figure 5.17: Elevon model

Similarly, Figure 5.18 shows the main features and hinges of the rudder element.

(a) In-board hinge (b) Out-board hinge

Figure 5.18: Rudder model

At last, in the areas corresponding to the hinges has been equipped with proper servo fixing points. These entities features two stands on which the servo structure can be screwed, aligning the pinion axis to that of the control surface hinge. Figure 5.19 shows the just mentioned component.

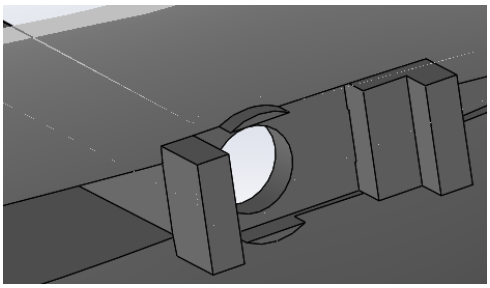

Figure 5.19: Servo supports

Additionally, the parachute bay has been also designed. An opening has been created in the aft lower portion of the fuselage and the removed part has been used to create the lid. Figure 5.20a show the parachute bay opening, from which it is possible to notice one of the two supports on which the servo dedicated to trigger parachute deployment will be fixed. Figure 5.20b, instead, show the lid that keeps the parachute in place while not deployed. As it is possible to notice, it features a rounded slot in which the retaining hook can engage.

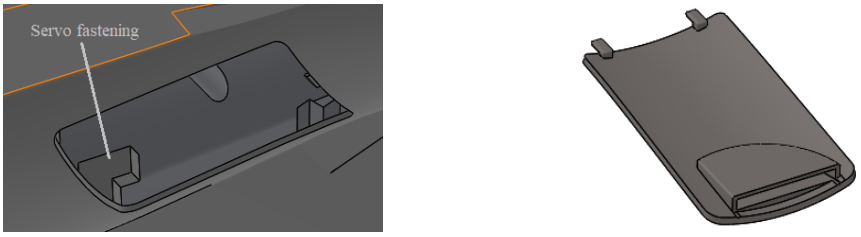

(a) Bay (b) Lid

Figure 5.20: Parachute bay and lid

5.1.4 Structural reinforcements

Once having completely defined these main geometric features, the following phase has been that of designing suitable structural reinforcements. To this end the standard aeronautics practice has been applied: every point load must be applied at the intersecting point of at least three structural elements. Since the main source of point loading are the control surfaces hinges, spars and ribs have been added to the already present skin to create the triad of structural elements just mentioned. Figure 5.21 shows the reinforcement designed for the wing, while Figure 5.22 the ones applied to the vertical stabilizer.

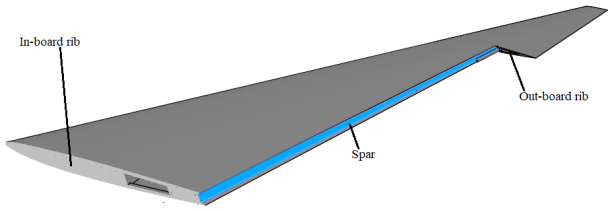

Figure 5.21: Wing reinforcements

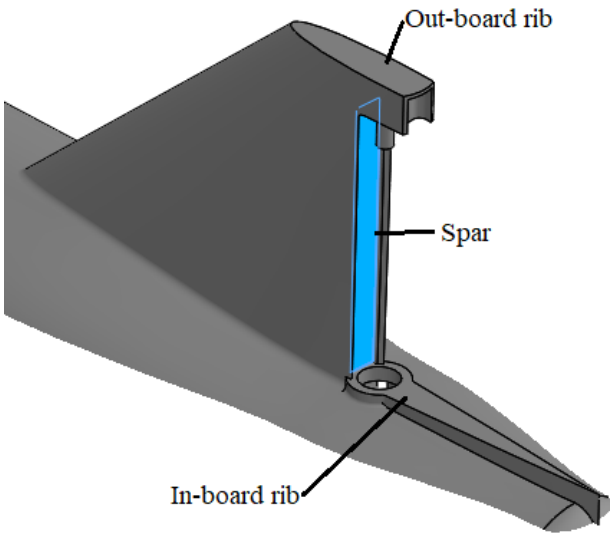

Figure 5.22: Vertical stabilizer reinforcements

5.1.5 Ballast placement

As a final step of the structural detail modeling, the ballasts placement has been performed. Considering that *Ballast5* and *Ballast7* have already been introduced, only the missing ones have been added in this last step. Figure 5.23 shows the placement of *Ballast1-2-3-4* in compliance with Table 4.6. Similarly, Figure 5.24 shows the placement of *Ballast6* in the upper part of the forward fuselage.

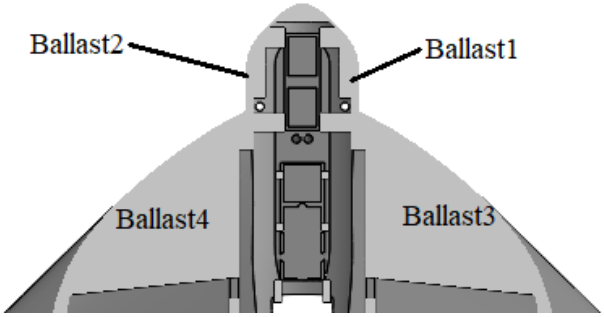

Figure 5.23: Ballast1-2-3-4

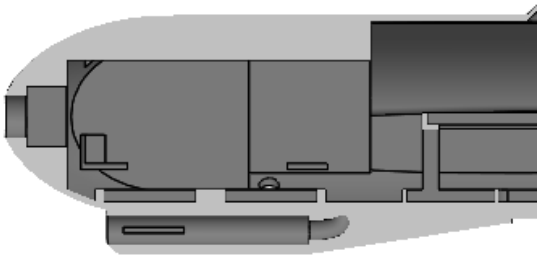

Figure 5.24: Ballast1-2-3-4

As already mentioned before, ballasts have been created by inserting a solid volume infill in the portions of the structure where such components have been designed to be.

5.2 3D print

Once the 3D CAD model has been completely determined the following phase has been that of prototyping. As aforementioned, the technology adopted to manufacture this model has been 3D printing. For this reason it has been necessary to undertake an evaluation study to determine the most suitable strategy to have the model printed. The main driving factor for this study are the 3D printer specifications. The employed model is the *Bambulab X1E* and further technical features are listed in Table 5.2.

Bambulab X1E	
Printing volume	25.6x25.6x25.6 mm
Nozzle size	0.4 mm
Min. layer height	0.08 mm

Table 5.2: 3D printer features

5.2.1 Printing preparation

Since the printing volume is significantly smaller than the aircraft size, the need for printing the model in separate pieces arises. For this reason, the model has been cut in sub-parts that would fit within the printing volume. This lead to the decomposition of the model in several parts. In order to preserve the structural integrity of the model, the main goal has been that of reducing the total amount of parts needed: in this case, the aircraft has been divided into 5 parts and a Pitot holder lid. This subdivision is represented in Figure 5.25.

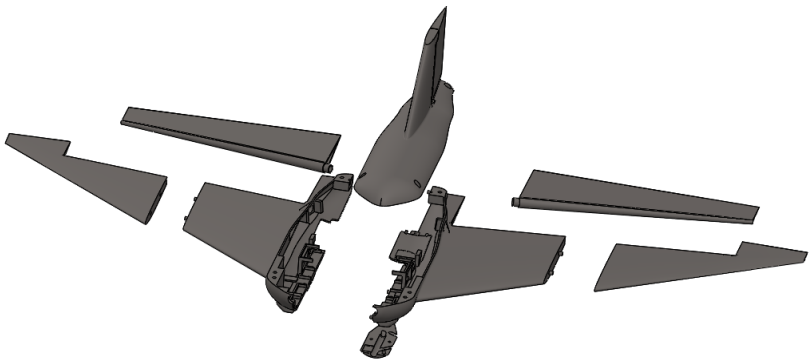

Figure 5.25: Model subdivision

Upper fuselage

In the first place, the upper fuselage canopy has been derived from the original model. It has been chosen to consider the assembly composed of this aircraft part and the rudder as a single entity mean to be printed in a single run. This strategy is useful to reduce the total amount of parts in which the model will be cut, since the rudder does not require any assembling. In addition, to facilitate the assembly of the whole aircraft, three aligning pins have been added in the lower part of this component: two in the forward part and one in the aft section. In order to securely fasten this canopy to the lower fuselage body, four screw holes have been obtained: these elements have been sized to be used with M3 screws.

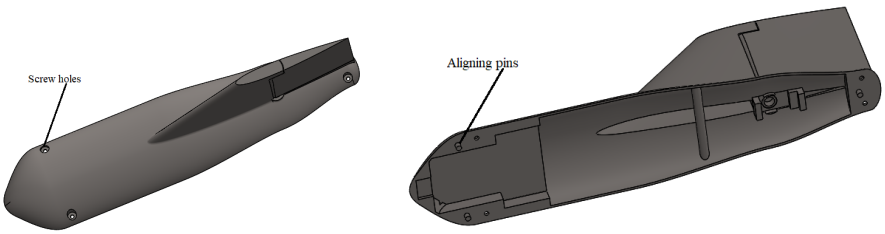

(a) Top view (b) Bottom view

Figure 5.26: Upper fuselage

As it is possible to see in Figure 5.26a, four counterbore holes have been placed at the extremities of the canopy, while Figure 5.26b shows the position of the aligning pins.

Lower fuselage

Coming to consider the counterpart of the just described component, the two sub-unities in which the lower fuselage has been divided are described hereafter. In order to obtain pieces that would fit within the available printing volume, this lower unit has been divided with respect to the longitudinal plane, resulting into two symmetric entities. Similarly to the previous element, three aligning pins have been added to the latter, while no screws have been designed to be employed. The reason for this is that the presence of the upper canopy and the lower Pitot-tube lid provide enough integrity so that a dedicated fixing design is not necessarily required. Figure 5.27 reports details of these two sub-parts. In particular, the left-hand side, shown in Figure 5.27a, is equipped with the three pins that fit into holes present in the right-hand side (Figure 5.27b). Both units are equipped in their upper face with three holes corresponding to the aligning pins of the upper canopy. Other four holes - two per sub-part - are present to house the M3 threaded inserts in which the upper fuselage screws will engage.

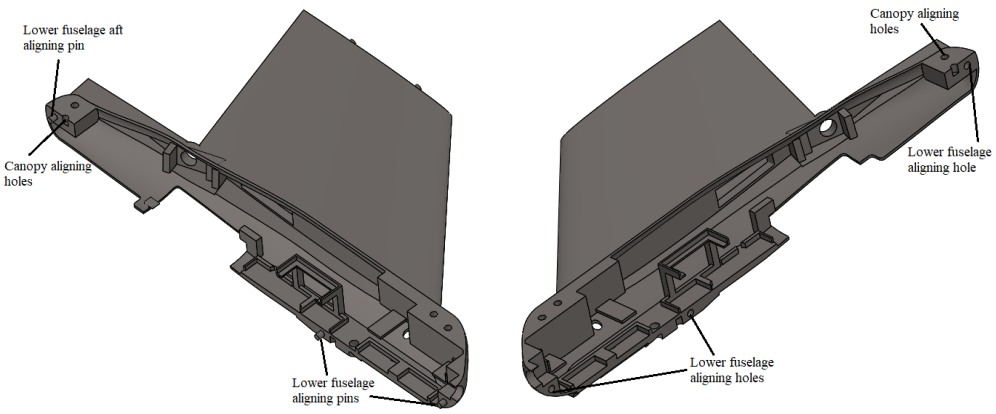

(a) Left-hand side (b) Right-hand side

Figure 5.27: Lower fuselage parts

The bottom part of the fuselage lower body accommodates the Pitot-tube. To make the installation of

the latter viable without disassembling the whole body unit, a dedicated lid has been conceived. This is fixed to the aircraft body through two aligning pins and two M3 screws. This is shown in Figure 5.28.

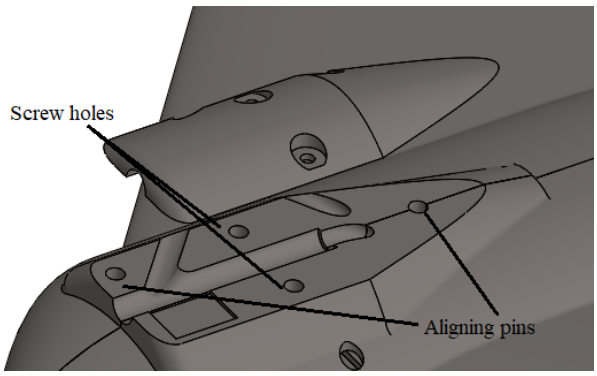

Figure 5.28: Pitot-tube lid

Wing extremities

The remaining elements to be described in this discussion are the wing extremities. Similarly to the previously described couplings, also in this case a pair of aligning pins has been conceived for each wing extremity. This time, however, the junction between the latter and the main body part is guaranteed by gluing. In order to increase local structural strength and surface adhesion, an extra rib has been inserted. The latter also acted as the basis on which the aligning pins and holes have been created. Figure 5.29a shows the rib and the carved aligning holes, belonging to the main aircraft body; figure 5.29b reports the actual wing extremity to which the counterpart of the extra rib is fitted with the above mentioned aligning pins.

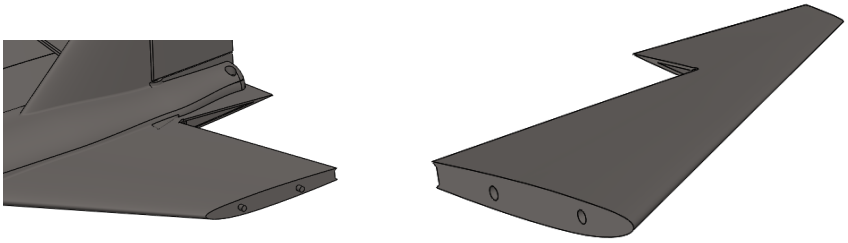

(a) Body pins (b) Wing extremity

Figure 5.29: Wing extremities

At this point, all the elementary pieces have been defined and optimized for the manufacturing process. At this stage the actual 3D printing of the model took place.

5.2.2 Printing process

The first step of creating any object through 3D printing is that of obtaining a 3D mesh model from the CAD and importing it in a slicing environment: these steps are fundamental to obtain the set of instructions that, once loaded on a printing machine, enable the actual part manufacturing. In this regard, each of the aforementioned sub-parts of the glider model have been exported from the SolidWorks environment in the *.3mf* format. This standard - that stands for *3D Manufacturing Format* - is a good compromise of file weight, model resolution and ease of use. In fact, the *.3mf* file format allows to create a 3D mesh structure of the CAD model maintaining original scaling and sizes and adapting its refinement to local level of detail. Many other file formats have been tested, including *.stl* and *.stp*, but eventually most suitable also from a compatibility and portability standpoint resulted to be the *.3mf*.
Once obtained every 3D object, they have been imported in the *BambuStudio* slicing environment. In this phase the print plates have been arranged. When possible, multiple object have been placed on the same plate allowing to save time and to optimized the printer resources. Nevertheless, each object has

been printed with specific settings: this has been done to optimize the printing time while not scarifying the resulting quality. In this matter, the adaptive layer control resulted to be particularly useful. This setting allows to slicing software to automatically adapt each printing layer thickness to the local object curvature. This means that the portions of an object characterized by (nearly) vertical features will be printed with higher layer thickness than those parts where the slope gradient is particularly high. Figure 5.30 shows the adaptive thickness functionality in action: red areas, characterized by almost vertical walls are printed with a relatively high layer thickness (approximately 0.28 mm), conversely, green areas where the curvature is high are manufactured adopting a much thinner layer height (0.08 mm). This makes it possible to obtain smooth curved surfaces without wasting time on straight ones.

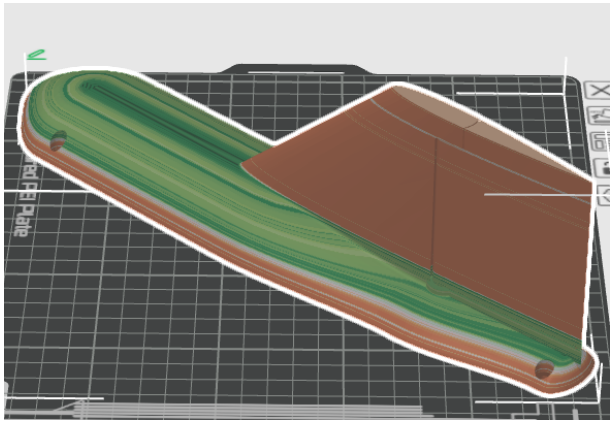

Figure 5.30: Adaptive thickness

Another useful general setting has been set on the printing supports. Since 3D print creates an object by subsequent layers, when dealing with overhanging portions of an object it is necessary to build print supports on which deposit the constituting material. Generally, these print supports require a lot of material and are difficult to remove from the actual object without leaving any trace. In this project, though, tree supports have been employed. As the name suggests, these structure are composed of a main trunk from which different branches depart. This allows to save a lot of material and, since the contact area between the part and the support is drastically reduced, it also easier to remove the stands without leaving traces on the final object. Figure 5.31 shows a sliced file in which the aforementioned settings have been applied. The orange part is the actual object, while the green one the support structure.

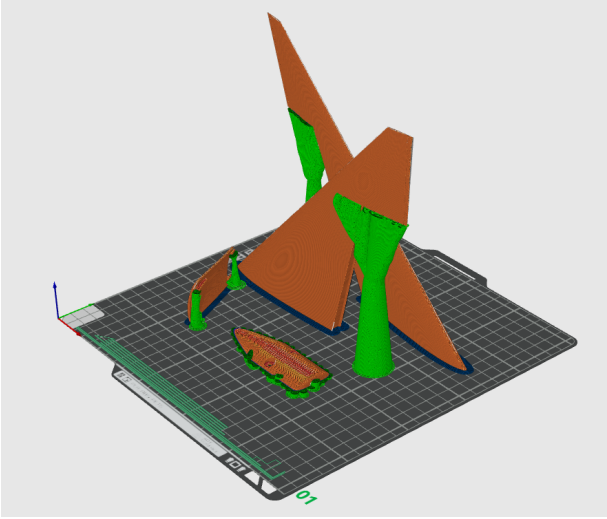

Figure 5.31: Tree supports

However, each object position and orientation has been chosen to minimize the total number of supports

needed: this helps in reducing the amount of needed material and decreasing the overall print time. The print plates have been organized as follows:

- **Plate 1**: two wing extremities, Pitot-tube lid and parachute lid;
- **Plate 2**: upper fuselage canopy;
- **Plate 3**: right-hand lower fuselage body;
- **Plate 4**: left-hand lower fuselage body;
- **Plate 5**: two elevons.

This plate arrangement is shown in Figure 5.32

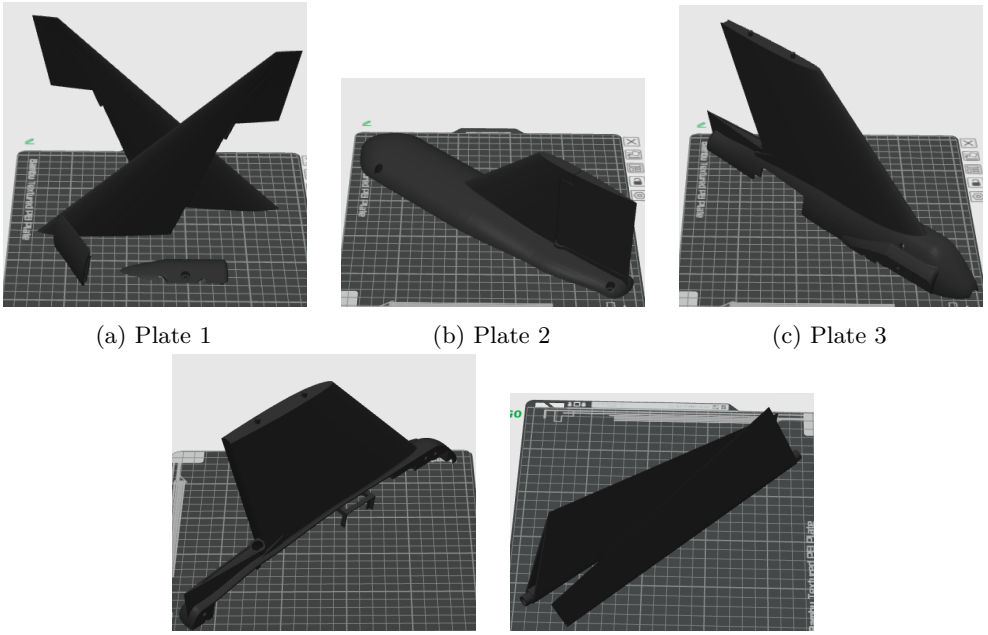

(a) Plate 1 (b) Plate 2 (c) Plate 3

(d) Plate 4 (e) Plate 5

Figure 5.32: Print plates

At this stage the print of every element has been performed and the resulting parts are shown in Figures 5.33a through 5.33i.

(a) Upper fuselage

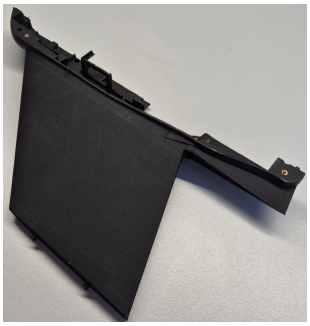

(b) Left hand lower fuselage

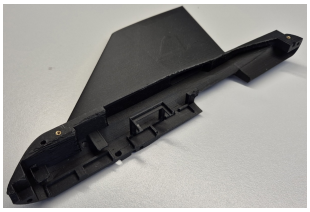

(c) Right hand lower fuselage

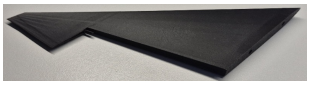

(d) Left hand wing extremity

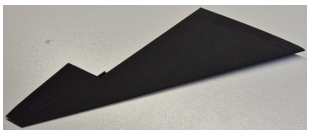

(e) Right hand wing extremity

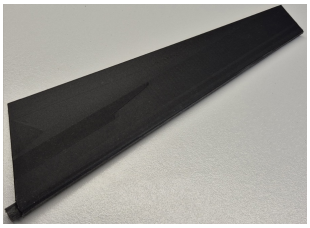

(f) Left elevon

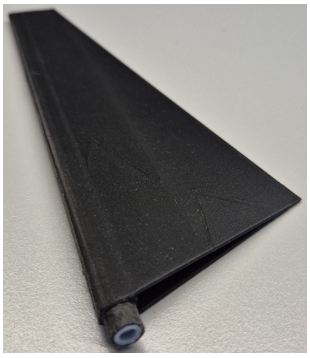

(g) Right aileron

(h) Parachute lid

(i) Pitot lid

Figure 5.33: Structural components

5.3 On-board avionics

After having completely defined the aircraft structure in more concrete terms and having described the main phases to manufacture it, a description of the on-board system architecture is presented hereafter. The first step has been that of designing the system wiring scheme, in which every component connection is presented. This diagram is shown in Figure 5.34 and for each connection the following information is reported:

- length: this is the minimum length assigned to each connection;
- built-in connector: this indicates the connector type each device comes with;
- connector polarity: this shows how the connector is meat to be oriented.

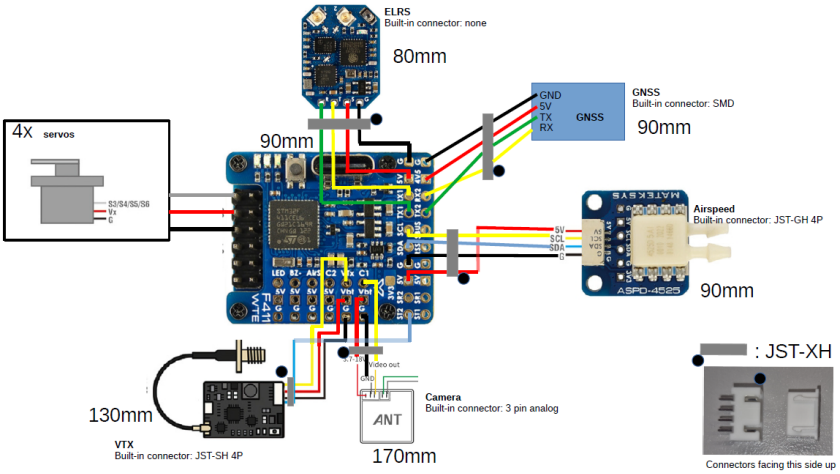

Figure 5.34: Wiring scheme

As it is possible to see, every peripheral device comes with a specific and different connector. Nevertheless, to the aim of standardizing the connecting interface of each element, every connector has been substituted with a JST-XH one. In particular, every female part of this connector has been associated to the FCC: it has been chosen to do so because the main power source is the FCC itself; thus, not having electrically charged protruding elements helps in avoiding the risk of short-circuits if some of the interfaces are ever left unplugged. Consequently, the male counterparts have been attached to the peripheral devices. A detail worth mentioning is that while the female connectors are intended to be crimped on wires connected to the motherboard, male counterparts are meant to be directly soldered on a PCB (Printed Circuit Board). Due to minimal space and weight constraints this solution could not be applied. For this reason, also the male connector has been soldered on the wires departing from the various devices. Figures 5.35a through 5.35f show the final results of these operations.

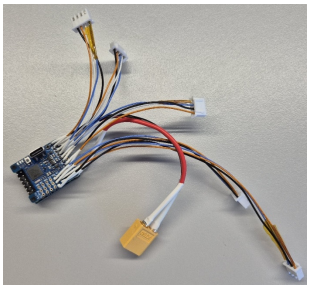

(a) FCC

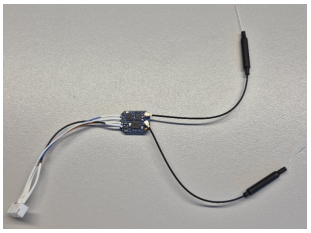

(b) ELRS

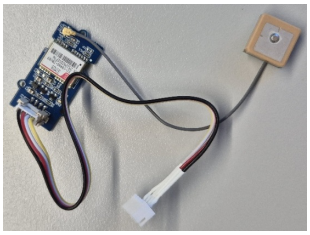

(c) GNSS

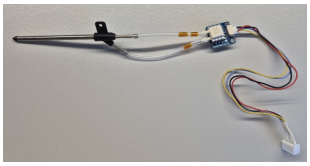

(d) Airspeed

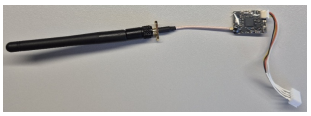

(e) VTX

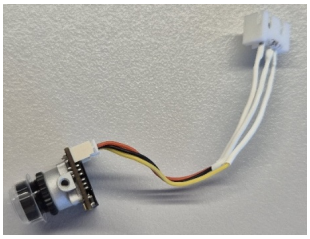

(f) Camera

Figure 5.35: Avionics components

Chapter 6

Assembly, integration, validation and testing

6.1 Assembly

Once every glider component has been manufactured, the actual assembly phase can be performed. In this matter, a fist insight in the structure building procedure is shown in the following steps.
The first step consists in assembling the the two halves wings and the associated elevons. To this end, the in-board elevon hinges have to be fitted in their female counterparts of the main body. Subsequently, after having inserted the wing extremities outboard hinges pins in the respective elevons cavities, the wing has to be assembled following with the aid of the aligning pins. Schematic in Figure 6.1 shows these first assembly steps.

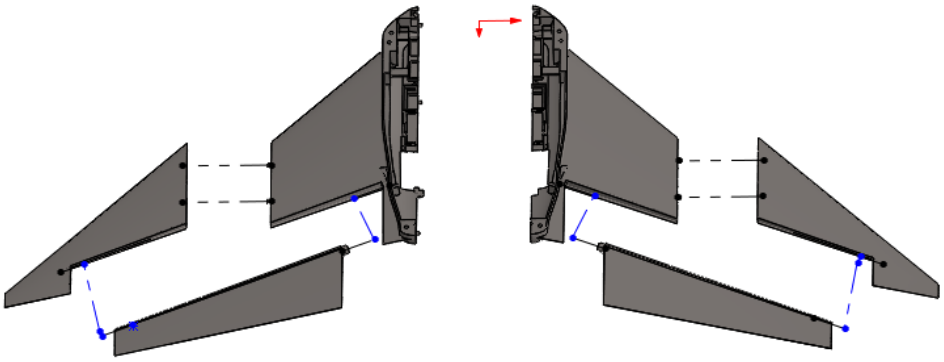

Figure 6.1: Wing assembly schematic

Once having completely put together the wing structure, the main body structure can be assembled. To do so, the two subparts constituting the fuselage can be joined precisely thanks to the three aligning pins. This is shown in Figure 6.2.

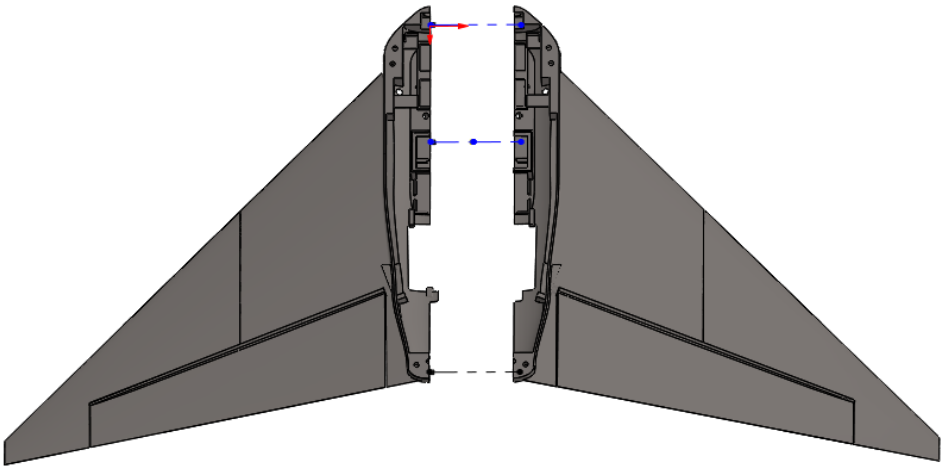

Figure 6.2: Exploded view 1

At this stage, the structure is ready to accommodate all the internal avionics. It is worth noticing that all the elements put together up to this stage constitute the portion of the glider that would not require future disassembly. This is because all the avionics components and the Pitot-tube can easily be accessed from the upper canopy or the respective lids. For this reason, the aforementioned elements can be joined with permanent type solutions, such as gluing. Conversely, the elements stated hereinafter will be bonded to the rest of the structure using screws: this allows for an easy, rapid and repeatable disassembly of the canopy and the lids. Figure 6.3 shows the upper canopy and Pitot-lid aligning pins couplings.

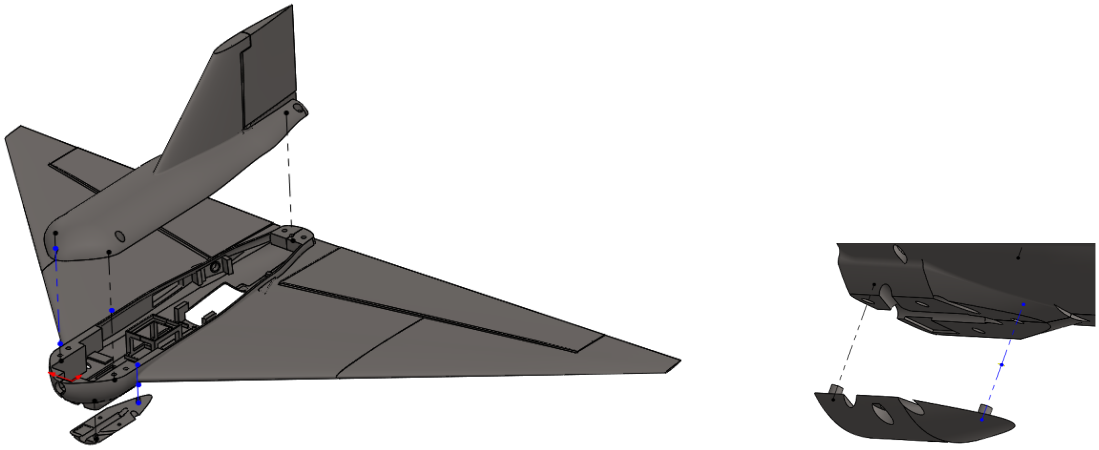

(a) Upper canopy (b) Pitot lid

Figure 6.3: Canopy and lids schematics

Figure 6.4 shows an overall schematics of the avionics positioning.

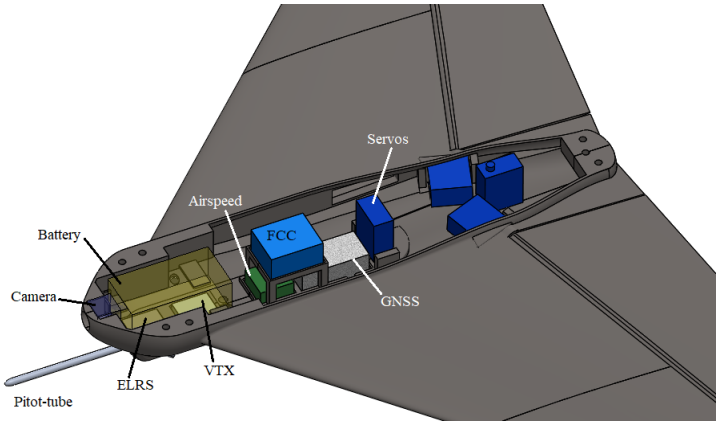

Figure 6.4: Avionics overall view

6.1.1 Real-life assembly

Now that an overall view on the assembly has been provided, the actual, concrete, real-life model construction will be presented hereafter. The following steps report the subsequent phases needed to fully assemble the glider model.

Wing and servo assembly

As already mentioned in the previous part, the assembly process starts from the construction of the two halves wings. The first step consists of inserting and gluing a grooved insert in the aileron in-board hinge hole and then inserting the latter in the corresponding fuselage hinge housing. This allows the servo pinion to be properly engaged with the control surface. The same operation can be performed on the upper canopy to prepare the rudder to be interfaced with the associated servo. Figure 6.5 shows the result of the just mentioned operation.

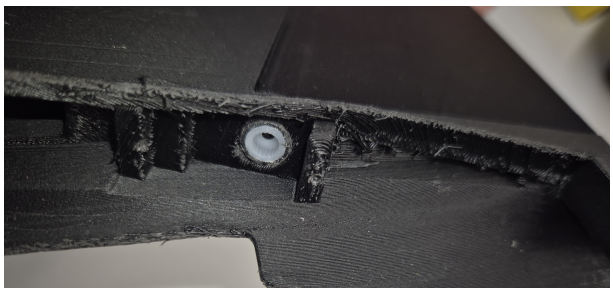

Figure 6.5: Servo grooved insert

After this, it is possible to install the servo in the corresponding housing, screwing its structure to the designed supports. Eventually, the wing extremity can be fitted and glued to the aircraft main structure. This completes the wing assembly phase, leading to the result shown in Figure 6.6.

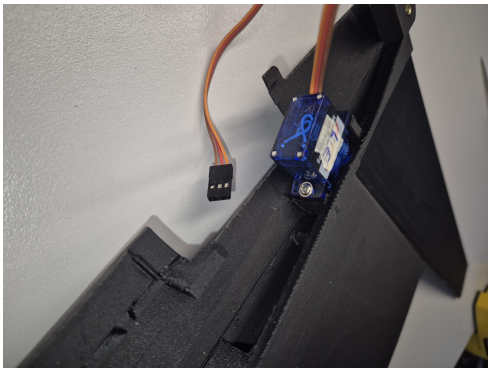

(a) Servo fitting

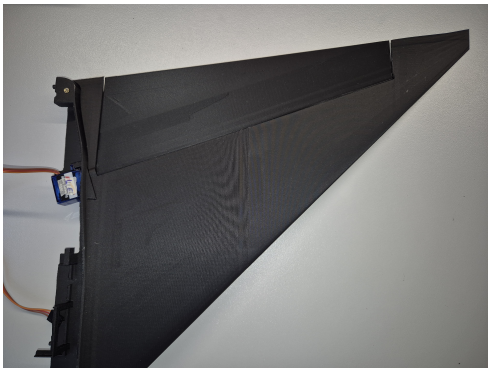

(b) Half-wing structure

Figure 6.6: Wing construction

Similarly, the rudder control servo can be fixed to the aircraft structure. This is shown in Figure 6.7.

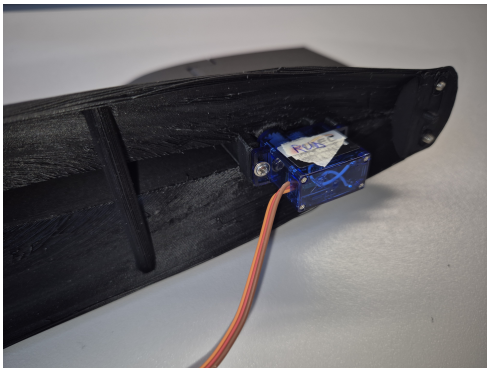

Figure 6.7: Rudder servo

Lower fuselage assembly

Now that the two sub-components of the fuselage have been put together, it is possible to proceed with the final assembly of the lower aircraft body. Prior to do so, it is convenient to add the threaded inserts in the designed holes, as shown in Figure 6.8.

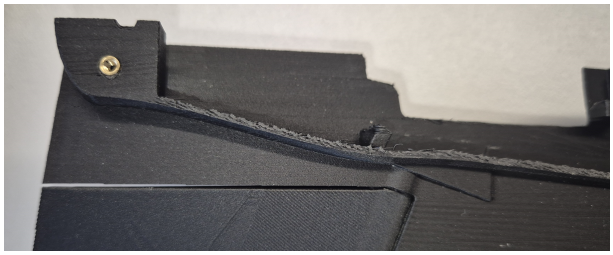

Figure 6.8: Threaded insert

At this stage, it is eventually possible to merge the two main body components and obtain the complete structure of the vehicle lower body. The result of this operation is presented in Figure 6.9.

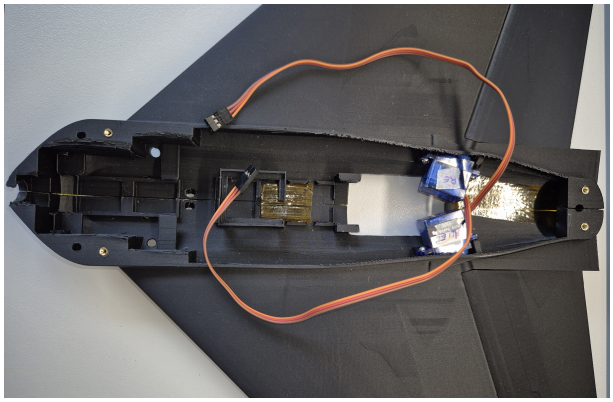

Figure 6.9: Lower body structure

In this regard, it is also worth noticing the parachute actuator installation: once again, the structure of the latter is directly placed on the dedicated supports with the releasing hook facing downwards, as shown in Figure 6.10.

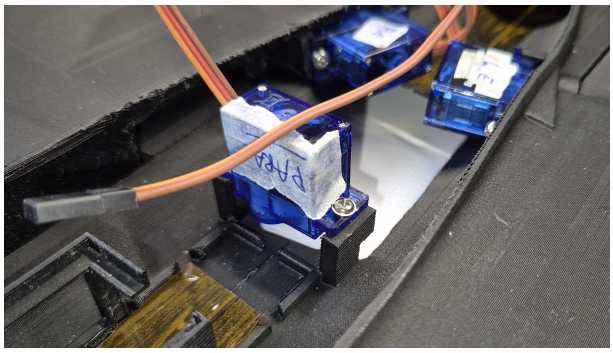

Figure 6.10: Parachute deployment servo

Upper canopy assembly

Since the rudder has been printed directly in its final location, no specific assembly is required, other than servo fitting and coupling with the moving surface. Figure 6.11 shows an overall view of the aircraft structure, where all the servos have been fitted in the respective slots and the upper canopy has been provided with fastening screws.

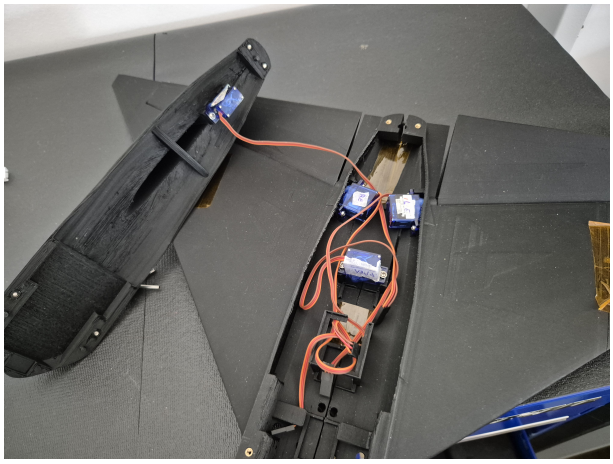

Figure 6.11: Structure assembly overview

6.2 Integration

After having completely assembled all the structural components of the aircraft, the following step consists of installing all the avionic on-board equipment. In this discussion, every element will be covered following the most viable integration order.

ExpressLRS module

The first element to be installed is the ExpressLRS module. This components sits in the forward, lower housing, with close access to the antenna openings to allow the latter to be mounted in the lower part of the aircraft. Figure 6.12a shows the antenna positioning through the dedicated holes, while Figure 6.12b represents the transceiver installation.

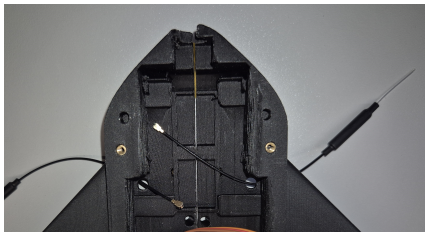

(a) ELRS antennas

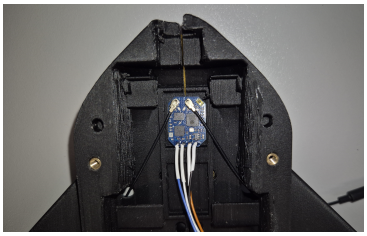

(b) ELRS module

Figure 6.12: ELRS integration

Camera

After the first radio communication module, the analog camera can be installed. Its dedicated housing is placed in the most forward portion of the aircraft fuselage, so that the objective can clearly stand out of the nose structure. As shown in Figure 6.13, the camera wiring is passed underneath the battery supports.

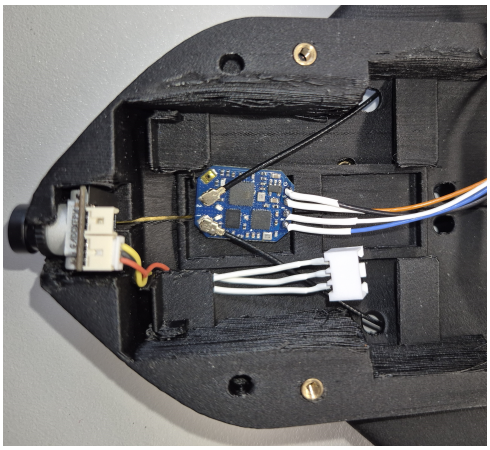

Figure 6.13: Camera integration

VTX module

Following the camera module, the VTX unit can be installed. This element sits next to the ELRS one, with the possibility to expose its antenna outside of the aircraft structure. Figure 6.14 shows this element in its final place.

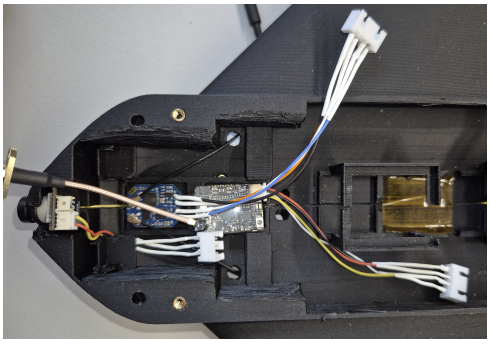

Figure 6.14: VTX integration

Airspeed module

Proceeding with the installation of the avionic modules, the following element to be installed is the airspeed sensor and the Pitot-tube. First of all, it is necessary to let the total and static pressure pass through the aircraft structure to allow a connection between the probe and the transducer. After this is possible to connect the piping to the respective ends. Figure 6.15a shows the connection to the transducer, while picture in Figure 6.15b features the probe piping. To fix all these elements in place, the dedicated lid can be eventually screwed to the structure, as shown in Figure 6.15c.

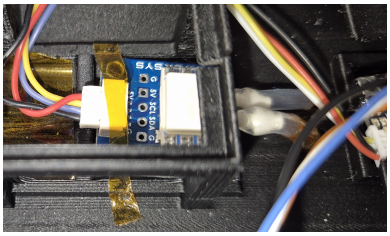

(a) Airspeed module

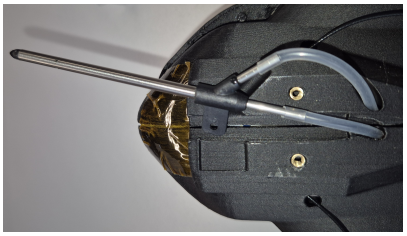

(b) Pitot-tube

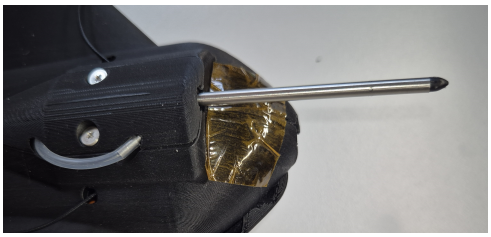

(c) Lid

Figure 6.15: Airspeed integration

GNSS module

The last peripheral module to be installed is the GNSS one. This element sits in the slot between the airspeed module and the parachute bay opening. Since this unit is provided with a pad antenna, it is necessary to pay careful attention to the positioning of the latter. GNSS satellite signal is really weak: for this reason it is advisable to place the receiving antenna on top of all the wiring, in order to avoid possible electromagnetic interference. Figure 6.16 shows this element in its designed installation place.

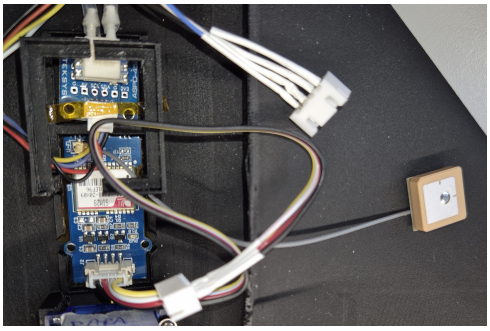

Figure 6.16: GNSS integration

FCC module and wiring

At last, the FCC module can be placed on its designed support. As it is possible to notice from Figure 6.17, this element has been bonded to its support structure with a proper fastener. This precaution is needed to avoid inadvertent movements that may compromise the aircraft stability or the electrical connections continuity. The other elements don't need such retaining systems because the tight avionic bay spaces are sufficient to prevent this occurrence.

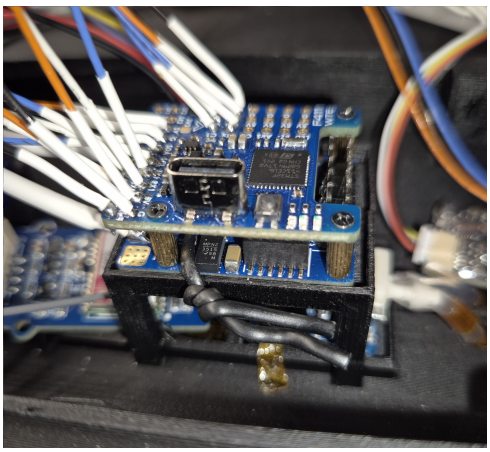

Figure 6.17: FCC integration

At this stage it is possible to connect every device to the central FCC unit, as displayed in Figure 6.18a and, subsequently, place the wiring in the available space aside of the already installed items. This is showcased in Figure 6.18b. At this stage also the servo actuators can be connected to the FCC.

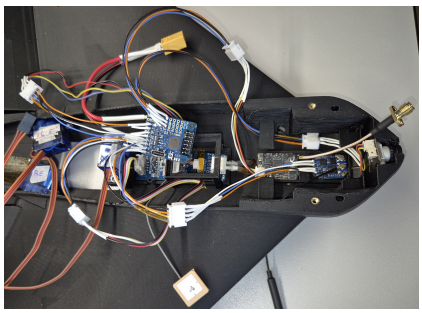

(a) Devices connections

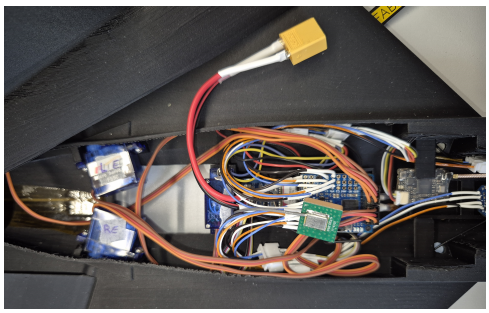

(b) Wiring disposition

Figure 6.18: On-board connections

Battery connection

To complete the installation and make the on-board system operative the last step is connecting the LiPo battery. Upon connection, the system automatically turns on and the firmware is booted. Battery connection and final wiring placement is shown in Figure 6.19.

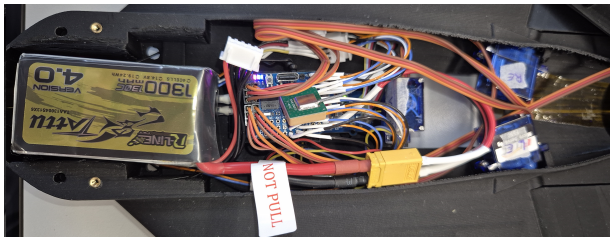

Figure 6.19: Battery connection

At this stage, it is possible to close the upper canopy and securely screw it to the main structure. This completes the aircraft assembly and integration. This is shown in Figure 6.20.

Figure 6.20: Overall assembly

6.3 Validation and testing

Once the manufacturing and integration phase has been completed, the validation and testing phase has been performed. In this matter, a detailed evaluation of the aerodynamic properties of the model has been carried out. This allowed to determine more precise aerodynamic loading distribution, which has been fundamental to perform structural strength evaluations on the most stressed element: the wing and the elevons.
In addition to this, also the operation of the avionic system has been checked. In particular, the GNSS and Airspeed sensors have been tested separately and, subsequently, the whole architecture has been verified.

6.3.1 Aerodynamic and structural validation

As already mentioned, this first evaluation concerned an analysis of the aerodynamic properties of the wing, aiming to evaluate:

- the pressure distribution over the wing surface;
- the total force generated by the lifting surfaces;
- the force acting on the mobile surfaces, in order to estimate the hinge moment.

The results of this fluid dynamics evaluation have eventually been used to test the structural resistance of the model and to evaluate its strain.

Aerodynamic simulation

In order to verify the quality of the obtained design, a CFD analysis has been performed performed using the Flow Simulation tool integrated within the SolidWorks environment. A test has been carried out on the half-wings structure, consisting of a fixed part and a movable part connected by a hinge constraint. Simulations have been performed performed for three significant configurations: elevon in neutral position, and at maximum (positive and negative) deflection. The free-stream conditions (velocity and AoA) have been imposed as defines as the trim condition (see Table 4.8), considering ISA conditions at an altitude of 0 m. The computational domain, shown in Figure 6.21, includes the specified boundary conditions. All model openings have been closed using "lids" generated by the simulation environment, and the gaps between the fixed and movable surfaces removed. Air was used as the working fluid, and a solver model capable of representing both laminar and turbulent flow regimes has been employed. The mesh has been refined in regions of smaller curvature radius, helping to gain more precise results where the higher gradients are expected to be.

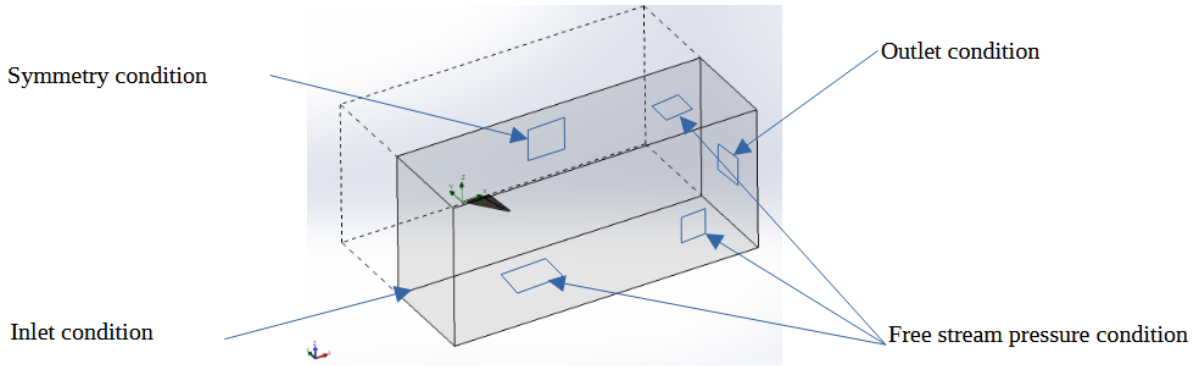

Figure 6.21: CFD domain

Elevon neutral position This first simulation has been run considering the elevon in its neutral position with in trim AoA conditions. Figure 6.22 shows the static pressure distribution in a general section surrounding the model.

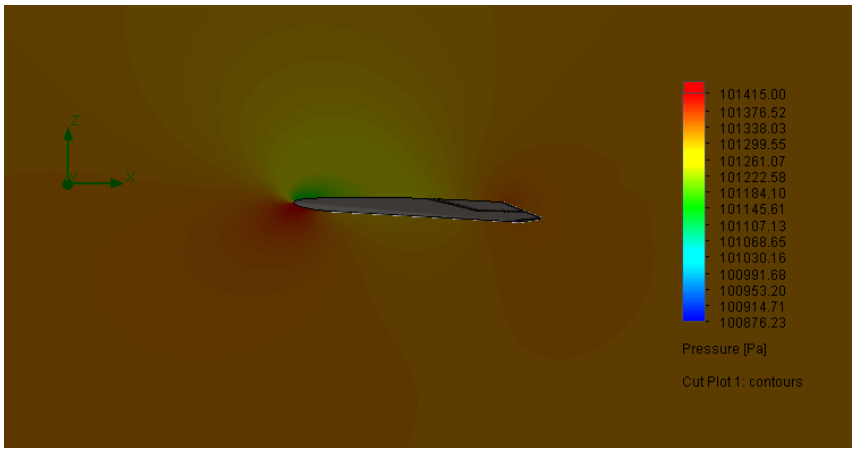

Figure 6.22: Neutral trim condition CFD

As it is possible to notice, in proximity of the leading edge of the wing there's a consistent increase in static pressure: this means that locally the flow speed is very low, leading to the presence of a stagnation point. From this point, following the lower wing surface in the stream direction, it is possible to notice a mild pressure decrease caused by current acceleration. Conversely, in correspondence of the upper wing

surface, a low pressure bubble is present just downstream of the stagnation point. This implies a local and rapid flow acceleration. This is a typical pressure and velocity distribution for a NACA airfoil. Following this point is a region of pressure recovery that, by the trailing edge, brings the static pressure to the same level that insists on the lower side. The overall pressure distribution - with lower pressure acting on the upper side than on the lower one - contributes to create an upward directed force, which is the lift.
Along with this, a the pressure distribution over the model surface has been determined, allowing to calculate the resulting aerodynamic forces. This is shown in Figure 6.23.

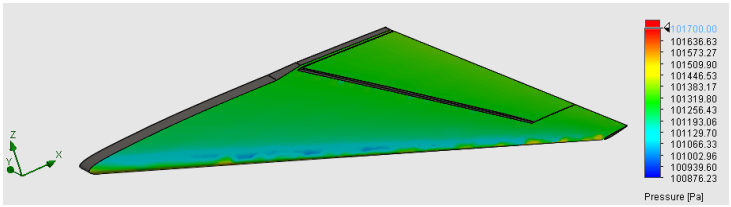

(a) Upper side

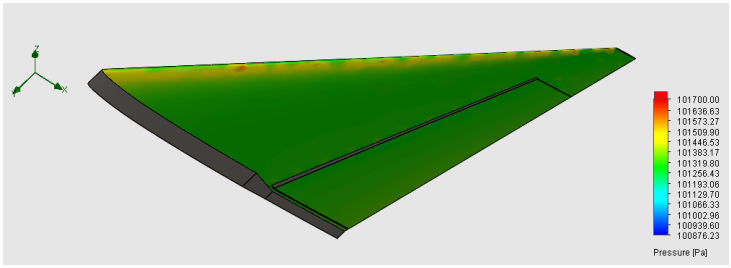

(b) Lower side

Figure 6.23: Skin pressure distribution - neutral elevon

As it is possible to notice, the pressure distribution resembles what observed in Figure 6.22. In fact, it is possible to notice the presence of high pressure areas in the proximity of the leading edge, particularly on the lower surface. Moving towards the leading edge, it is possible to notice the same pressure variation observed in the above presented case. These pressure distribution data have been used to perform the structural evaluations that will be described in the following section. If this pressure distribution is integrated over it the surface on which insists, it is possible to calculate the overall aerodynamic force acting on this half-wing. The results to this operation are shown in Table 6.1.

Quantity	**Value [N]**
X force	0.190
Y force	-0.451
Z force	3.832
Lift	3.809
Drag	0.456

Table 6.1: Overall forces - elevon neutral

The reported values are expressed in the SolidWorks reference frame, which coincides with the nose-fixed one, and show the resulting forces acting on the considered half-wing. The last two rows, instead, report the same quantities expressed in the wind reference frame, hence lift and drag. Considering the equilibrium equation 3.6, it is possible to evaluate if the lift produced by the designed model is suitable to balance the aircraft weight. In particular, the mathematical relation to be satisfied is the following:

$$W \cos \gamma = L$$

where:

- W is the aircraft weight, as reported in Table 4.7;
- γ is the flight path angle, derived from Table 4.8;

- L is the total aircraft lift. Since an only half-wing has been considered in this simulation, this term has to be substituted with twice the value reported in Table 6.1.

Substituting the corresponding terms, the left-hand term results equal to 8.32 N, while the right-hand one 7.62 N. It is clear that the two terms are not equal to each other, but a difference of 0.7 N is present. This fact can be explained considering that this simulation took into account only the wing structure, not considering the fuselage contribution to lift generation. This conduced to an underestimation of the total lift force.
In addition to this preliminary evaluations, a high incidence ($\alpha = 25°$) simulation has also been run. The wing surface pressure distribution is shown in Figure 6.24.

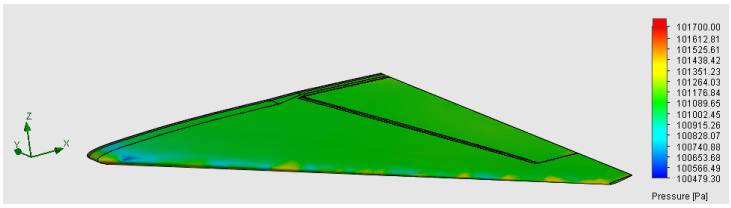

(a) Upper side

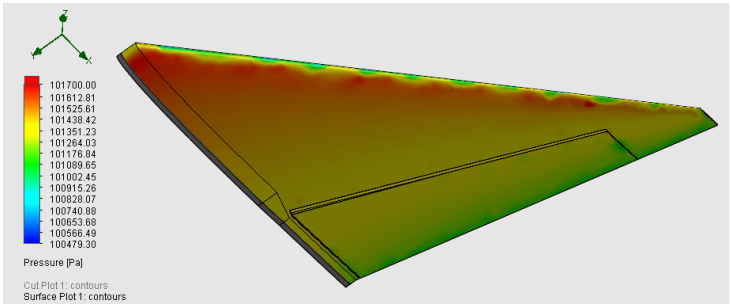

(b) Lower side

Figure 6.24: Skin pressure distribution - neutral elevon - high AoA

The pictures clearly shows that the phenomena already observed in Figure 6.23 are present also in this case. Since the significantly higher incidence condition, the magnitude of the latter is also higher, making them more visible in this representation. Similarly, Table 6.2 shows the total aerodynamic forces.

Quantity	**Value [N]**
X force	0.178
Y force	-1.621
Z force	15.408
Lift	13.88
Drag	6.67

Table 6.2: Overall forces - elevon neutral - high AoA

As it is possible to see, the AoA increase leads to a significant increase of all the aerodynamic forces - considering to maintain the above defined trim airspeed. This shows that with a high AoA attitude great values of loading factor can be reached, or, on the other hand, low-speed flight can be performed at such incidence. Both in this study and in the previous one it is possible to notice the presence of a negative Y force, oriented towards the out-board direction. This can be associated to a wing-tip suction effect caused by extremity vortexes. High pressure from the lower side of the wing tends to move to the upper, low pressure face: this generates a swirling motion originating from the wing-tip. If this phenomenon is animated by a sufficiently high speed, a low pressure area can insist around the wing extremity: this generates a side-pulling resulting force. Nevertheless, thanks to the overall symmetry of the model, it is reasonable to expect this action to be present on both wing-tips, oriented in opposite directions, thus canceling each other. For this reason the effect of this Y force can be neglected.

Elevon maximum deflection - hinge moment estimation Similarly to the just discussed case, the CFD simulation has been run for the condition of maximum elevon deflection. This corresponds to the surface deflection required to implement a pitch-down maneuver. The static pressure distribution on a arbitrary section of the motion field is reported in Figure 6.25.

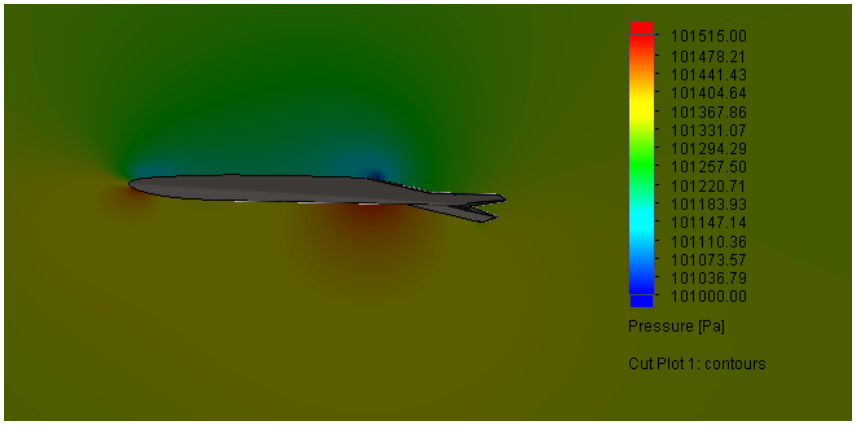

Figure 6.25: Max. deflection condition CFD

Analyzing the results shown in this representation, it is possible to draw the same conclusions as done for the neutral deflection case. In this configuration, though, it is possible to appreciate the presence of high pressure area collocated in the aft part of the wing, approximately where the elevon is placed. This puts in evidence the effect the control surface has on the whole body aerodynamics. The presence of this high pressure area creates an uplifting force in the rear portion of the wing, thus applying a pitch-down moment. This confirms the aileron pitch control effectiveness. Figure 6.26 shows the pressure distribution over the wing surface and it is possible to have a further confirmation of the just mentioned phenomenon.

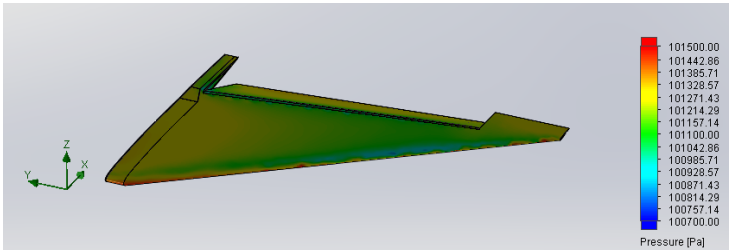

(a) Upper side

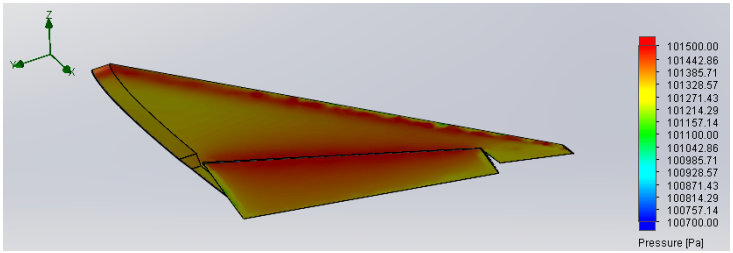

(b) Lower side

Figure 6.26: Skin pressure distribution - max. deflection

The main objective of this case study has been that of evaluating the total force acting on the elevon surface, to the end of estimating the moment acting on its hinge. This analysis is crucial to verify that the selected servos can provide a suitable amount of torque to operate the control surface. In this operating scenario, the total force acting on the elevon resulted equal to 8.23 N.
The strategy adopted to perform the just mentioned check consisted in calculating at what distance from the hinge axis this force should be applied to saturate the maximum torque the servo can generate. If this quantity is higher than the distance between the elevon hinge and its aerodynamic center, then the

servo meets the maximum torque requirements, otherwise the actuator is undersized. In this discussion, the elevon aerodynamic center hasn't been determined, hence to perform this evaluation in the most conservative way, the test has been considered passed if the point of application of the overall force stands out of the control surface. Considering the maximum torque of the actuator, as specified in Table 2.10, the force application point results to be at a distance of 1.43 cm from the hinge axis. This value indicates that real aerodynamic center of the elevon may be at further distance from the axis, requiring a much higher torque to be applied to the surface hinge.
Similarly, the same evaluations have been performed for a maximum (negative) elevon deflection: simulating a full-control pitch-up maneuver. Figure 6.27 shows the flow pressure field distribution, while Figure 6.28 is relative to the wing surface.

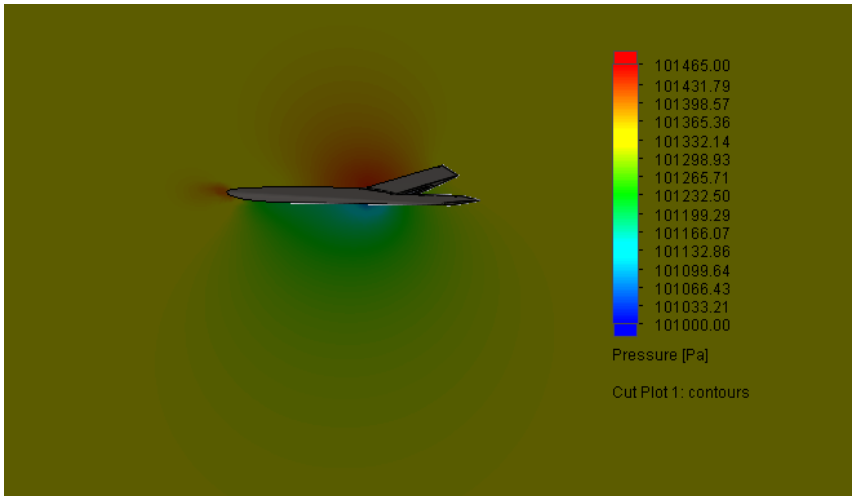

Figure 6.27: Max. (neg.) deflection condition CFD

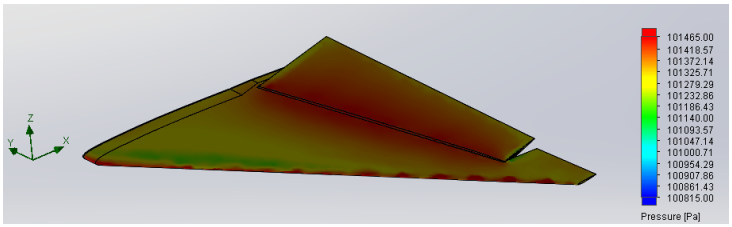

(a) Upper side

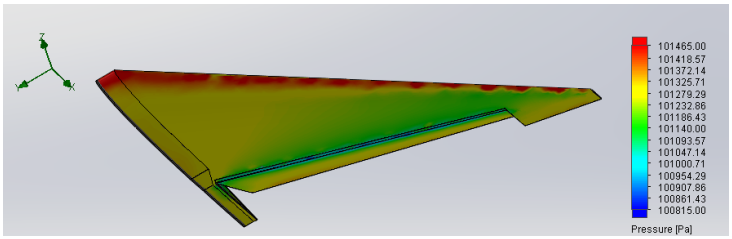

(b) Lower side

Figure 6.28: Skin pressure distribution - max. (neg.) deflection

In this scenario the high pressure bubble is located on the upper side of the wing, thus generating a down-pushing force. This action, thanks to its astern application, forces the aircraft to a pitch-up attitude. This, again, confirms the effectiveness of this control surface.

Structural simulation

Downstream of the determination of the aerodynamic wing loading it is possible to consider the effects the latter has when applied to the aircraft structure. To do so the FEA structural model has been created

within the SolidWorks environment.
As a first step, the model has been imported in the SolidWorks FEA environment, where a 3D finite element mathematical method is employed to evaluate the stress, strain and displacement in each point of the submitted structure. After this, the boundary conditions have been set: the only portion of the model subjected to external constraints is the wing root, on which a clamped condition has been set. Subsequently, the mesh controls have been defined and the mesh has been created. The latter and the application of the boundary conditions can be seen in Figure 6.29. As it can be seen, the mesh is refined with respect to the local object curvature and level of detail.

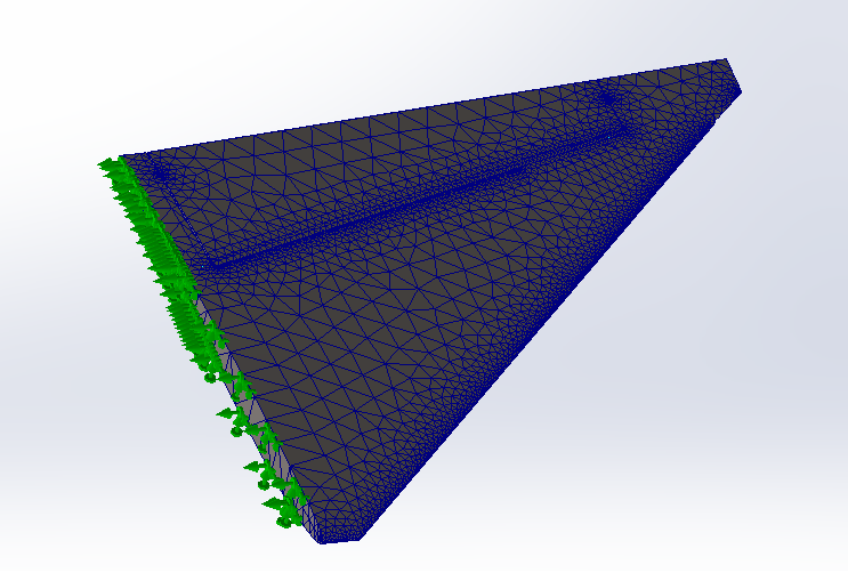

Figure 6.29: Boundary condition and mesh

As a next step, the material mechanical properties have been imposed to the model. The reference values are those reported in Table 5.1. At last, the surface distributed loading obtained through CFD analysis has been applied to the interested parts. One dedicated analysis has been run for each elevon configuration: neutral position and maximum positive and negative deflection. Once completely set, the simulations have been run invoking a static condition solver, obtaining as outputs the stress volumetric distribution - expressed as the Von Mises equivalet stress - and the displacement map.
In the first case scenario, the analysis is representative of the reference trim condition and shows the stress distribution acting on the wing structure and the consequent displacements. Figure 6.30.

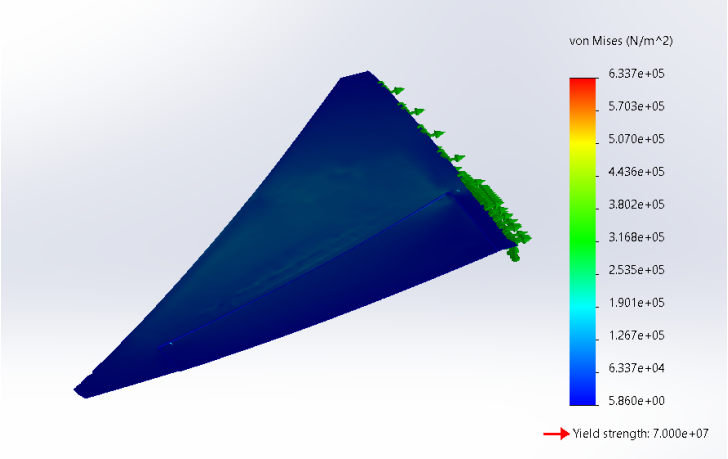

(a) Stress distribution

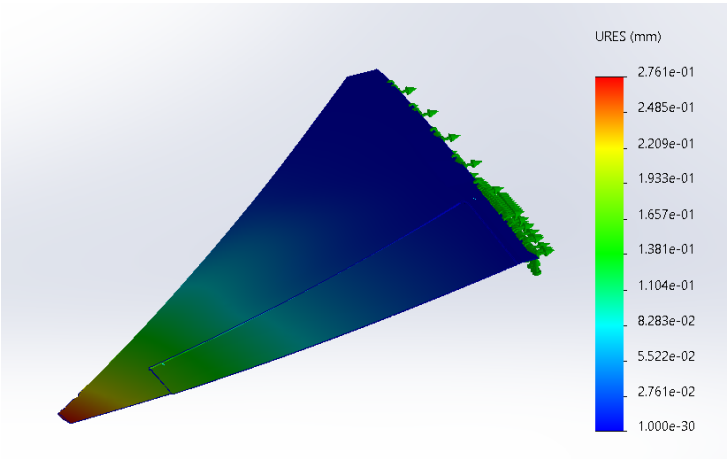

(b) Displacements

Figure 6.30: Neutral deflection FEM analysis

As it is possible to notice, the aerodynamic loading causes an upward bending of the structure as can be expected. Nevertheless, in each point of the model the stress is orders of magnitude lower than the material yield strength. This indicates that in no point of the structure a critical loading is reached: this validates the structural resistance of the model. Regarding the displacement map, instead, the maximum value is found at the wing tip: this is due to the bending action of the aerodynamic loading. Also in this case, though, the reported values are well within the acceptable ranges: the maximum displacement is lower than three tenth of a millimeter, that is small enough to be considered negligible in this matter.
Similarly, the same simulation has been executed for the maximum elevon deflection situation, obtaining the results shown in Figure 6.31.

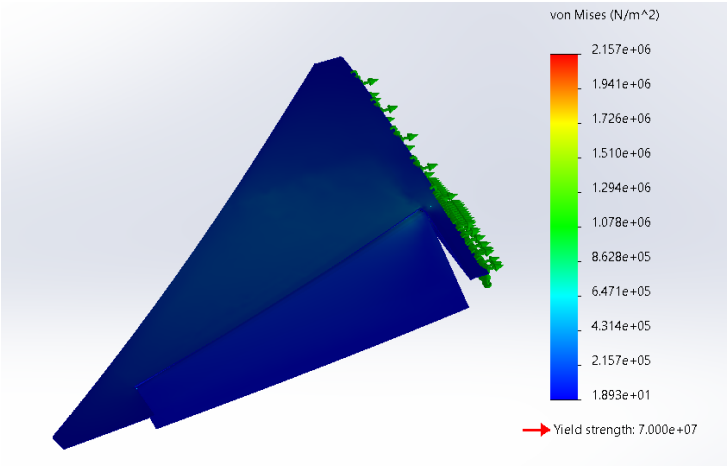

(a) Stress distribution

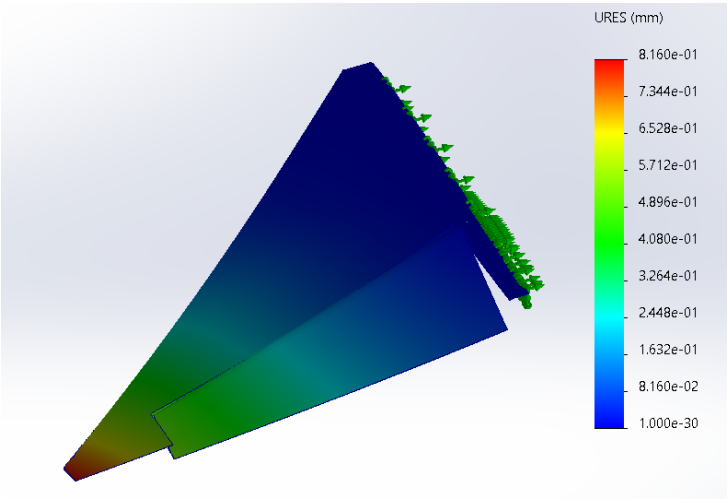

(b) Displacements

Figure 6.31: Max. deflection FEM analysis

In this situation, as in the maximum negative one reported in Figure 6.32, the acting aerodynamic loads are higher than the previous case because of the effect of the deflected elevon. This causes an overall higher stress within the structure and greater displacements. Nonetheless, also in these configurations, the maximum stress is lower than the PLA yeld strength and the maximum displacement at the wing-tip is lower than a millimeter. This ultimately proves the success of the design, even in the condition of elevon maximum deflection.

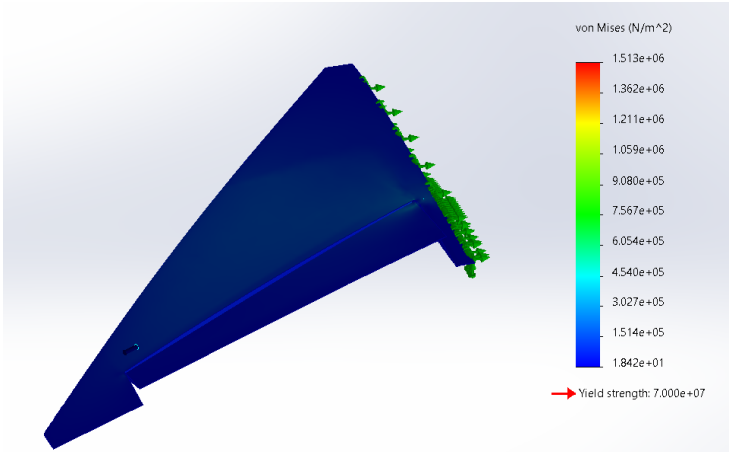

(a) Stress distribution

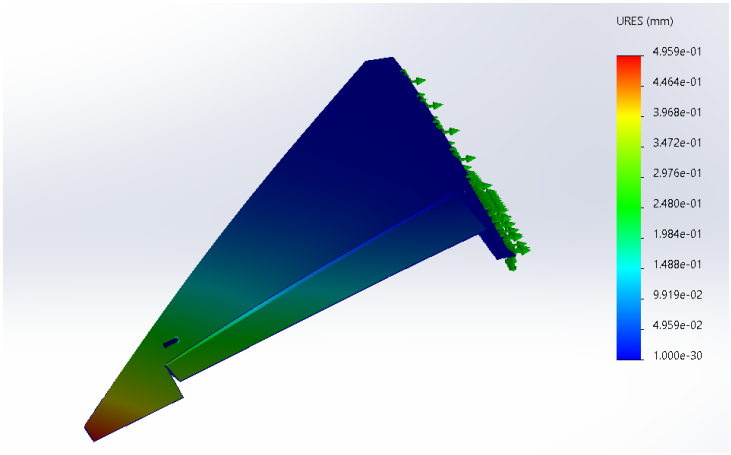

(b) Displacements

Figure 6.32: Max. (neg.) deflection FEM analysis

6.3.2 Avionic system testing

After having validated the structural and aerodynamic properties of this project, a testing and configuration phase of the on-board systems has been undertaken. As a preliminary step, the operativity of the the peripherals has been tested separately and then the complete architecture has been evaluated as a whole. The following paragraphs describe this testing phases.

6.3.3 Sensors testing

The preliminary tests have been concentrated on evaluating the operativity of two of the main components of the avionic system: the GNSS module and the airspeed one. To this purpose, the sensors have been connected to an Arduino board and, after having established a serial communication with a PC, a proper piece of software has been employed to capture the raw sensor outputs and display their readings.

GNSS sensor

The first element that underwent a preliminary phase of testing has been the GNSS module. The aim of this activity has been that of reading the raw GNSS module messages, conform to the NMEA standard, and prove their integrity. Subsequently, the *u-center* environment has been used to interpret the latter and more specifically evaluate their accuracy in terms of geo-location data.
The first step has been accomplished by implementing an Arduino script capable of reading the serial data flow coming from the sensor and displaying the raw message string. After having powered on the peripheral, connected to the Arduino board, it has been necessary to wait for a proper GNSS information signal to establish. This is the time the GNSS chip needs to perform the triangulation calculation with

the signal coming from the satellites. Once completed this procedure, called *cold start*, the raw messages captured by the testing script are displayed in Figure 6.33.

```
$GPGSV,4,4,13,41,,,*7E
$GPRMC,135554.000,A,4504.8292,N,00736.5864,E,0.00,36.54,091025,,,A*5F
$GPGGA,135555.000,4504.8292,N,00736.5864,E,1,9,0.92,284.4,M,48.2,M,,*51
```

Figure 6.33: NMEA raw messages

The reported text shows a series of three NMEA messages. Each message starts with the *$* symbol and is composed of comma-separated values. In particular, the first field describes the message type and its content, while the following ones represent the actual information. The following list reports more detail for the type of displayed messages:

- **GPGSV**: this message string identifies the number of SVs in view, the PRN numbers, elevations, azimuths, and SNR values. Table 6.34 shows the correct interpretation of the fields [18];

Field	Meaning
0	Message ID
1	Total number of messages of this type in this cycle
2	Message number
3	Total number of SVs visible
4	SV PRN number
5	Elevation, in degrees, 90° maximum
6	Azimuth, degrees from True North, 000° through 359°
7	SNR, 00 through 99 dB (null when not tracking)
8–11	Information about second SV, same format as fields 4 through 7
12–15	Information about third SV, same format as fields 4 through 7
16–19	Information about fourth SV, same format as fields 4 through 7
20	The checksum data, always begins with *

Figure 6.34: GPGSV table

- **GPRMC**: this message string shows the position (longitude, latitude and orthometric height), velocity and time data acquired from the sensor. Table 6.35 shows the correct interpretation of the fields [18];

Field	Meaning
0	Message ID $--RMC Talker ID can be: GP: GPS only GN: More than one constellation
1	UTC of position fix
2	Status A=active or V=void
3	Latitude
4	Longitude
5	Speed over the ground in knots
6	Track angle in degrees (True)
7	Date
8	Magnetic variation, in degrees
9	The checksum data, always begins with *

Figure 6.35: GPRMC table

- **GPGGA**: this message string shows the same information type of the previous point but with additional details, such as information about the GNSS satellite constellation the sensor is communicating with.

Thanks to this preliminary check it has been possible to prove the correct functioning of the GNSS module. In has been also possible to see that this element is actually able to provide the FCC with the information needed for this application: longitude, latitude, orthographic altitude and velocity. All these quantities are included in the NMEA raw messages.
At this point, to the end of visualizing the state of the GNSS connectivity and interpret the above described raw NMEA statements in a more user-friendly way, the *u-center* tool has been employed. After having connected the sensor to the PC, via an Arduino-based connection, and after having waited for the *cold start* phase to complete, the following information has been shown by the tool:

- **connection status**: this table, shown in Figure 6.36, reports the basic information about the GNSS connectivity. The most relevant data are about the latitude, longitude, altitude and number of satellites;

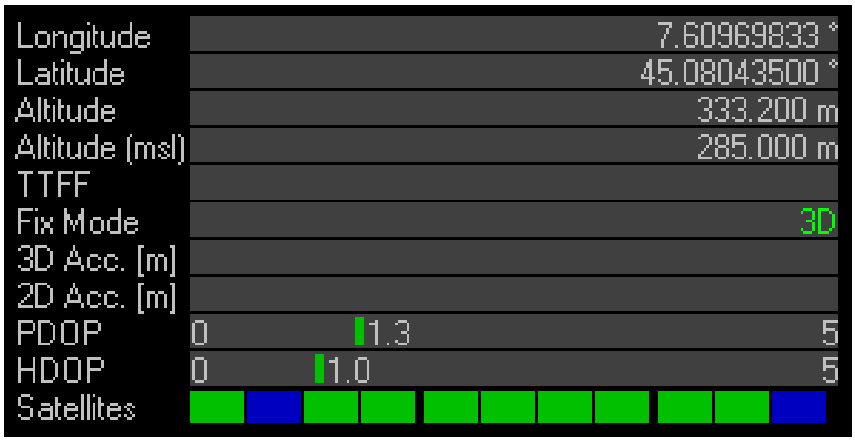

Figure 6.36: u-center status

- **satellites status**: this view, shown in Figure 6.37, gives more detailed information about each satellite link. Some of the reported information includes satellite ID and signal strength in dB;

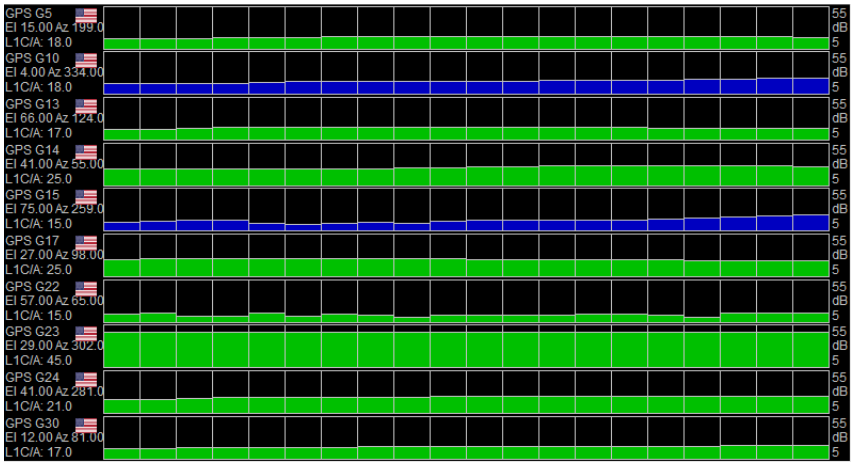

Figure 6.37: u-center satellites

- **satellites map**: this view, reported in Figure 6.38, shows an interpretation of the satellites azimuth and elevation as geographical coordinates, representing the spacecraft position projection on Earth surface;

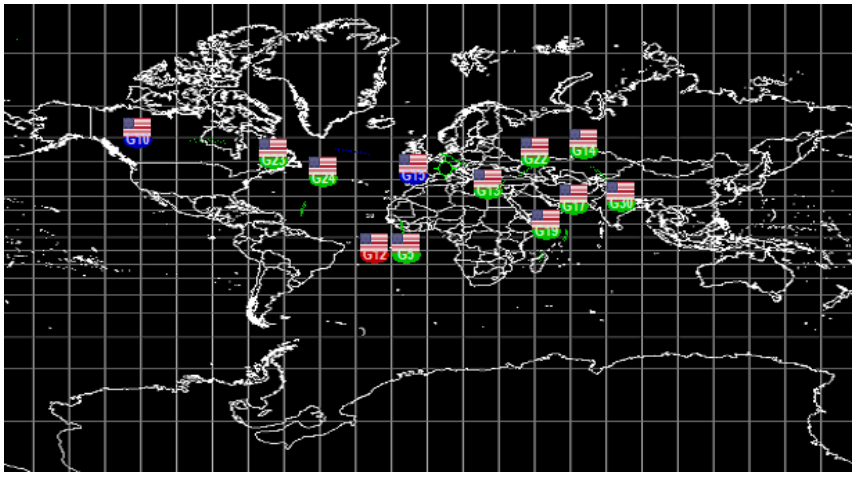

Figure 6.38: u-center satellites map

- **satellites map**: this view, presented in Figure 6.39, shows the representation of the GNSS coordinates on the Earth surface.

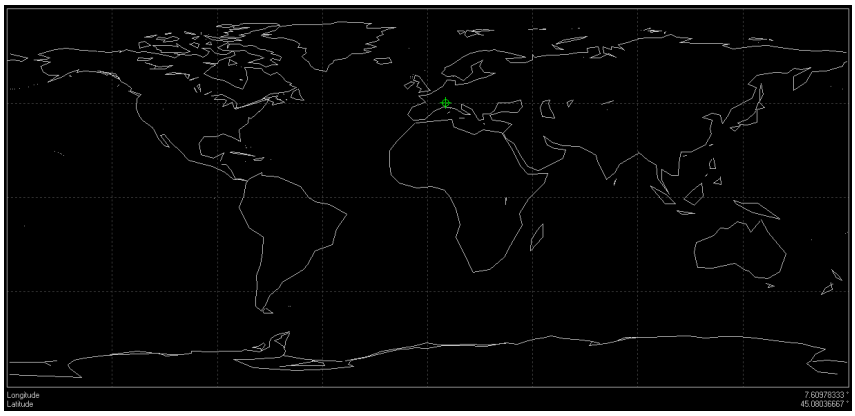

Figure 6.39: u-center map

Airspeed sensor

After having proved the operativity of the GNSS module, the same study has been carried out regarding the Airspeed module. This time, the sensor connecting interface has been connected to the Arduino board using the analog pins. Similarly to the previous case, a script has been written to read the transducer output and verify it operativity. The snippets shown in Figure 6.40 report the output captured from the sensor.

```
Raw Pressure: 1026 | PSI: 4.95
Raw Pressure: 1066 | PSI: 4.96
Raw Pressure: 1026 | PSI: 4.95
```

Figure 6.40: Airspeed sensor reading

As it can bee seen, this output provides a raw reading of the differential pressure perceived by the transducer to which the Pitot-tube has been attached. Nevertheless, the displayed values are totally arbitrary because no calibration had been applied to the sensor yet. Finally, to verify the responsivity of the device, the probe has been subjected to an arbitrary flow. This caused oscillation on the captured values.

Thanks to these tests, it has been possible to verify the operativity of these two peripherals, which constitute the main - non built-in - aircraft sensors. Radio communication devices testing and overall system validation will be discussed in the next section.

6.3.4 System-level testing

In order to verify the overall operativity of the on-board system, all the devices have been connected to the central FCC. After having correctly set up the firmware configuration, every sensor and device functioning has been tested. To this end, the iNav configuration and diagnosis environment has been employed. At first, the general status panel displayed as follows:

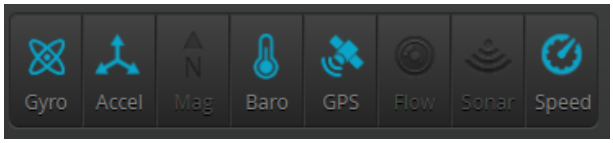

Figure 6.41: iNav general status

As it is possible to see, every element is displayed in blue: this shows that all the peripherals are working and communicating correctly with the FCC. Coming to consider more specific details, the following paragraphs describe the evaluation performed on each sub-system.

GNSS module

Along with the testing previously performed, this final verification has been useful to determine the effective synergic cooperation of the control software and the peripheral. The configuration tool offered the view displayed in Figure 6.42.

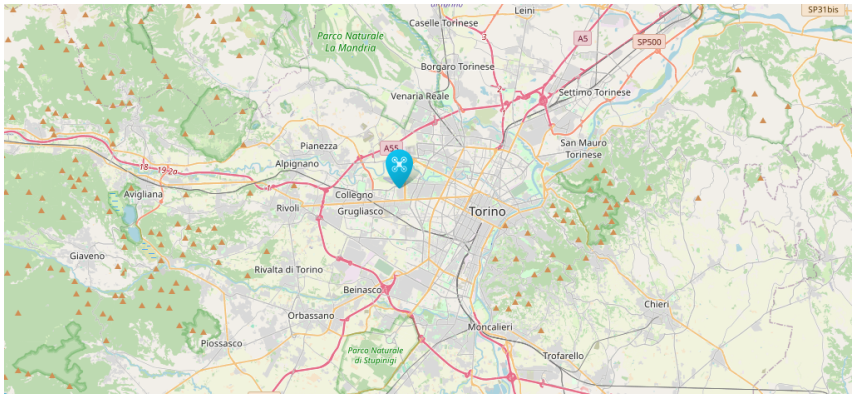

Figure 6.42: iNav GNSS

As it can be seen, the position is accurately determined: this shows that the GNSS module successfully interacts with FCC.

Airspeed module

Similarly to what done in the previous case, also the airspeed module outputs have been observed from the iNav firmware standpoint. In particular, a time history of the velocity reading has been used to verify the correct system operativity. Figure 6.43 shows a snapshot of the sensor reading.

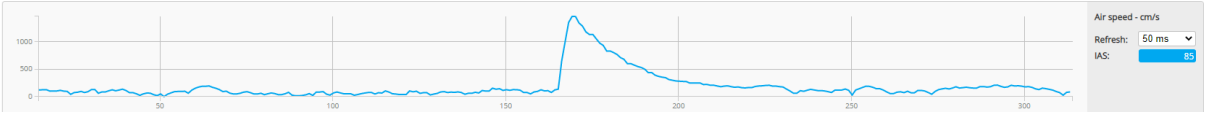

Figure 6.43: iNav Airspeed reading

As it can be seen, the airspeed is expressed in cm/s and the plot shows the measured value over time. The spike present at the middle of the plot represents a sudden jet the probe has been subjected to. This is useful to evaluate the response time of the sensor.

IMU

Coming to consider the set of built-in devices, the first element to be analyzed has been the IMU. This unit provides linear and angular acceleration measurements. Similarly to the previously described element, a plot of the time-history values of this couple of sensors is provided in Figure 6.44.

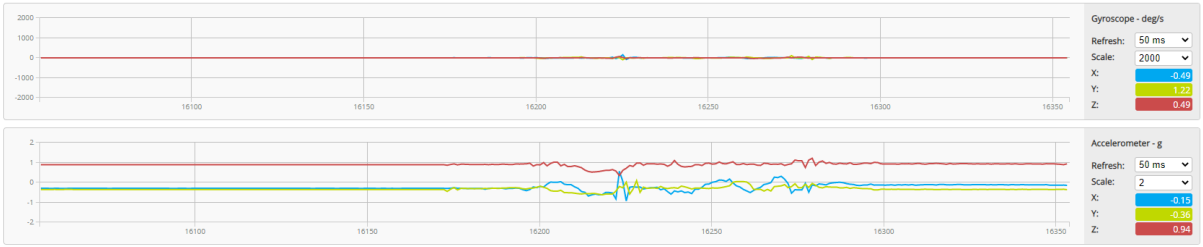

Figure 6.44: iNav IMU reading

As it can be noticed, when a solicitation is imposed to the FCC, incorporating the IMU, corresponding oscillations of the measured accelerations are shown. This proves this sensors velocity of response.

Barometer

This sensor provided static pressure reading mainly for the purpose of determine the aircraft altitude during flight. Figure 6.45 shows a snapshot of the time-history of the values read by the flight controller.

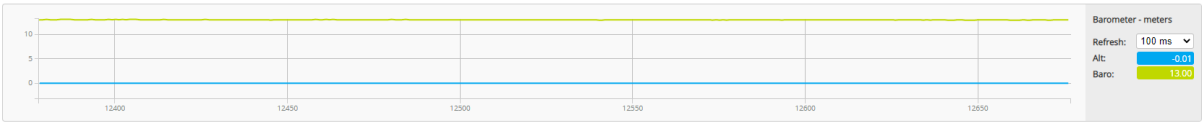

Figure 6.45: iNav barometer reading

As it can be seen, both a value for the actual pressure and its interpretation in terms of altitude are reported.

6.3.5 ExpressLRS module

The test described in this paragraph has been finalized to test the correct operativity of the ELRS control and telemetry. The iNav configuration interface offers the possibility to check the entity of the commands given through the control chain. Firstly, the up-link connection has been tested, as displayed in Figure 6.46.

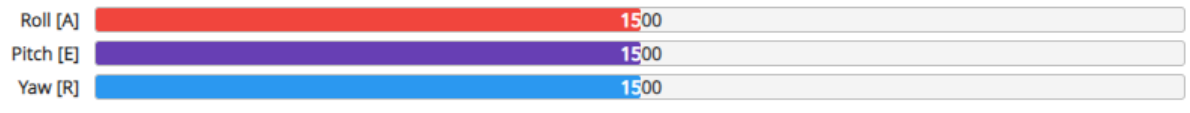

(a) Neutral condition

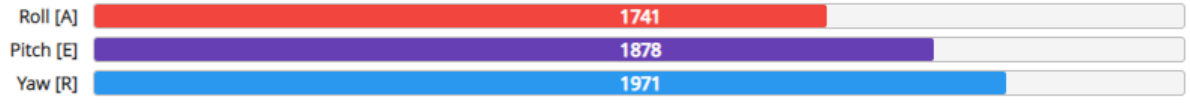

(b) Commands reading

Figure 6.46: iNav ExpressLRS module reading

The difference that can be seen among the reported colored bars indicate the magnitude of the arbitrary command that has been applied. This probes the correct functioning of the control data communication. Along with this, the downstream connection has been tested. To this end, the telemetry output visible on the ground controller display has been analyzed. The latter is shown in Figure 6.47.

Figure 6.47: Telemetry

This view shows information about aircraft, attitude, altitude, and speed. In addition to this, further data are reported regarding the radio link connection strength and the glider battery rating. In addition, also the telemetry data display responsiveness has been tested and it shows suitable features.

Video capturing

At last the video capturing functionality has been tested. In this matter, the camera and the VTX modules have been connected to the FCC and once having set the parameters to be displayed in the OSD view, the obtained result is shown in Figure 6.48.

Figure 6.48: Camera OSD

As it can be seen, the most important parameters are displayed. Furthermore, the reactivity of the telemetry transmission has been tested and it proved to be suitable for the intended use.

Chapter 7

Conclusions

This thesis work laid the basis for the development of a minimum viable product that aims to demonstrate how the Space exploration industry can interact with the world of everyday life through the ambitious project of the *SpArks* venture. The gliding aircraft, matter of which this discussion reports a preliminary design, has the objective of creating the first flying asset on which the edutainment platform can rely to create a totally new interactive game experience. Thanks to the resources and expertise provided by the world-famous Space industry *Thales Alenia Space*, it has been possible to undertake the interesting study that lies behind such an ambitious project as the development of a model aircraft. The activity required to define each key point of this project: from the on-board electronic devices to the basic aerodynamic features; from the regulatory guidelines for the use of stratospheric balloons to the study of the higher atmosphere environment and, finally, from the optimization of the flight mechanics properties to the validation of the final model structural resistance. Nevertheless, what gives the most important added value to this thesis project is the possibility of actually manufacture a real-life model of the designed vehicle and having the opportunity to integrate and test all the systems needed for this product to operate.

7.1 Main objectives achieved

The main goals that have been successfully achieved within the framework of this thesis project are presented hereafter.

Requirements analysis

The first part of this discussion has been dedicated to the exploration of the requirements imposed on this project. In this matter, a detailed collection of the restrictions and performance requirements this glider is subjected to is analyzed. In particular, the following aspects have been covered:

- regulatory requirements: this defines the regulatory framework that rules the operations with balloons;
- environmental requirements: in this regard the natural environments of the stratosphere and troposphere have been presented. This originates the set of requirements deriving from the domain of operability of this vehicle;
- mission requirements: this analysis eventually explores how the aircraft is supposed to interact with the project within which it has been developed. From this the set of performance requirements is established.

Avionics system architecture

The next area of development regarded the architecture of the on-board avionic system. In this matter, different solutions for the overall system architecture have been evaluated. Once identified the most suitable and effective one a detailed list of the needed devices has been produced. Downstream of this, a selection of a set of commercial elements has been proposed.

Aeromechanic study

The core part of this project has been concentrated on providing an aerodynamic configuration characterized by fundamental mechanical properties. In this regard, the following analysis have been accomplished:

- geometry analysis: the main geometric features have been determined in this matter. The wing shape and the adopted airfoil have been studied with the aim of obtaining the configuration that best suits the imposed requirement;
- C.G. analysis: this evaluation had the objective to determine the best avionics devices disposition, to the aim of ensuring a correct balancing of the aircraft;
- control surface analysis: once the previously reported steps have been completed, an optimization analysis has been performed to obtain a first-attempt sizing of the control surfaces.

Manufacturing and integration

After having conceived the final design of this glider, the following step consisted of detailed 3D modeling of every constituent element. This phase has been aimed to obtain a set of pieces that could be 3D printed in order to create a first real-life prototype. After having built the latter, all the electronics has been integrated and made operational. This resulted in a complete system and structure architecture capable of showcasing the main features this vehicle is supposed to have.

Validation and testing

Downstream of all the previous phases, a set of high-fidelity evaluations have been performed to validate the obtained results. To this end, some detailed CFD analysis have been run on an half-wing structure to evaluate the aerodynamic loading. Subsequently, using the pressure distribution data obtained, a structural analysis has been performed to confirm the model strength. Similarly, also the servo torque has been compared to the elevon hinge moment. The results of these final analysis are fundamental to define the future developments that may bring further improvement to this glider project.

7.2 Future developments

The project described in this thesis and summarized in the previous paragraphs laid the basis for the development of gliding vehicle capable of soaring from the upper layer of the atmosphere down to the ground. Although every main aspect has been covered by this discussion, further analysis, design and general improvements need to be done. The list presented hereinafter showcases the main development points where this project needs to be explored further:

- detailed CFD analysis: the first point about which it is necessary to deepen the study presented in this discussion is that of detailed fluid dynamics simulation. This type of evaluation is crucial to optimize the aerodynamic and, consequently, flight dynamics features of the aircraft. This also allows to obtain more precise knowledge about the aerodynamic loading acting on the aircraft structure, allowing to run more detailed structural analysis and improve the overall glider configuration;
- control surfaces optimization: as it has been already mentioned in the previous pages, the control surfaces of this model have been designed to satisfy specific steady-state equilibrium conditions without requiring excessive deflection. This led to a oversized elevon structure for the control over the lateral-directional plane. For this reason, it results necessary to carry out further study on the control surfaces in order to reduce the elevon authority along the lateral-directional plane, while still being able to equilibrate the glider in a sufficiently wide range of AoA over the longitudinal plane. In addition to this, a detailed study on the transient of elevons and rudder actuation has to be performed. This is crucial to understand the dynamic response of the glider in the face of an imposed command. This would be also useful to set which gain factors have to be set in the control logic of the aircraft to properly deflect the control surfaces;
- free controls stability study: downstream of the previous point, a study of the free controls condition has to be performed. This would provide an insight on the dynamics properties of the aircraft in the case of loss of authority of the control surfaces. This is representative of an on-board power failure.

In order to avoid losing control of the aircraft, it is advisable for the latter to be both statically and dynamically stable also in the free controls condition;

- servo actuators sizing: after having re-defined the glider control surfaces, it is necessary to correctly size the servo actuators. The main parameters that have to be taken into account for this operation are those of satisfying the maximum torque requirement and ensuring a sufficiently quick response and high accuracy. These constraints derive respectively from a precise evaluation of the elevons and rudder hinge moment and the stability studies about the control surfaces deflection angles;
- detailed structural FEM analysis: this details study can be performed after having obtained the results of the CFD analysis and having evaluated any load acting on the glider structure. Thanks to this analysis, it would be possible to further optimize the aircraft main components, improving the overall strength of the model while optimizing its weight. Furthermore, more specific study may also lead to the use of a different material;
- prototype assembly strategy validation and optimization: in this regard a detail study of the reliability of the joints between the various structural elements has to be carried out. This consists in a specific evaluation of the strength of the gluing and may lead to a re-engineering if the connecting interfaces and related adopted bonding strategies;
- experimental testing: once having manufactured a new-conception prototype, it is advisable to perform a wind tunnel testing session. This is fundamental to validate the previously mentioned design steps and to achieve a complete and quantitative understanding of the aircraft features and performance. This testing operation is also crucial to calibrate some of the on-board devices: the Pitot-tube and the control surfaces actuators;
- parachute design: this point is about the final phase of the nominal flight. Downstream of the mechanic, aerodynamic and inertial features of the model, a suitable parachute has to be conceived. This element must assure a safe falling velocity to preserve structural integrity upon landing. Along with this, a proper deployment procedure has to be set up;
- control logic refinement and integration: finally, a further point of development is about the integration of this flying platform with the final *SpArks* environment. Prior to this, though, it is advisable to develop a flight control logic specifically conceived for operation with this aircraft. This would ensure best performance and would be eventually suitable for integration with the edutainment platform.

These final paragraphs conclude the discussion about the design, manufacturing and testing of a *Micro Glider* for stratospheric flight. This activity involved an all-around application of the knowledge belonging to the Aerospace field, but also a study of topics relating to other engineering areas, such as electronics and radio communication. The final outcome of this work has been a prototype the *SpArks* venture can rely on to develop a part of its main activities. All of this has been possible thanks to the cooperation with and the support given by the world-famous Space company *Thales Alenia Space*.

Bibliography

[1] *About OpenVSP*. URL: https://openvsp.org/learn.shtml.

[2] *Aerodinamica delle Fusoliere*. URL: http://wpage.unina.it/agodemar/MS/Estratto%5C_Capitolo%5C_Aerodinamica%5C_Fusoliere.pdf.

[3] DIMEAS Angelo Lerro Politecnico di Torino. *Dispense del Corso: Meccanica del Volo*.

[4] Renzo Arina. *Fondamenti di Aerodinamica - Parte 1*. Levrotto & Bella, Torino, 2015.

[5] *CADDX ANT - 1200TVL 16:9 FPV NANO Camera*. URL: https://www.costruzionedroni.it/caddx-ant-1200tvl-169-fpv-nano-camera.

[6] *Cavo coassiale Linx RG58, RP-SMA / Tipo N, L. 96poll, col. Nero*. URL: https://it.rs-online.com/web/p/cavi-coassiali/2338561?gb=s.

[7] *Convertitore video Tipo composito, Audio RCA, S-Video x USB StarTech.com*. URL: https://it.rs-online.com/web/p/convertitori-video/2230923?gb=s.

[8] *Flight Controller F411-WTE*. URL: https://www.mateksys.com/?portfolio=f411-wte.

[9] *Kitronik micro Servo*. URL: https://it.rs-online.com/web/p/stem-componenti-di-movimento/2153180?gb=s.

[10] H. Kumar. "Making space accessible: Democratizing space exploration with adaptive and playable space assets". M.S. thesis, Politecnico di Torino. 2024.

[11] *Layers of the atmosphere*. URL: https://niwa.co.nz/atmosphere/layers-atmosphere.

[12] *Layers of the Atmosphere - Stratosphere*. URL: https://www.noaa.gov/jetstream/atmosphere/layers-of-atmosphere.

[13] *Layers of the atmosphere - The troposphere*. URL: https://niwa.co.nz/atmosphere/layers-atmosphere.

[14] *Matek ASPD-4525*. URL: https://www.costruzionedroni.it/matek-aspd-4525-digital-airspeed-sensor.

[15] *Matek ELRS R24-D*. URL: http://www.mateksys.com/?portfolio=elrs-r24.

[16] *MVP*. URL: https://www.dictionary.com/browse/mvp.

[17] National Oceanic as Atmospheric Administration. *Layers of the Atmosphere - Average temperature profile for the lower layers of the atmosphere*. URL: https://www.noaa.gov/jetstream/atmosphere/layers-of-atmosphere.

[18] *NMEA-0183 messages: Overview*. URL: https://receiverhelp.trimble.com/alloy-gnss/en-us/Welcome.html.

[19] *Oscar 18*. URL: https://it.farnell.com/siretta/oscar18-x-nf-s-s-22/antenna-mont-su-polo-muro-conn/dp/2666834.

[20] DIMEAS Piero Gili Politecnico di Torino. *Dispense del Corso: Fondamenti di Meccanica del Volo*.

[21] *Pocket Radio Controller (M2)*. URL: https://radiomasterrc.com/collections/pocket-radio/products/pocket-radio-controller-m2?variant=47236836327655.

[22] *RC832S High Sensitivity FPV Receiver*. URL: https://www.costruzionedroni.it/rc832s-58ghz-48ch-hig-sensitivity-fpv-receiver.

[23] *Seeed Studio 113020003*. URL: https://it.rs-online.com/web/p/moduli-gnss-e-gps/1793714?gb=s.

[24] RobertLanger ShadyFarah DanielG.Anderson. “PhysicalandmechanicalpropertiesofPLA,andtheirfunctionsin widespreadapplications — A comprehensivereview”. In: *AdvancedDrugDeliveryReviews* (2016).

[25] Stratoflights GmbH & Co. KG. *Weather Balloon - Datasheet*.

[26] *Tattu Batteria ricaricabile LiPo 11.1 V 750 mAh Numero di celle: 3 95 C Softcase*. URL: https://www.conrad.it/it/p/tattu-batteria-ricaricabile-lipo-11-1-v-750-mah-numero-di-celle-3-95-c-softcase-2316800.html.

[27] *Tattu Batteria ricaricabile LiPo 14.8 V 1300 mAh Numero di celle: 4 130 C Blocco XT60*. URL: https://www.conrad.it/it/p/tattu-batteria-ricaricabile-lipo-14-8-v-1300-mah-numero-di-celle-4-130-c-blocco-xt60-3304638.html.

[28] *TBS Unify Pro 5G8 V3 (RP-SMA)*. URL: https://www.team-blacksheep.com/products/prod:unify_pro?srsltid=AfmBOorw4RbOjCaIZQv6IpblqXsXFVGTMxFOnMxtf6uuMBHeuwnAj6-T.

[29] The European Commission. *COMMISSION REGULATION (EU) 2018/395 of 13 March 2018, Article 2*. 2018.

[30] The European Commission. *REGULATION (EC) No 216/2008 OF THE EUROPEAN PARLIAMENT AND OF THE COUNCIL, Annex IV 4.a*. 2018.

[31] The European Commission. *REGULATION (EC) No 216/2008 OF THE EUROPEAN PARLIAMENT AND OF THE COUNCIL, Annex IV 4.c*. 2018.

[32] The European Commission. *REGULATION (EC) No 216/2008 OF THE EUROPEAN PARLIAMENT AND OF THE COUNCIL, Annex IV 5.a*. 2018.

[33] The European Commission. *REGULATION (EC) No 216/2008 OF THE EUROPEAN PARLIAMENT AND OF THE COUNCIL, Article 8*. 2018.